UNDERSTANDING THE PROCESS-STRUCTURE-PROPERTY RELATIONSHIP IN BIODEGRADABLE POLYMER NANOCOMPOSITE FILMS

A Dissertation
Presented to
The Academic Faculty

by

Erin M. Sullivan

In Partial Fulfillment
of the Requirements for the Degree
Doctor of Philosophy in the
School of Materials Science and Engineering

Georgia Institute of Technology
December 2015

UNDERSTANDING THE PROCESS-STRUCTURE-PROPERTY RELATIONSHIP IN BIODEGRADABLE POLYMER NANOCOMPOSITE FILMS

Approved by:

Dr. Kyriaki Kalaitzidou, Advisor
G.W. Woodruff School of Mechanical Engineering
School of Materials Science & Engineering
Georgia Institute of Technology

Dr. Ben Wang, Co-advisor
H. Milton Stewart School of Industrial and Systems Engineering
School of Materials Science & Engineering
Georgia Institute of Technology

Dr. Rosario A. Gerhardt
School of Materials Science and Engineering
Georgia Institute of Technology

Dr. Robert J. Moon
U.S. Forest Service

Dr. Meisha L. Shofner
School of Materials Science and Engineering
Georgia Institute of Technology

Date Approved: November 4, 2015

This work is dedicated to my husband, W. Garrett Sullivan, sister, Lea Phillips,
and
to my parents, Alan and Leslye Phillips

ACKNOWLEDGEMENTS

First, I would like to thank my advisor, Dr. Kyriaki Kalaitzidou, for her guidance and mentorship. It was through her continued guidance that this study was possible. I would also like to thank my co-advisor, Dr. Ben Wang, for all of his support throughout my graduate studies. I would also like to thank my committee members, Dr. Rosario Gerhardt, Dr. Robert Moon, and Dr. Meisha Shofner, for their time, encouragement, and invaluable advice.

This study would not be possible without the necessary equipment. I would like to sincerely acknowledge Dr. Jonathan Colton and Dr. Rosario Gerhardt for their generosity in providing me access to their laboratories. I would especially like to thank Dr. Rosario Gerhardt for allowing me to use the impedance spectroscopy set-up she designed for the analysis of my samples. This study would not have been possible without this technique. My collaborators, Dr. Mohammad Naraghi and Parvin Karimineghlani, from Texas A&M University were very helpful and I offer them my gratitude for their ideas and assistance.

I would like to thank my colleagues in Dr. Kalaitzidou's laboratory, both past and present. I would especially like to thank Matthew Smith for his time, effort, and assistance in the laboratory. Throughout my graduate career I've had the opportunity to work with and mentor many undergraduate engineering students, Yun Ju Oh, Richard Flowers, Francesca Gencarella, Renée Puvvada, José Colon Quintana, and Vanessa Prema. It was an honor to interface with you and I thank you for your assistance.

My graduate studies and research would not have been possible without the financial support provided by the Cytec Engineered Materials Doctoral Fellowship, the Georgia Tech Manufacturing Institute, the Jewell Family Fellowship, and the P^3Nano Forestry Endowment. I thank them for their confidence in my research.

My friends and family have been immeasurably supportive throughout my education. Thank you to my husband, W. Garrett Sullivan, for always being there. It's not only been great having your engineering expertise and mathematical knowledge, but your love and support is and has been so important to me. Thank you to my parents, Leslye and Alan Phillips, my sister, Lea Phillips, and brother-in-law, Dr. Michael Manley. Each of you has provided me with invaluable love and support over the years, each in your own way. Thank you to my friend, Dr. Shalini Saxena, for all of the thoughtful discussions over coffee or lunch. I could always count on you for advice on anything from life skills to polymer engineering. Finally, I would like to thank my dogs, Suki and Frodo, for always welcoming me home with hugs and kisses even after a tough day.

TABLE OF CONTENTS

LIST OF TABLES

Page

LIST OF FIGURES

Page

LIST OF SYMBOLS

B	full width at half maximum
c	filler volume fraction
df	degree of freedom
E	elastic modulus
E^*	effective elastic modulus
E''	loss modulus
E'	storage modulus
E_0	elastic modulus of the matrix
E_1	elastic modulus of the filler
E_{11}	longitudinal elastic modulus
E_{22}	transverse elastic modulus
f	frequency
F^*	tabulated F-statistics value
F_o	F-statistic
i	current
i_m	current magnitude
K	dimensionless shape factor
k	number of factors
L	apparent crystalline lamella thickness
ℓ	low level treatment combination
M_n	number average molecular weight
n	number of observations per factor level
R^2	coefficient of determination

S_{ijkl}	Eshelby's tensor
T	temperature
t	thickness
t^*	apparent thickness
T_{cc}	cold crystallization temperature
T_g	glass transition temperature
V	voltage
V_m	voltage magnitude
x	coded variables
Z^*	complex impedance
$\|Z^*\|$	impedance magnitude
β	regression coefficient(s)
β_0	overall mean
ΔH°_m	theoretical melting enthalpy of 100% crystalline polymer
ΔH_c	cold crystallization enthalpy
ΔH_m	melting enthalpy
θ	Bragg angle
ϑ	phase angle
λ_o	Lamé constant of the matrix
λ_1	Lamé constant of the filler
μ_o	Lamé constant of the matrix
μ_1	Lamé constant of the filler
ν_0	Poisson's ratio of matrix
χ	degree of crystallinity
ω	angular frequency

LIST OF ABBREVIATIONS

ANOVA	Analysis of Variance
BPA	bisphenol-A
CN	cellulose nanomaterials
CNC	cellulose nanocrystals
CNT	carbon nanotubes
DEHP	di-(2-ethylhexly)phthalate
DMF	dimethylformamide
DSC	differential scanning calorimetry
E-CM	electrospinning / compression molding
FC	fast cooling
GNP	exfoliated graphite nanoplatelets
HT	Halpin-Tsai
IS	impedance spectroscopy
LNR	liquid natural rubber
MA	maleic anhydride
MC-CM	melt compounding /compression molding
MS	mean square
MWNT	multi-walled carbon nanotubes
PEG	polyethylene glycol
PET	polyethylene terephalate
PHA	polyhydroxyalkanoate
PHB	polyhydroxybutyrate
PLA	polylactic acid

PMMA	polymethyl methacrylate
POM	polarized optical microscopy
PP	polypropylene
PS	polystyrene
PVOH	polyvinyl alcohol
SC	slow cooling
s-CNC	silylated cellulose nanocrystals
SEM	scanning electron microscopy
SoC	solution casting
SoC-CM	solution cast / compression molded
SS	sum of squares
SWNT	single-walled carbon nanotubes
TEM	transmission electron microscopy
TGA	thermogravimetric analysis
TW	Tandon-Weng
WAXD	wide-angle X-ray diffraction
XPS	X-ray photoelectron spectroscopy

SUMMARY

The focus of this study was to explore process-structure-property relationships in biodegradable polymer nanocomposite films in order to eliminate the commonly used trial and error approach to materials design and to enable manufacturing of composites with tailored properties for targeted applications. The nanofiller type and concentration, manufacturing method and compounding technique, as well as processing conditions were systematically altered in order to study the process-structure-property relationships. Polylactic acid (PLA) was used as the polymer and exfoliated graphite nanoplatelets (GNP), carbon nanotubes (CNT), and cellulose nanocrystals (CNC) were used as reinforcement. The nanocomposite films were fabricated using three different methods: 1) melt compounding and melt fiber spinning followed by compression molding, 2) solution mixing and solvent casting, and 3) solution mixing and electrospinning followed by compression molding. Furthermore, the physical properties of the polymer, namely the crystallization characteristics were altered by using two different cooling rates during compression molding. The electrical response of the composite films was examined using impedance spectroscopy and it was shown that by altering the physical properties of the insulating polymer matrix, increasing degree of crystallinity, the percolation threshold of the GNP/PLA films is significantly reduced. Additionally, design of experiments was used to examine the influence of nanofiller type (CNT versus GNP), nanofiller content, and processing conditions (cooling rate during compression molding) on the elastic modulus of the composite films and it was concluded that the cooling rate is the primary factor influencing the elastic modulus of both melt compounded CNT/PLA and

GNP/PLA films. Furthermore, the effect of nanofiller geometry and compounding method was examined and it was shown that the high nanofiller aspect ratio in the CNT/PLA films led to decreased percolation threshold compared to the GNP/PLA films. The melt compounded GNP/PLA films displayed a lower percolation threshold than the solution cast GNP/PLA films most likely due to the more homogeneous distribution and dispersion of GNP in the solution cast films. Fully biodegradable and biorenewable nanocomposite films were fabricated and examined through the incorporation of CNC in PLA. Through the addition of CNC, the degree of crystallinity of the matrix was significantly increased. Focusing the design space through investigation of process-structure-property relationships in PLA nanocomposites, can help facilitate nanocomposites with tailored properties for targeted applications.

CHAPTER 1

INTRODUCTION

1.1 Biodegradable Composites

The plastics industry is the third largest manufacturing industry in the United States [1]. Plastic consumption has reached more than 300 million tons annually world-wide, with approximately 50% of this being used for disposable applications, where products are discarded within one year of purchase [2, 3]. Plastic disposal has been a widespread problem in recent years. Plastic waste causes ~$13 billion in damage to marine ecosystems annually due to littering and poor management and overflow of landfills [4]. Furthermore, the negative effect of plastics is not localized to marine ecosystems, recent studies have shown that the prolonged exposure to plastics, specifically bisphenol-A (BPA) and di-(2-ethylhexyl)phthalate (DEHP), has a negative effect on reproductive health [2]. Plastic waste is disposed of using four primary methods: landfills, incineration, recycling, and biodegradation [2, 5]. The use of landfills or even utilization methods such as incineration and recycling still pose threats to the global environment for today and for future generations. There is limited acceptable landfill space due to the rapid population growth and concern for future generations if landfills continue to be a primary source for plastic waste disposal. Incineration produces large amounts of carbon dioxide and sometimes toxic gases, which can cause global warming and global pollution, respectively [2, 5]. Recycling is sometimes seen as a solution to this problem of environmentally conscious plastic waste disposal; however it

comes with its own set of problems. The quality of recycled plastic is lower and the cost is higher for consumers due to increased expenditures of labor and energy during the recycling process, i.e. removal of waste, sorting, washing, drying, grinding etc. [2, 5]. There is an urgent need for the production and implementation of biodegradable and biorenewable plastics that can be made without any toxic components and can be naturally degraded. This has been the primary driver for researchers and engineers to further develop and tailor the properties of biodegradable polymers for widespread use [5].

Biodegradable polymers are defined as polymers that mineralize due to microbially triggered chain scissions. There are a wide range of biodegradable polymers that can be derived through numerous methods. Generally, there are four categories of biopolymers [5, 6]: 1) biopolymer that are derived directly from the natural sources, such as cellulose and starch; 2) biopolymers synthesized from small molecules through the use of microorganisms like bacteria, such as polyhydroxybutyrate (PHB) or polyhydroxyalkanoate (PHA); 3) biopolymers created through polymerization of bio-derived monomers, such as polylactic acid (PLA); and 4) biopolymers created through petroleum based sources, such as aliphatic and aromatic polyesters. In recent years, PLA has attracted attention due to its environmentally friendly and scalable production [5].

1.2 Polylactic Acid, PLA

Polylactic acid (PLA) is a thermoplastic aliphatic polyester derived from sugarcane or cornstarch and is 100% biodegradable and biorenewable and has the chemical formula $C_3H_4O_2$ and the chemical structure, seen in Figure 1.1. PLA is

produced through bacteria fermentation of D-glucose in corn, a renewable feedstock. The interest in production of PLA was pioneered by Carothers in 1932. However, Carothers' initial aliphatic polyester produced from lactic acid had a low molecular weight and poor mechanical performance [7]. Over the years, further advances were made in manufacturing an aliphatic polyester from lactic acid. However, cost was the primary restriction outside of medical grade applications until the late 1980s when advances in bacteria fermentation decreased the cost of the previously used petrochemical-derived production, making further breakthroughs possible [7].

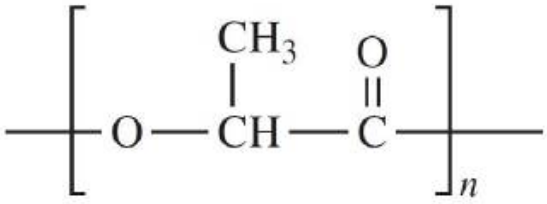

Figure 1.1 PLA monomer

The production of PLA begins with the extraction of starch from a bulk source, such as corn, sugarcane, sugar beets or rice. The starch is then converted to dextrose via a process called enzymatic hydrolysis. Dextrose is then fermented to lactic acid via acidulation and a series of purification steps [8]. PLA can be polymerized from lactic acid either via direct condensation or ring opening polymerization [8, 9]. In a direct condensation reaction, water is removed via condensation with the aid of a solvent in a high temperature and high vacuum environment [8]. However, the use of direct condensation is limited because it is difficult to achieve high molecular weight PLA due

to challenges removing trace amounts of water during polymerization [9]. Furthermore, the use of a solvent during synthesis has a negative environmental impact, as opposed to producing PLA in melt without the use of solvents [9]. The ring opening polymerization reaction begins with the removal of water from aqueous lactic acid via a condensation reaction without the use of solvent. This process produces a low molecular weight prepolymer. The prepolymer is converted to lactide by depolymerization through the use of a catalyst and the lactide is purified though vacuum distillation [8, 9]. High molecular weight PLA is produced via a solvent-free ring opening polymerization reaction. This process is outlined in Figure 1.2.

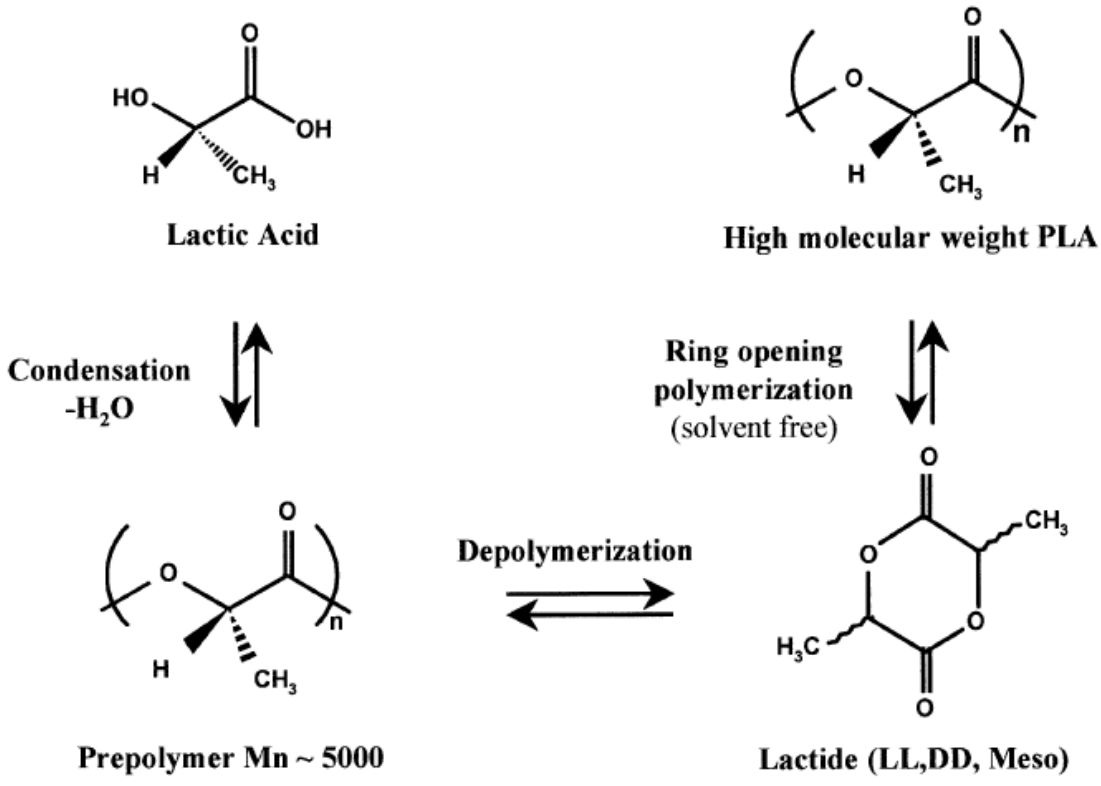

Figure 1.2 Production of PLA via ring opening polymerization [8]

Because lactic acid is a chiral molecule, there are two stereoisomers that exist: L-isomer and D-isomer. These isomers can co-exist in a racemic mixture. For example, a chemically synthesized lactic acid mixture is typically 50% L-isomer and 50% D-isomer; however for fermentation derived lactic acid, a typical ratio is approximately 99.5% L-isomer and approximately 0.5% D-isomer [8, 9]. Three potential types of lactide dimer exist: 1) D,D-lactide, which is also called D-lactide; 2) L,L-lactide, which is also called L-lactide; and 3) L,D-lactide or D,L-lactide, which is also called meso lactide [8]. These lactide types are outlined in Figure 1.3.

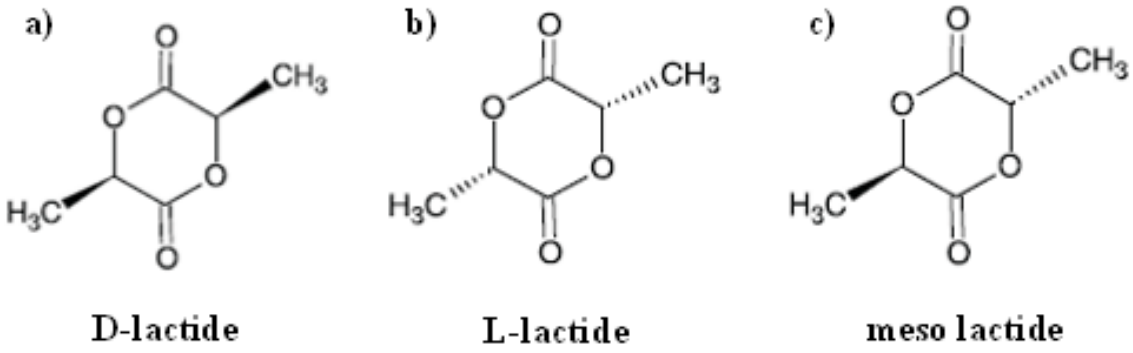

Figure 1.3 Types of lactide: a) D-lactide, b) L-lactide, and c) meso lactide [6]

Typically, PLA is degraded through a hydrolytic degradation process, usually occurring in two steps. First, the higher molecular weight polyester chains hydrolyze to low molecular weight oligomers. The second stage of degradation is facilitated by microorganisms that convert the oligomers into byproducts such as carbon dioxide and

water [9]. The degradation process is affected by a number of factors including moisture, temperature, crystallinity, and the pH of the environment [9, 10].

While a there is a concern for the durability of PLA due to its hydrolysis in water and sometimes in highly humid conditions, PLA has properties comparable to petroleum based thermoplastics such as polystyrene (PS), polyethylene terephalate (PET), and polypropylene (PP) [7]. A property comparison summary is seen in Table 1.1. Properties such as the density and modulus of elasticity are very comparable with that of PET, while the elongation at break and flexural strength is closer to that of PS. PLA properties can be optimized and enhanced through the incorporation of various nanofillers. The use of nanofillers or nanoreinforcements is outlined in the next section.

Table 1.1 Property comparison of PLA, PET, PP, and PS [11-14]

Property	PLA	PET	PP	PS
Density [g/cm^3]	1.2-1.3	~1.4	~0.94	~1.1
Melt temperature [°C]	145-155	~246	~160	~222
Glass transition [°C]	55-65	~74	~0	~91
Ultimate tensile strength [MPa]	~49	~70	16-30	~40
Tensile strength, yield [MPa]	~45	~62	~32	~33
Elongation at break [%]	~21	~68	~154	~14
Modulus of elasticity [GPa]	~3.63	~3.45	~1.75	~2.76
Flexural Modulus [GPa]	~3.84	~4.92	~1.44	~2.61
Flexural Strength [MPa]	75-85	~120	~45	~72
Izod impact, notched [J/cm]	~1.6	0.40-0.65	0.48-0.77	0.50-0.53
Electrical resistivity [Ω.cm]	~10^{16}	~3.6 x 10^{16}	~1.2 x 10^{17}	~3.2 x 10^{16}

1.3 Nanoreinforcements

A nanofiller or nanoreinforcement is defined as a filler or additive with one dimension on the scale of 100 nm or less. Nanofillers can have a dramatic impact on the properties of the composite even at low concentrations. Due to their size, nanofillers have an extremely high surface area to volume ratio allowing for increased performance of the composite through increased matrix/filler interface with a minimal addition of filler. Nanofillers can reinforce significantly more efficiently compared to conventional fillers due to this high surface area to volume ratio. Nanofillers are divided into three main categories depending on their shape: nanoplatelets (one-dimensional geometry, seen in Figure 1.4a), nanofibers (two-dimensional geometry, seen in Figure 1.4b), and nanoparticles (three-dimensional geometry, seen in Figure 1.4c).

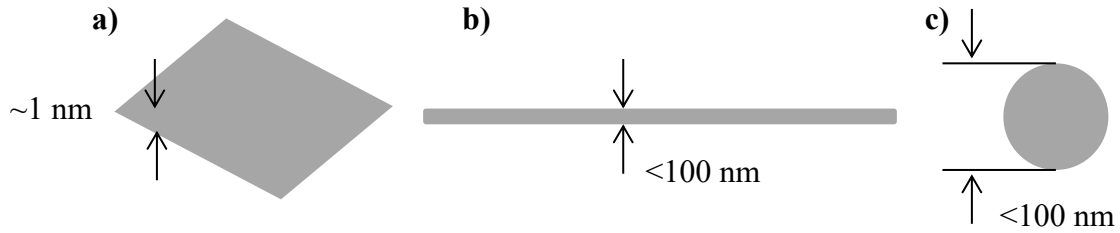

Figure 1.4 Schematic of the three primary geometries of nanofillers used in polymer nanocomposites: a) nanoplatelets, b) nanofibers, and c) nanoparticles

A variety of nanofillers have been used to reinforce polymers including: ceramic nanofillers such as indium tin oxide [15] or silica nanoparticles [16], inorganic nanofillers such as nanoclays [17], organic nanofillers such as carbon nanotubes (CNT) [18] and exfoliated graphite nanoplatelets (GNP) [19] or even bio-based nanofillers derived from cellulosic materials [20]. There is a large focus on carbon based nanofillers due to their superior mechanical and electrical properties at a fraction of the weight of micro-size fillers. For example, CNT and GNP have an elastic modulus greater than 1 TPa and tensile strength 10-100 times greater than the strongest steel [18, 21]. In addition to superior mechanical properties, carbon based nanofillers have desirable electrical and thermal properties. The electrical conductivity of CNT has been reported to be in the range of $10^4 - 10^7$ S/m [22] and similarly, the electrical conductivity of GNP has been reported to be greater than 10^4 S/m [21]. Furthermore, the thermal conductivity of CNT is extremely high and reported to be in the range of 2000 to 6000 W/m K [23] compared to typical insulating thermoplastics which usually display thermal conductivities in the range of 0.2 to 0.5 W/m K [23]. Both CNT and GNP based polymer composites have a wide range of potential applications including: electronics packaging, electromagnetic shielding, and sporting goods, to name a few.

Furthermore, in recent years there has been a lot of work done to produce fully biodegradable composites using bio-based polymer, like PLA, and bio-based fillers, such as cellulose nanomaterials (CN) [20]. CNs are cellulose based nanoparticles isolated from bulk cellulose sources, such as wood or plants, and due to their unique combination of high mechanical and barrier properties, low density, low toxicity, and potential to be sustainably produced at industrial scale quantities at a reasonable price [24], CNs have

attracted attention as a polymer reinforcement in composite development for potential applications such as packaging, biomedical implants, and textiles [20, 25, 26]. Cellulose nanocrystals (CNC) are one type of CN and are rod-like particles (3-20 nm in width and 50-500 nm in length) of highly crystalline cellulose (65-90%).

While the inherent properties of the nanofiller used are important, the dispersion and distribution of the nanofiller are also critical components to how the nanofiller contributes to the bulk properties of the polymer composite. Due to the high surface area of nanofillers, the composite properties are highly dependent on the dispersion and distribution of nanofiller throughout the matrix. Maximizing filler dispersion and distribution to create homogeneous composites is a challenge with many nanofillers, due to their increased likelihood to aggregate compared to microscale fillers because of this high surface area. Dispersion and distribution are terms that are often used interchangeably; however, they are not the same. The dispersion refers to how the individual filler particles are arranged in relation to other filler particles, while distribution refers to how the filler as a whole is arranged in relation to the bulk composite. Figure 1.5 shows a schematic of the difference between dispersion and distribution. Controlling nanofiller distribution and dispersion is critical when engineering properties of polymer nanocomposites. There are three primary processing techniques used to help facilitate nanofiller distribution and dispersion [27]: 1) melt compounding, 2) solution compounding, and 3) in-situ polymerization.

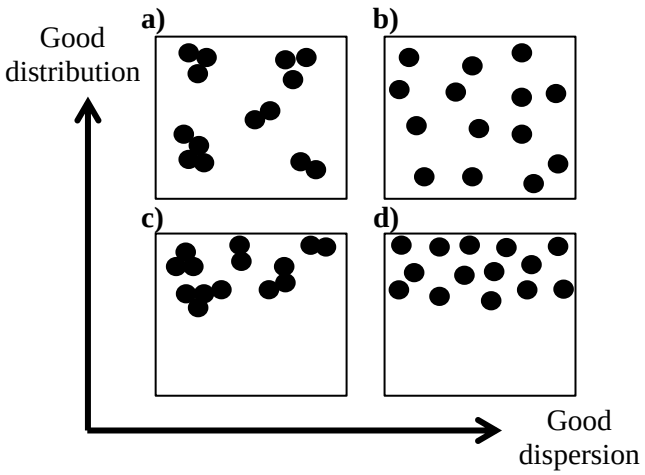

Figure 1.5 Schematic of a composite with a) good filler distribution and poor filler dispersion, b) good filler distribution and good filler dispersion, c) poor filler distribution and poor filler dispersion, and d) poor filler distribution and good filler dispersion

In melt compounding, a nanofiller is incorporated into a viscous polymer melt via shear mixing. Composites can then be produced via compression molding, extrusion, or injection molding. Melt processing is a scalable form of manufacturing that requires no harsh chemicals; however, the viscosity of many polymers is too high to homogeneously disperse the nanofiller in the matrix. The use of a twin screw is typically preferred over a single screw extruder for many composites due to its better dispersive mixing [28]. Furthermore, melt processing is often limited to thermoplastics with relatively low melting temperatures for ease of processing.

Solution compounding involves dissolving the polymer in a solvent, adding the nanofiller into the polymer solution, and removing the solvent via controlled evaporation to obtain a composite powder. Alternatively, the nanofiller can be dispersed in a solvent via agitation, such as magnetic stirring or sonication, and then this suspension can be

added to the polymer solution. Solution compounding can be beneficial for filler dispersion because the polymer viscosity is reduced in solution; however, in many cases, solution compounding requires the use of toxic, harmful solvents that can be dangerous for humans, as well as detrimental to the environment. Furthermore, the aspect ratio of a nanofiller may be reduced with prolonged agitation and therefore, the composite properties can be reduced [29]. PLA has a high solubility in solvents such as chloroform, benzene, and methyl chloride [30]. Crystallization rate and kinetics can be altered by the solvent used. For example, using a solvent which enables high polymer-solvent interactions, such as chloroform, will lead to highly crystalline PLA [30].

During in-situ polymerization, the nanofiller is first dispersed in a monomer and then the monomer is polymerized. In-situ polymerization is a desirable technique for polymer composite fabrication particularly when the polymer matrix is insoluble or has a very high melting temperature, therefore the composite cannot be produced via solution or melt processing [27]. Furthermore, high nanofiller loading can be achieved and chemical functionalization of the nanofiller can facilitate better interfacial adhesion between the nanofiller and matrix during polymerization [27]. However, in-situ polymerization cannot be achieved with all thermoplastic polymers and is mainly used with thermoset resins.

The nanofiller dispersion and distribution can also be altered through functionalization of the nanofiller. Nanofillers like, GNP and CNT, can be particularly difficult to disperse in a polymer matrix like PLA due to their inherent interfacial chemistry. Many techniques have been previously studied to enhance polymer-nanofiller

interfacial interactions and augment PLA physical properties. These techniques include the use of nanofiller functionalization, coupling agents, and compatibilizers.

Nanofillers are often functionalized in order to maximize interfacial compatibility with the polymer matrix. For example, GNP and CNT that are not functionalized can often lead to poor interfacial properties in PLA composites due to their hydrophobicity, which is in direct contrast with PLA's affinity for water [31]. Functionalization of CNT through the addition of carboxylic acid is commonly used to enhance polymer/matrix interactions. Carboxylic acid can be added to the nanotube structure via direct attachment of the functional group or it can be introduced through inducing targeted defects [32]. While functionalization of the nanofiller can improve interfacial properties, it can also alter properties of the nanofiller and thus of the composite, such as electrical conductivity. As reported, untreated single-walled carbon nanotubes (SWNT) are good electrical conductors, while fluorinated SWNT display insulating behavior [33].

Because PLA is non-polar, interfacial interactions between PLA and many nanofillers with polar functional groups are limited. Therefore, maleic anhydride (MA) is commonly used as a coupling agent to facilitate PLA/nanofiller interactions [34, 35]. Another coupling agent that is commonly used in bio-based polymer nanocomposites, particularly in CN/PLA composites, is silane. Due to the chemistry of silane it can bond to both polar nanofillers and to non-polar polymers, like PLA [36]. Furthermore, commonly used compatibilizers in PLA composites to help facilitate interfacial adhesion include liquid natural rubber (LNR) [37] and other thermoplastics, like PP or polymethyl methacrylate (PMMA), grafted with MA or other components [38, 39]. Due to its high ductility and biodegradability, LNR is used to increase PLA's elongation at break [37].

Compatibilizers may enhance the interfacial interactions between the nanofiller and the polymer matrix, but they can also alter overall performance of the polymer nanocomposite and must be chosen carefully.

1.4 Research Motivation, Goals, and Objectives

This research aims to 1) fabricate and characterize PLA nanocomposite films and 2) eliminate the trial and error style approach to materials design through the creation of a property roadmap that can lead to nanocomposites with tailored properties for targeted applications. This will be accomplished by systematically altering nanofiller type and concentration, fabrication technique and compounding method, as well as processing conditions.

To achieve the research goal, the following objectives have been identified:

1) Investigate the effect of nanofiller concentration and nanofiller type on the composite film properties.
2) Investigate the effect of compounding method, which alters the distribution and dispersion of the nanofiller, on the composite film properties.
3) Explore the effect of the physical properties of the polymer, which can be altered by tuning the processing conditions, on the composite film properties.

Figure 1.6 displays an overview of the research that will be presented.

Figure 1.6 Overview of presented research on PLA nanocomposite films

CHAPTER 2

MATERIALS, PROCESSING, AND CHARACTERIZATION

2.1 Materials

2.1.1 Matrix

Polylactic acid (PLA, M_n = 1.42 x 10^4 g/mol, semi-crystalline) in pellet form was purchased from Nature Works LLC, Minnetonka, Minnesota, U.S.A. (product name of PLA 3051D) was used as the matrix material. A detailed summary of PLA physical and mechanical properties are listed below in Table 2.1:

Table 2.1 Physical and mechanical properties of Nature Works PLA 3051D pellets as reported by Nature Works [12]

Physical Properties	
Specific Gravity	1.24
Melt Index (g/10 min at 190°C)	10-30
Relative Viscosity	3.0-3.5
Crystalline Melt Temperature (°C)	145-155
Glass Transition Temperature (°C)	55-65
Clarity	Transparent
Mechanical Properties	
Tensile Yield Strength (MPa)	48
Tensile Elongation (%)	2.5
Notched Izod Impact (J/m)	0.16
Flexural Strength (MPa)	83
Flexural Modulus (MPa)	3828

2.1.2 Nanoreinforcements

Exfoliated graphite nanoplatelets (GNP) were purchased from XG Sciences Inc., East Lansing, Michigan, U.S.A. (product name xGnP® Grade C). GNP particles consist of several graphene sheets arranged to have a platelet-like morphology, as seen in Figure 2.1. The GNP supplied in dry powder form with no additional surface treatment has a specific surface area of ~750 m^2/g, an average diameter between 1-2 μm, and a thickness on the order of 10 nm. A detailed summary of the typical properties of GNP particles are presented below in Table 2.2:

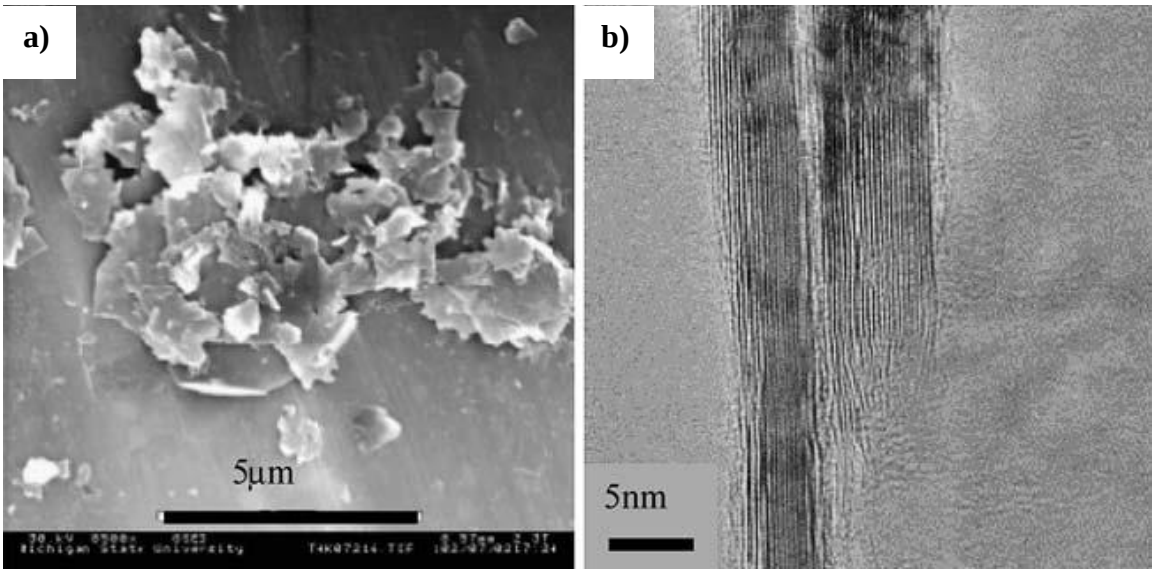

Figure 2.1 a) Topographical SEM of GNP and b) TEM image of GNP cross section [40]

Table 2.2: Typical properties of GNP as reported by XG Sciences Inc. [41]

Property	Parallel to Surface
Density (g/cc)	2.2
Carbon Content (%)	>99.5
Thermal Conductivity (W/m K)	3,000 (in-plane) 6 (normal)
Thermal Expansion (CTE)	4-6 x 10^{-6} (in-plane) 0.5-1.0 x 10^{-6} (normal)
Tensile Modulus (GPa)	1,000
Tensile Strength (GPa)	5
Electrical Conductivity (S/m)	10^{7} (in-plane) 10^{2} (normal)

Multi-walled carbon nanotubes (MWNT) of greater than 95 wt% purity with a 30-50 nm outer diameter were purchased from CheapTubes, Cambridgeport, Vermont, U.S.A. A detailed summary of the MWNT properties are listed below in Table 2.3. MWNT are essentially concentric single-walled nanotubes, as seen in Figure 2.2.

Table 2.3: Properties of MWNT as reported by CheapTubes [42]

Multi-walled Carbon Nanotube Properties	
Outer Diameter (nm)	30-50
Length (μm)	10-20
Purity (wt%)	>95
Ash (wt%)	<1.5
Specific Surface Area (m^2/g)	>60
Electrical Conductivity (S/cm)	$>10^{2}$

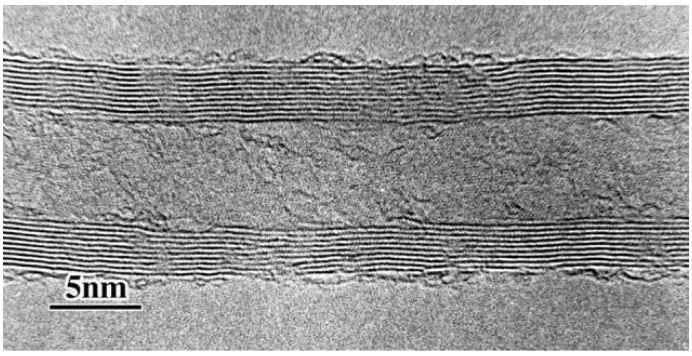

Figure 2.2 TEM image of MWNT [18]

An unmodified aqueous suspension of cellulose nanocrystals (CNC) was purchased from the University of Maine Process Development Center and manufactured at U.S. Forest Service's Cellulose Nanomaterials Pilot Plant at the Forest Products Laboratory, Madison, Wisconsin, U.S.A. The suspension was 11.9 wt% CNC/water and the CNC used were derived from dissolving pulp via sulfuric acid hydrolysis. The average length and width of the CNC were 6.4 ± 0.6 nm and 138 ± 22 nm, respectively [43]. Figure 2.3 shows a representative TEM image of CNC derived from wood pulp.

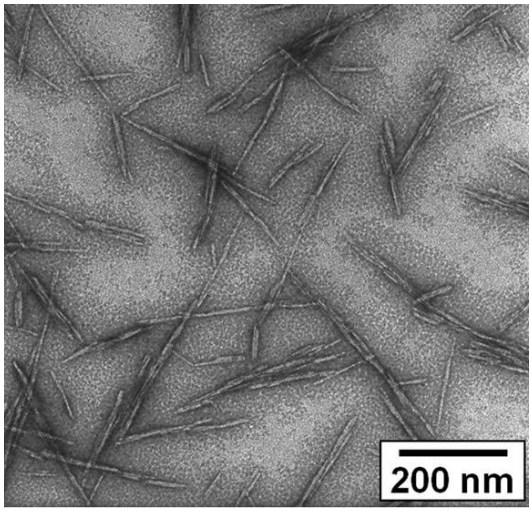

Figure 2.3 TEM image of CNC derived from wood pulp [20]

2.2 Manufacturing Methods

2.2.1 Melt Compounding / Compression Molding, MC-CM

First, the nanofiller (GNP, CNT, or CNC) was incorporated into the PLA polymer matrix via melt blending using a DSM 15cc Compounder (a vertical, co-rotating twin-screw microextruder) at a screw speed of 150 RPM and an operating temperature of 190°C (GNP and CNT composites) or 175°C (CNC composites) for approximately 3 minutes. (Note that the CNC was incorporated via direct liquid feeding of the as-received CNC/water suspension.) The nanofiller/PLA mixture was then extruded out of a 0.8 mm orifice at a 15 RPM pull-out rate and melt spun into fibers of ~60-70 μm diameter (draw ratio of ~12). A schematic of the compounding process is shown in Figure 2.4. By melt spinning fibers prior to compression molding, the nanofiller agglomeration size can be better controlled and minimized and partial control of the nanofiller orientation/distribution was achieved. The composite fibers with nanofiller content ranging from 0-15 wt% were then compression molded into films with a thickness of either ~160 μm or ~110 μm using a manual four-column 12 ton Carver hydraulic press (model 4122) with controlled cooling. As seen in Figure 2.4, the composite fibers were chopped and randomly oriented before placement in the mold, promoting anisotropy in the plane of the film. The fibers were softened on the heated platens for 5 minutes at 180°C (GNP and CNT composites) or 3 minutes at 175°C (CNC composites) before a load of ~1 MPa was applied for 5 minutes (GNP and CNT composites) or 3 minutes (CNC composites). To minimize plastic deformation and thermal residual stresses, the samples were allowed to cool below the glass transition temperature (~50°C) before being removed from the mold. To investigate the effect of cooling rate during

compression molding, films were cooled at a non-linear rate following Newton's law of cooling shown in Figure 2.5 of either an approximate average of 16 °C/min (fast cooling referred to as FC and achieved using cooling water, seen in Figure 2.5a) or 0.4°C/min (slow cooling referred to as SC and achieved using ambient temperature air cooling, seen in Figure 2.5b).

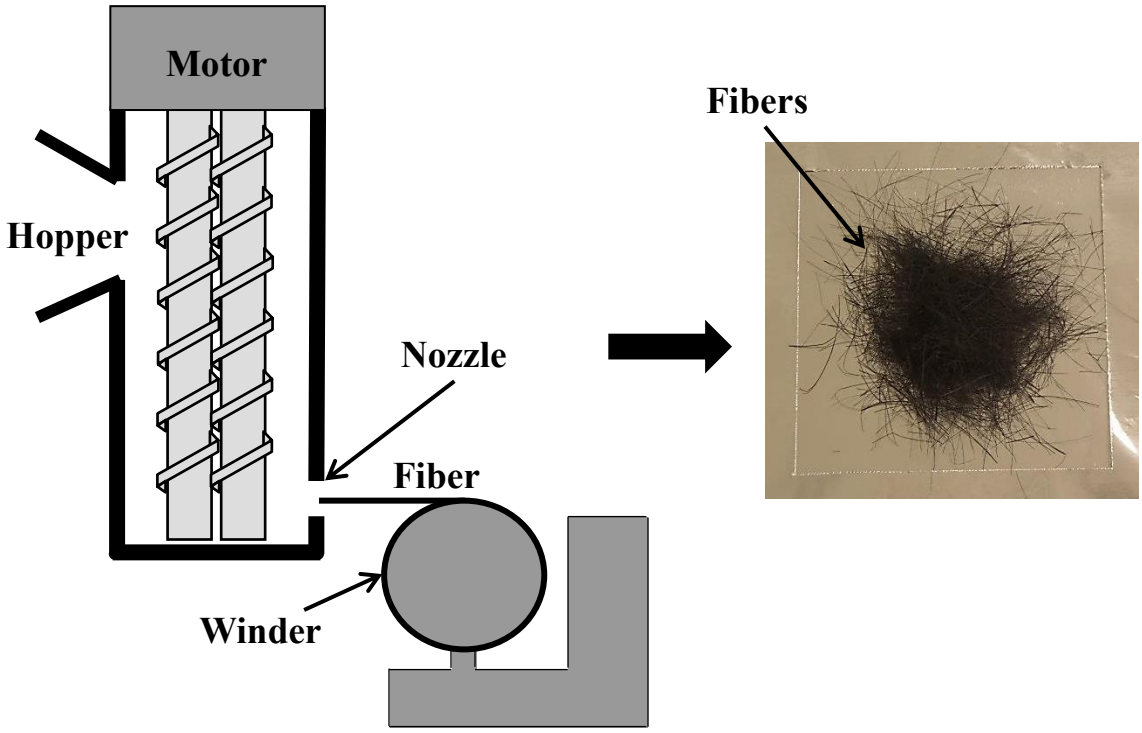

Figure 2.4 Schematic of melt fiber spinning process and representative image of random fiber orientation prior to compression molding

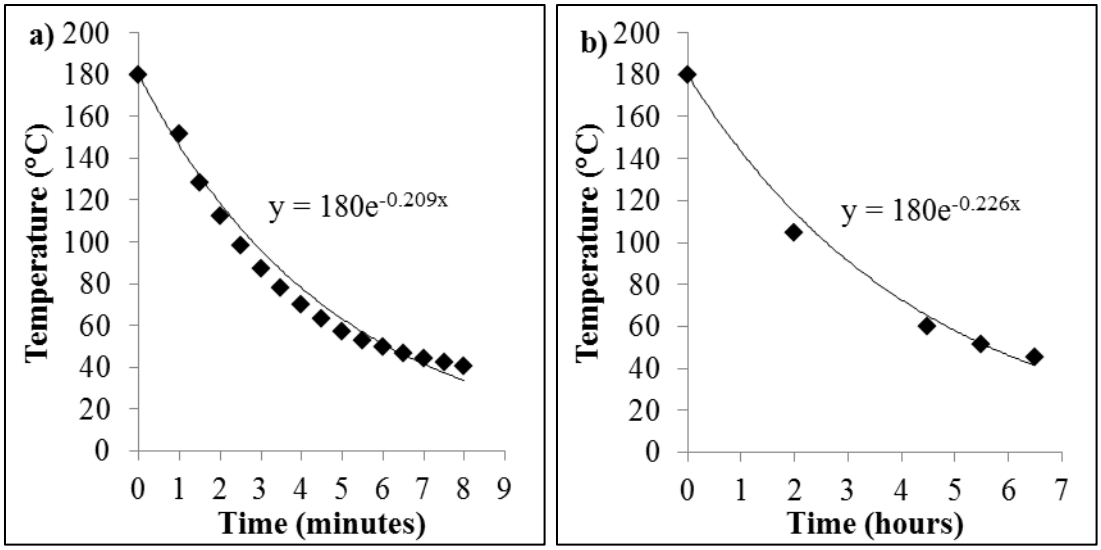

Figure 2.5 Compression molding cooling rates for a) fast cooling and b) slow cooling

2.2.2 Solution Casting, SoC

Dissolution of the polymer and solution casting was used as an alternative method to make the composite films in order to compare the effect of the manufacturing method on the properties of the films. A 20 wt% PLA/chloroform solution was prepared by stirring PLA pellets in chloroform on a hot stage for ~5 hours at ~30 °C. A 1 wt% suspension of GNP/chloroform was then sonicated at 30% amplitude for 30 minutes using a Misonix S-4000 ultrasonic processor with a 1/2″ probe size. The nanocomposite films were then fabricated by combining the 20 wt% PLA/chloroform solution and 1 wt% GNP/chloroform suspension at appropriate ratios to produce ~200 μm thick films of 0-15 wt% GNP content. The films were then dried in a vacuum oven at ~45°C for ~10 days to remove any remaining solvent. Alternatively, the drying process was sped up by removing the solvent through hot pressing the films.

2.2.3 Electrospinning / Compression Molding, E-CM

In addition to melt mixing and melt-spinning of composite fibers, fibers were also made using electrospinning. The electrospinning was performed in Dr. Mohammad Naraghi's laboratory at Texas A&M University. A 10 wt% solution of PLA in chloroform was first prepared by stirring with low heat to dissolve the PLA pellets. The appropriate ratio of CNT to produce the desired composite composition was added to dimethylformamide (DMF) and sonicated for 3 hours to homogenize. Then, the CNT/DMF suspension was added to the PLA/chloroform solution and stirred for 1 hour. The electrospinning was performed under ambient conditions using a rotating collector and applied voltage of 16 kV. The distance between the syringe tip and the collector was 15 cm and the feeding rate of the solution was 100 μL/hour. Due to the relatively high viscosity of the CNT/PLA/chloroform/DMF solution, the amount of CNT in the electrospun fibers was limited to 1 wt%. The 0 wt% or 1 wt% CNT/PLA electrospun composite fibers were then compression molded into films with a thickness of ~110 μm using a manual four-column 12 ton Carver hydraulic press (model 4122) with controlled cooling. The compression molding conditions were identical to the conditions outlined in 2.2.1 and the films were cooled at ~0.4°C/min using ambient temperature air cooling.

2.3 Characterization

The morphology and structure of the films was examined using scanning electron microscopy (SEM). Both a Zeiss Ultra60 FE-SEM, at an accelerating voltage of 5 kV, and a Hitachi SU8230 cold field emission FE-SEM, at an accelerating voltage of 10kV were used. The samples were first coated with gold using a Cressington Sputter Coater

108 (model 6002) at ~0.08 mbar and ~30 mA using a 30 second deposition time to eliminate charging.

Surface composition of the CNT and GNP was examined using X-ray photoelectron spectroscopy (XPS), Thermo K-alpha XPS, with Al Kα radiation at an excitation energy of 12 kV coupled with an ionized argon flood gun. A step size of 1 eV and pass energy of 200 eV was used for the wide scans, while a step size of 0.1 eV and pass energy of 50 eV was used for the high-resolution scans.

The thermal transitions and crystallization behavior was examined using thermogravimetric analysis (TGA), TA Instruments SDT Q600, and differential scanning calorimetry (DSC), TA Instruments DSC Q2000. For TGA, 7-15 mg samples were prepared in alumina pans and heated from 30°C to 600°C in argon at a rate of 5°C/min. For DSC, 5-7 mg samples were prepared in standard Tzero aluminum pans, equilibrated at 20°C, and held isothermal for 5 minutes. The samples were heated to 175°C at a rate of 5°C/min and then cooled down to 20°C at a rate of 5°C/min. The degree of crystallinity was calculated using the first DSC heating cycle to capture the thermal history, a result of the processing conditions. The crystal structure of the films was determined using wide-angle X-ray diffraction (WAXD) and polarized optical microscopy (POM). WAXD measurements were performed using an X'Pert Pro Alpha 1 (PANalytical, Almelo, Netherlands) diffractometer (Cu Kα radiation, $\lambda = 1.541$Å) The diffraction patterns were collected from a 2θ angle of 8° to 40° with a step size of ~0.02. (The diffractometer operated at 45 kV and 40 mA). Isothermal crystallization was also performed and captured using POM with a Leica DFC420 optical microscope coupled with cross polarizers and an Instec HCS302 hot stage. Samples were heated to 200°C and held

isothermally for ~3 minutes to homogenize, then isothermal crystallization was performed at 135°C or 140°C.

The electrical response of the films was measured using impedance spectroscopy (IS), which is closely related to dielectric spectroscopy and measures the current, voltage, and phase angle over an extensive range of frequencies [44]. A Solartron 1260 Impedance/Gain Phase Analyzer along with a 1296 Dielectric Interface was used to measure in the 0.1 Hz – 10 MHz frequency range using an in-plane configuration [45].

Thermo-mechanical properties were investigated using dynamic mechanical analysis (DMA), TA Instruments DMA Q800. Rectangular specimens with a width of ~3 mm and gauge length of ~10 mm were equilibrated at 35°C and held isothermal for 5 minutes. The samples were then heated at 3°C/min to 100°C. The tests were conducted at a frequency of 1 Hz and a strain amplitude of 12 μm. The tensile properties were examined using rectangular shaped specimens with a gauge length of 40 mm and width of 10 mm. The rate of grip separation was 12.5 mm/min in accordance with ASTM D882. An Instron 33R4466 and a 10 kN load cell were used.

CHAPTER 3

EFFECT OF NANOFILLER CHARACTERISTICS AND POLYMER CRYSTALLINITY ON THE PROPERTIES OF EXFOLIATED GRAPHITE NANOPLATELET / POLYLACTIC ACID FILMS

The focus of this chapter is to fabricate biodegradable GNP/PLA conductive films using scalable-manufacturing methods and investigate how the processing conditions for the given method affect the properties of the films. The incorporation of graphitic nanofillers for enhancing electrical conductivity of PLA and other thermoplastic polymers has previously been explored [31, 46, 47]. The distribution and dispersion of a nanofiller throughout the matrix has been shown to be governed by the compounding and manufacturing method employed [31]. A heterogeneous or poor dispersion and distribution of GNP have been shown to facilitate electrical percolation in PLA nanocomposites [46]. Percolation threshold is referred to as the minimum volume fraction of conductive filler required to form an interconnected network of conducting particles, usually denoted by a dramatic increase of several orders of magnitude in electrical conductivity [48]. Percolation threshold depends highly on the microstructure of the composite with primary contributing factors including the filler size, shape, distribution, and dispersion [49, 50], inherent material properties of the filler and matrix, such as conductivity [51], and the physical properties of the polymer matrix, such as crystallinity [52-54]. For example, Tait et al. reported that a randomly distributed network of nanofiller achieved via melt compounding / compression molding, as opposed

to a partially aligned nanofiller network achieved via melt compounding / injection molding, helps facilitate an interconnected conductive network, therefore lowering the percolation threshold of the composite [31].

This chapter examines the role of both distribution and dispersion and polymer matrix crystallinity on composite film properties for the same filler type, GNP. Specifically focusing on how the differences in distribution and dispersion, achieved by altering the compounding method, coupled with the physical properties of the polymer matrix, i.e., crystallization behavior, affect the electrical response of GNP/PLA films. While the conductivity of GNP/PLA has been studied [46, 47], the effect of the processing conditions on the conductivity has not yet been investigated for this composite system. Kalaitzidou et al. [40] found for GNP/PP composites, both FC and SC composites had the same degree of crystallinity, but the SC composites exhibited significantly higher electrical conductivity compared to the FC ones with the same GNP content. The increased conductivity of the SC composites was attributed to a 20-30% increase in crystallite size compared to the FC composites, thus due to GNP being a nucleating agent, the spherulites grew around the platelets, therefore the fewer, but larger spherulites meant that fewer GNP were trapped inside the spherulites and more were outside forming the conductive network [40]. To investigate the effect of processing conditions on the electrical response of GNP/PLA films, two different compounding methods, 1) melt mixing, followed by compression molding (MC-CM), and 2) solution mixing, followed by solution casting (SoC) are employed and two different cooling rates during compression molding are used, fast cooling (FC) and slow cooling (SC). The melt compounding and solution compounding processes used in this study may employ

different amounts of energy during compounding, which is important to note when directly comparing two compounding methods. By altering the processing conditions, the crystallization characteristics of the PLA were significantly altered and thus correlation between polymer crystallinity and electrical response of the films was established.

3.1 Morphology and Dispersion

Representative SEM images of the cryo-fracture surface of the 15 wt% GNP films fabricated by all three processing methods and conditions: FC, SC, and SoC are shown in Figure 3.1a through f. The difference in GNP distribution between the films can be seen in the low magnification images shown in Figure 3.1a, c, and e. Both the 15 wt% FC and SoC films show a homogeneous distribution of GNP as indicated in Figure 3.1a and e, respectively. Upon further magnification, Figure 3.1b and f, GNP and minimal GNP agglomerates, indicated by arrows, can easily been seen. However, the GNP is not as apparent in the 15 wt% SC film and is more heterogeneously distributed, shown in Figure 3.1c and d. Due to the slow cooling rate used during fabrication, the SC films are expected to have a high degree of crystallinity. Furthermore, GNP has been previously reported to act as a nucleating agent, promoting crystallization [40]. The GNP may not be as visible in the SC films because some of the GNP is trapped in crystalline spherulites, therefore making them less apparent. The crystallization behavior of the films was studied in detail in order to better understand the microstructural differences seen in the morphological study.

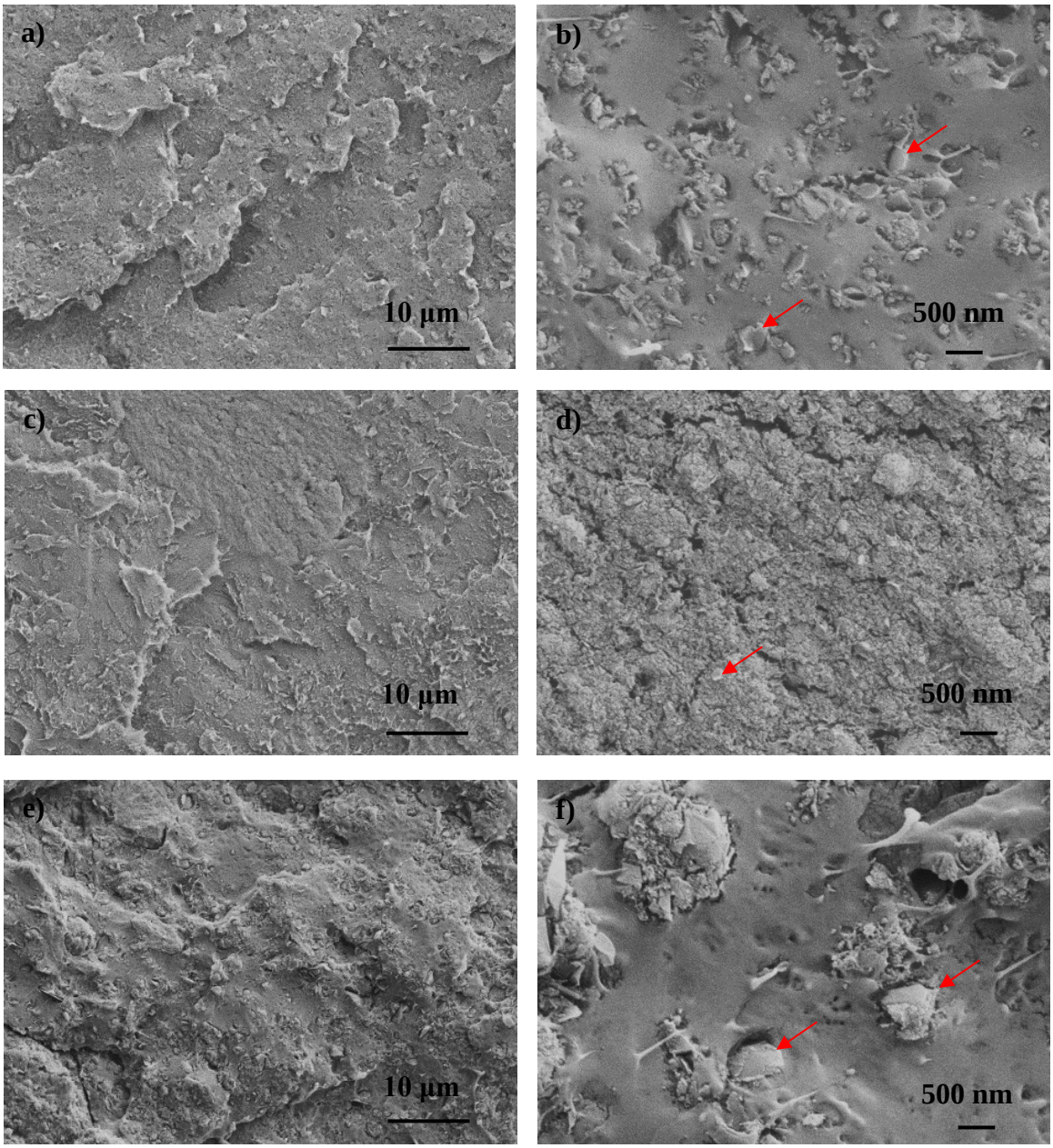

Figure 3.1 Representative cross sectional SEM images of 15 wt% GNP/PLA cryo-fracture surfaces a) FC at low magnification, b) FC at high magnification, c) SC at low magnification, d) SC at high magnification, e) SoC at low magnification, and f) SoC at high magnification. Arrows indicate GNP.

3.2 Crystallization Characterization of Composite Films

The rate of cooling during the compression molding of the films was varied in order to alter the crystallization behavior of the PLA matrix and investigate how the crystallization characteristics affect the mechanical and electrical properties of the films. Initial heating thermograms, seen in Figure 3.2, were used to characterize thermal transitions and degree of crystallinity. The glass transition temperature (T_g) and the degree of crystallinity (χ), calculated using equation (3.1), are shown in Table 3.1.

$$\chi = \frac{\Delta H_m + \Delta H_c}{\Delta H_m^{\circ}(1 - wt\%/100)} \times 100 \tag{3.1}$$

where χ is the degree of crystallinity, ΔH_m is the melting enthalpy of the sample, ΔH_c (< 0) is the cold crystallization enthalpy of the sample, ΔH°_m is the theoretical melting enthalpy of 100% crystalline PLA, ΔH°_m = 93 J/g was used [55], and *wt%* is the nanofiller content.

Table 3.1 Effect of compounding and processing conditions on the degree of crystallinity (χ) and glass transition temperature (T_g) for FC, SC, and SoC GNP/PLA films

	χ (%)			T_g (°C)		
	FC	**SC**	**SoC**	**FC**	**SC**	**SoC**
0wt% GNP	0.8±0.8	37.5±1.6	33.2±0.8	58.4±0.4	61.1±0.3	63.9±3.5
1wt% GNP	0.2±0.3	37.8±1.0	32.5±1.1	58.3±0.2	60.5±0.3	66.9±1.2
5wt% GNP	0.8±0.5	39.0±1.2	33.0±1.0	58.3±0.3	60.7±0.4	62.7±0.4
8wt% GNP	1.0±0.3	34.4±0.7	32.4±0.8	55.7±0.8	59.7±0.1	60.9±1.2
10wt% GNP	2.3±0.1	37.7±0.8	29.5±3.1	59.6±0.2	62.0±0.2	59.6±0.4
12wt% GNP	0.7±0.5	35.3±1.4	27.1±0.4	55.8±1.0	59.2±1.3	61.4±1.2
15wt% GNP	2.5±0.7	42.0±0.8	24.5±2.2	58.1±0.3	59.8±0.4	63.2±1.9

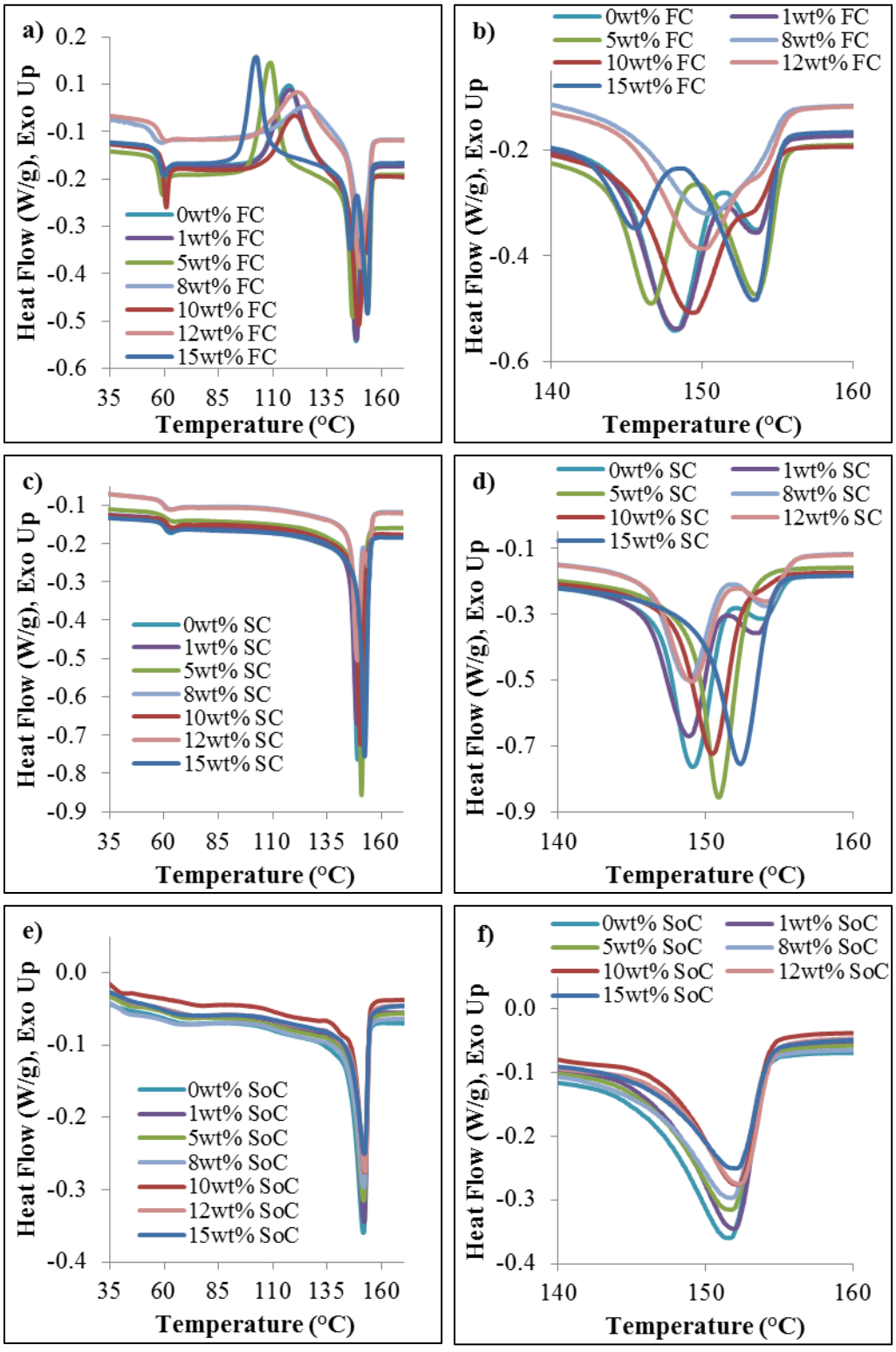

Figure 3.2 Non-isothermal initial heating thermograms of a) FC, b) FC melting endotherm, c) SC, d) SC melting endotherm, e) SoC, and f) SoC melting endotherm

There is no statistically significant trend in T_g as a function of GNP content for either the FC, SC, or SoC films. However, the FC films displayed a slightly lower overall T_g compared to the SC and SoC films. The lower T_g and degree of crystallinity of the FC films is attributed to the high polymer chain mobility compared to the SC and SoC films. The FC films also displayed extremely low crystallinity (~0.2-2.5%) and no significant trend in crystallinity as a function of GNP content, as shown in Table 3.1. The fast cooling rate during compression molding does not allow enough time for the polymer chains to organize into crystalline lamella resulting in a highly amorphous polymer structure. Furthermore, as seen in Figure 3.2a, the FC films display cold crystallization peaks which are in good agreement with the highly amorphous structure. In contrast, the SC and SoC films display a much higher crystallinity in the range of ~37-42% and ~25-33%, respectively, as shown in Table 3.1, and do not display cold crystallization peaks, seen in Figure 3.2c and e. For both the SC and SoC films, the polymer chains were given more time to organize into crystalline lamella due to the decreased cooling rate during compression molding for the SC films or the slow evaporation of the chloroform for the SoC films. Furthermore, chloroform, used to dissolve the polymer, leads to highly crystalline PLA due to its good polymer-solvent interactions [30]. It is noted, as seen in Figure 3.2e, that the SoC films have a much broader glass transition region compared to both the FC and SC films indicating that the solvent acts as a plasticizer [56]. Furthermore, the degree of crystallinity increases with the addition of GNP for the SC films and decreases with the addition of GNP for the SoC films. GNP has been shown to act as a nucleating agent [57], promoting crystallization which explains the increase in crystallinity in the SC films with the increase in GNP content. The opposing trend for the

SoC films suggests the GNP is hindering crystallization which has also been previously reported in the case of organoclay that is highly exfoliated and highly miscible in PLA [58]. As seen in Figure 3.2d, four of the SC films, the control PLA, 1 wt%, 8 wt%, and 12 wt% GNP/PLA, display double melting behavior. The other SC films, containing 5 wt%, 10 wt%, and 15 wt% GNP, displayed a single melting endotherm. A double melting endotherm indicates either polymorphism, multiple crystal phases, or melt-recrystallization [59]. Melt-recrystallization occurs when semi-melted crystals present in the PLA melt, recrystallize instead of melting further. Finally, the recrystallized crystals melt as the temperature increases [59]. Further investigation of this behavior was explored by examining the diffraction patterns of the films.

The crystal structure of PLA is comprised of three main crystal phases referred to as α, β, or γ [60]. There is a secondary disordered α' phase that can form at low crystallization temperatures and can be converted to the α crystal phase at temperatures greater than 120°C [60]. The most stable and prevalent of the three main crystal phases is the pseudo-orthorhombic, helical α phase [60-62]. Diffraction patterns for the FC, SC, and SoC films are shown in Figure 3.3a, b, and c. None of the films show evidence of polymorphism or changes in crystal structure as a function of GNP content. The only crystal phase present is the primary α phase. Thus, it is concluded that the double melting peaks observed in Figure 3.2b and d are due to melt-recrystallization as the films are heated, rather than polymorphism. The FC films display a broad maximum around 2θ = 16.7° independent of GNP content. The extremely broad maximum is indicative of a highly amorphous structure, which is in agreement with the low crystallinity, calculated using the thermograms obtained, seen in Figure 3.2. As the GNP content increases, the

characteristic graphitic peak emerges at ~26.6°. Using Bragg's Law, the d-spacing associated with this peak can be calculated. The 2θ peak of ~26.6° corresponds to the d-spacing between graphite sheets in regularly spaced graphite or basal plane distance of graphite, 3.35Å [46, 63]. This indicates the presence of GNP in the composite films. However, in the SC and SoC films, the characteristic graphitic peak is less prevalent due to the highly crystalline PLA dominating the behavior, but is shown in Figure 3.4. The sharp diffraction peaks, seen in Figure 3.3b and c, for both the SC and SoC films indicate high crystallinity and is in agreement with the degree of crystallinity calculated from the initial heating thermograms reported in Table 3.1.

The SC films display characteristic peaks of crystalline PLA at 2θ = 15.0°, 16.7°, 19.1°, and 22.4°. These crystalline peaks correspond to all α crystal phase with the characteristic planes of (010) [64], (200+110) [62], (203) [64], and (121) [64], respectively. There is also some indication of a weak reflection at 31.3° in the SC films which corresponds to the (0010) plane of the hcp crystal phase [61]. The dominate crystalline peaks associated with the SoC films are at 2θ = 16.7°, 19.1°, and 22.4° and are associated with the characteristic planes of (200+110) [62], (203) [64], and (121) [64]. There is also some indication of a weak reflection at 2θ = 15.0° which corresponds to the α phase characteristic plane (010) [64].

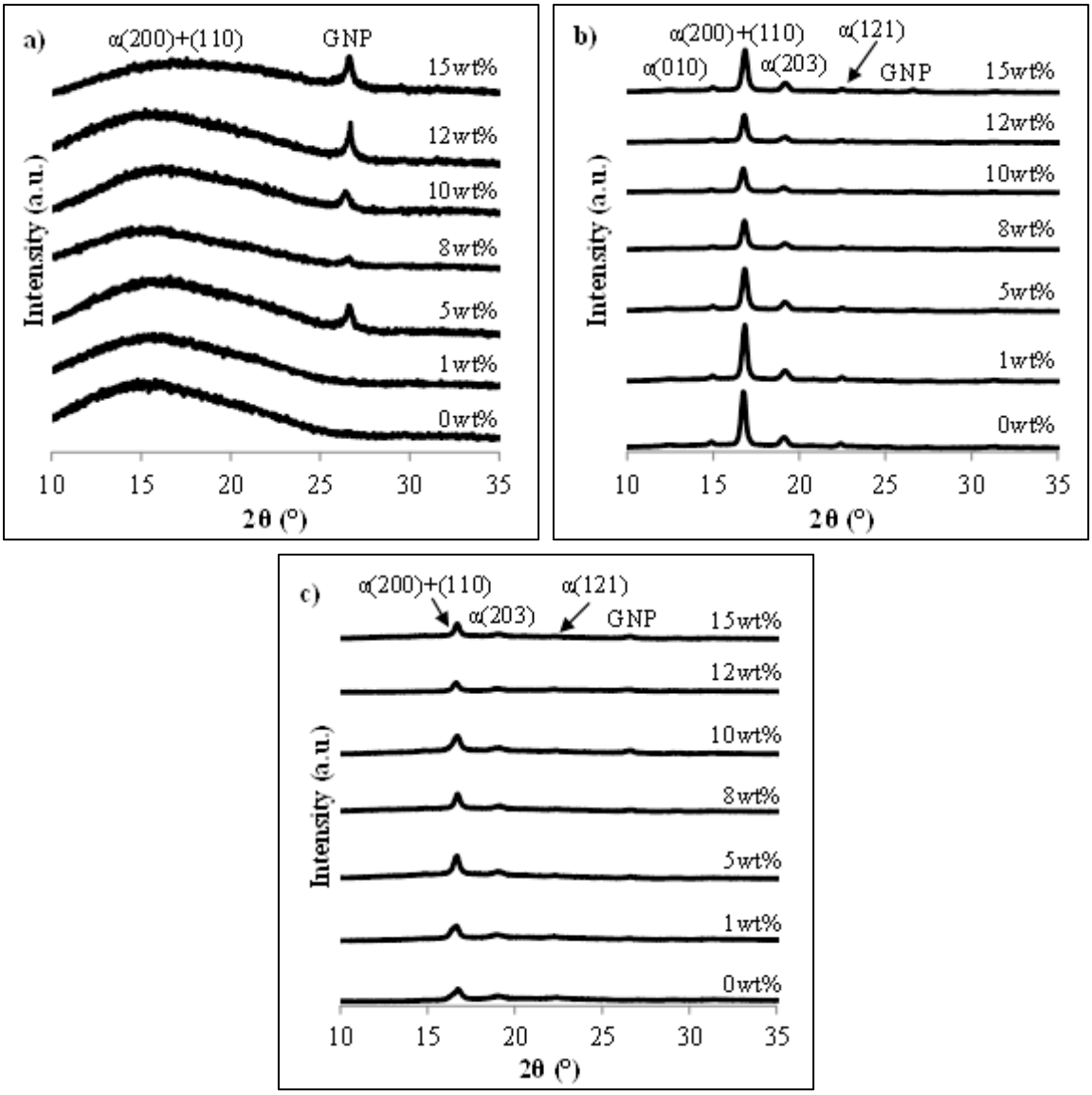

Figure 3.3 Diffraction patterns obtained for the a) FC, b) SC, and c) SoC films as a function of GNP content

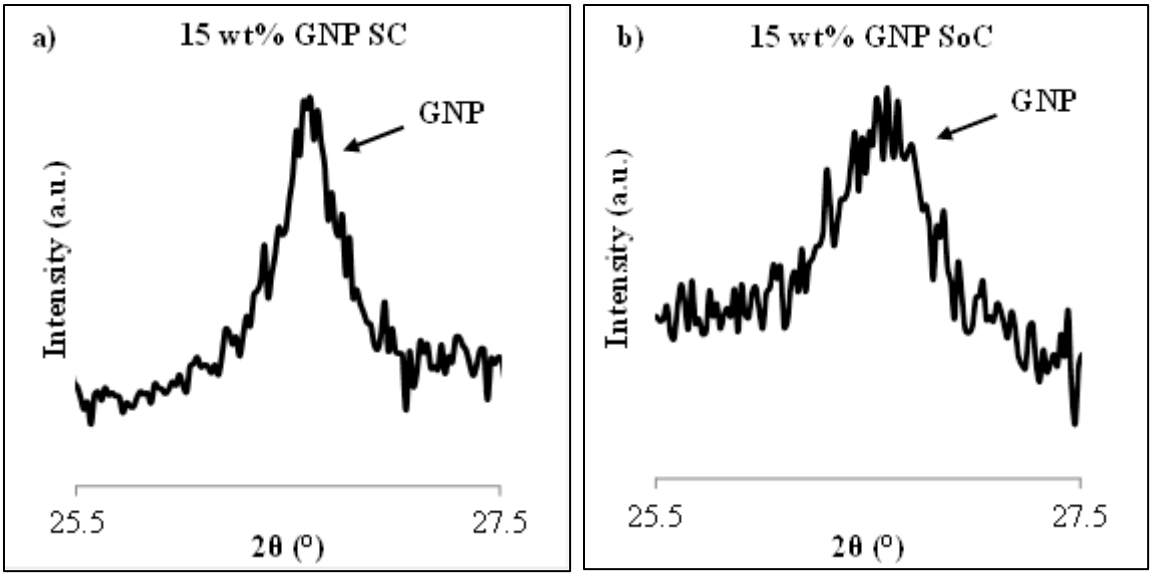

Figure 3.4 Characteristic graphitic peak of the a) SC and b) SoC films

The degree of crystallinity and crystal structure are two characteristics of the crystallization behavior of the films. A third aspect is the average lamella thickness which can be determined using the Scherrer equation (3.2):

$$L = \frac{K\lambda}{Bcos(\theta)} \tag{3.2}$$

where L is the apparent crystalline lamella thickness, K is a dimensionless shape factor (0.9 was used as an approximate for the spherulite structure [65]), λ is the radiation wavelength, B is the full width at half maximum value of the diffraction peak, and θ is the Bragg angle. The average lamella thickness for the two dominant diffraction peaks at 16.7° and 19.1° for the SC and SoC films was calculated to compare the effect of compounding method on lamella thickness. It is important to note that the 16.7° diffraction peak corresponds to two crystal planes, (200) and (110) and thus the information obtained cannot be directly related to the thickness of one crystal type. As

seen in Figure 3.5a and b, the SC films have a greater average lamella thickness than the SoC films for both dominant peaks. The SC films have a slightly higher degree of crystallinity, as seen in Table 3.1, and therefore the increase in average lamella thickness indicates that the SC films have slightly thicker crystalline regions, but a comparable number of crystals to the SoC films. Furthermore, the lamella thickness for both the SC and SoC films does not change significantly with increased GNP content indicating the increase in crystallinity of the SC films with increased GNP content is due to the presence of more crystals not thicker crystals and the decrease in crystallinity of the SoC films with increased GNP content is due to the presence of fewer crystals of comparable size.

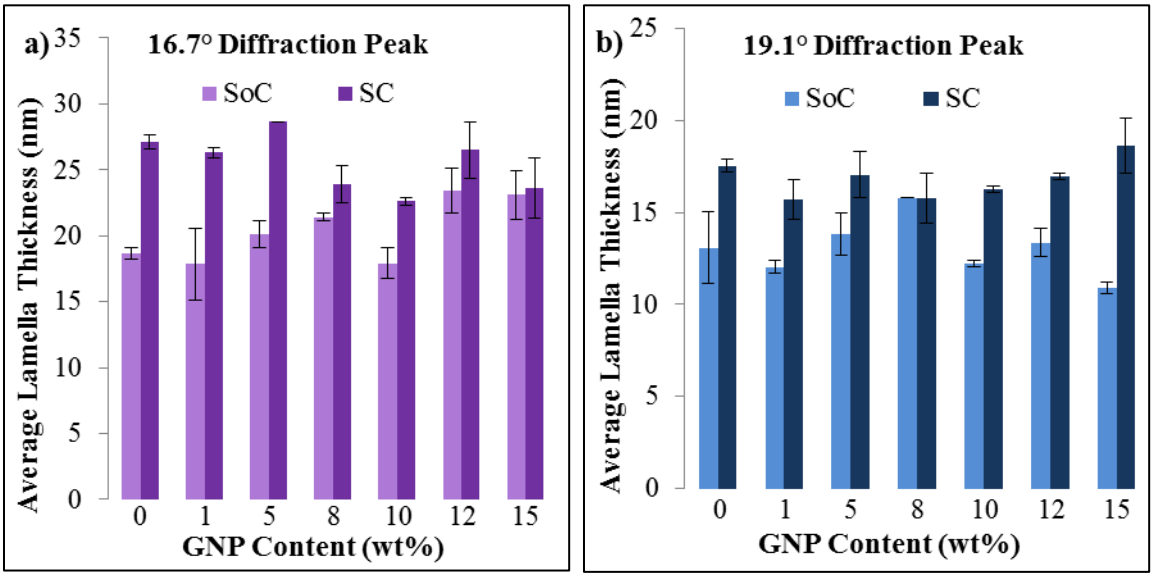

Figure 3.5 Average crystal lamella thickness of the two dominant diffraction peaks, a) 16.7° and b) 19.1°, for the SC and SoC films as a function of GNP content

The differences in crystallization behavior as a function of processing conditions was further explored using isothermal crystallization studies, at 135°C, of both the 0 wt% GNP and 1 wt% GNP films using polarized optical microscopy (POM). As seen in Figure 3.6, both the 0 wt% GNP and 1 wt% GNP films showed similar spherulite size. However, as evident in Figure 3.6, the crystallization of the 0 wt% GNP film was homogeneous, while the crystallization of the 1 wt% GNP film displayed heterogeneous crystal growth concentrated around the GNP, indicated by the arrow in Figure 3.6. This further supports that GNP is promoting nucleation in the MC-CM films and the average lamella thickness remains constant with GNP content. By altering the processing conditions of the composite films, the physical properties of the PLA matrix, specifically crystallinity, can be modified.

It is noted that the effect of processing conditions, that is the cooling rate during compression molding, has a much more significant influence on the crystallization characteristics compared to the effect of compounding method. The influence of the GNP distribution and dispersion coupled with crystallization behavior on the elastic modulus is examined below.

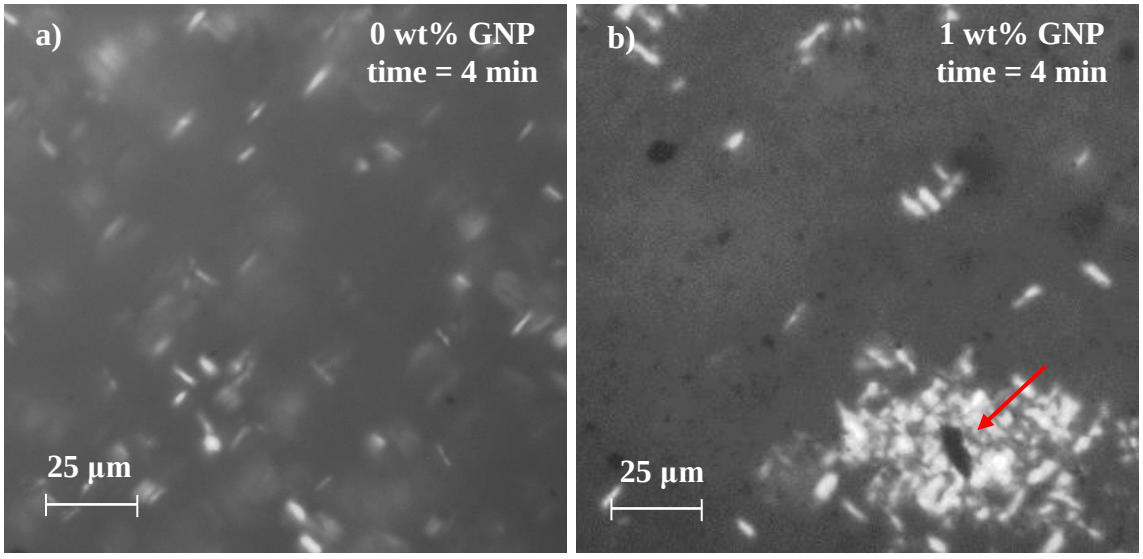

Figure 3.6 Representative POM image of isothermal crystallization at 135°C of a) 0 wt% GNP and b) 1 wt% GNP films at 4 minutes after nucleation was observed, time = 4 minutes

3.3 Effect of GNP Distribution/Dispersion and Polymer Crystallinity on the Elastic Modulus

The elastic modulus, *E*, of the FC, SC, and SoC GNP/PLA films is shown in Figure 3.7. The *E* increases with GNP content for all of the films, indicating good interfacial interaction between the GNP and the polymer matrix [66]. At constant GNP content, the SC films display the highest *E* of ~3.85 GPa for the 15 wt% film, followed by the FC films of ~3.37 GPa for the 15 wt% film, and finally the SoC films of ~2.32 GPa for the 15 wt% film. The significantly lower *E* of the FC films compared to the SC films can be attributed to the difference in crystallinity. The high crystallinity of the SC films increases the modulus by hindering the molecular mobility [67]. However, the SC and SoC films have very comparable crystallization behavior, yet there is a significant

discrepancy in mechanical response. The lower modulus of the SoC films compared to the SC films may be due to the micro-porosity present in the SoC films due to lack of compression during processing and/or remnant chloroform in the film acting as a plasticizer and reducing the modulus. It has previously been reported that a small amount of solvent remaining in the film after solution casting may reduce the intermolecular forces in PLA, thus causing the film to have a lower modulus [56].

To improve the modulus of the SoC films, representative GNP/PLA SoC films of 0 wt% and 5 wt% were compression molded at a slightly elevated temperature of 120°C (above T_g, but below melting) and are referred to as solution cast / compression molded (SoC-CM) films. As seen in Figure 3.7, the SoC-CM films exhibited a higher modulus than the SoC films. There are three potential underlying mechanisms for the increase in modulus after compression molding: 1) decrease in micro-porosity of the films, 2) elimination or decrease of remnant chloroform through evaporation due to the combined effect of elevated temperature and pressure, and/or 3) change in crystallinity upon heating and slow cooling.

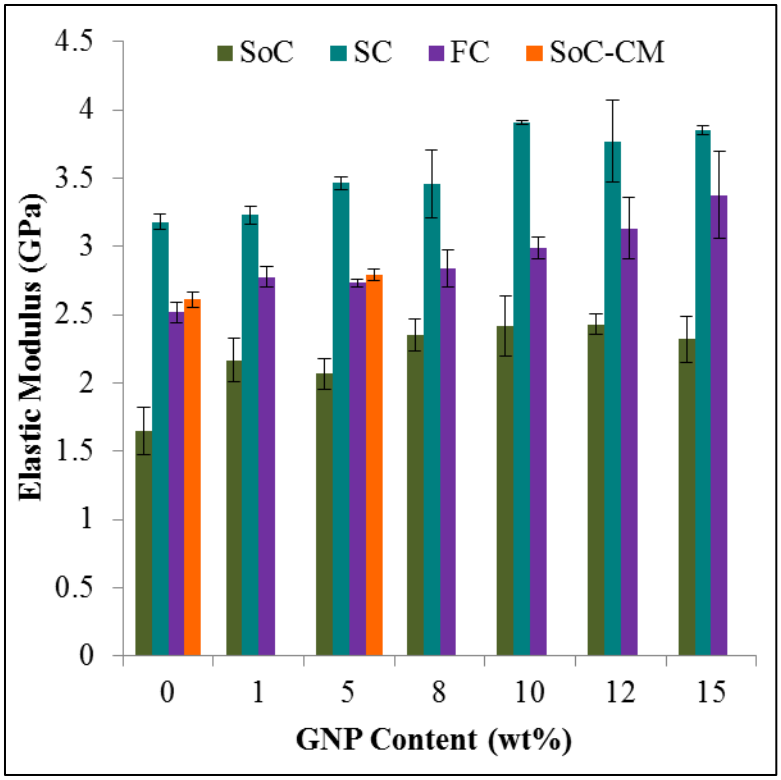

Figure 3.7 Elastic modulus of FC, SC, SoC, and SoC-CM GNP/PLA films as a function of GNP content

The initial heating thermograms shown in Figure 3.2e indicated there could be remnant chloroform present in the SoC films, so TGA was performed. As seen in Figure 3.8, there is a 5-6% drop in weight between ~95°C and ~135°C indicating the presence of fluid in both the 5 wt% SoC and 5 wt% SoC-CM films. To confirm that the fluid present was chloroform (boiling point of ~61°C) and not water (boiling point of ~100°C) absorbed from the humidity in the atmosphere, as-received PLA pellets and a 0 wt% SoC film were used as the controls. The as-received PLA pellets did not show this fluid content and both the pellets and films are stored in sealed containers under the same conditions. However, the difference in remnant chloroform content is not statistically

significant between the SoC and SoC-CM films; therefore this is not the dominating mechanism for the difference in mechanical response.

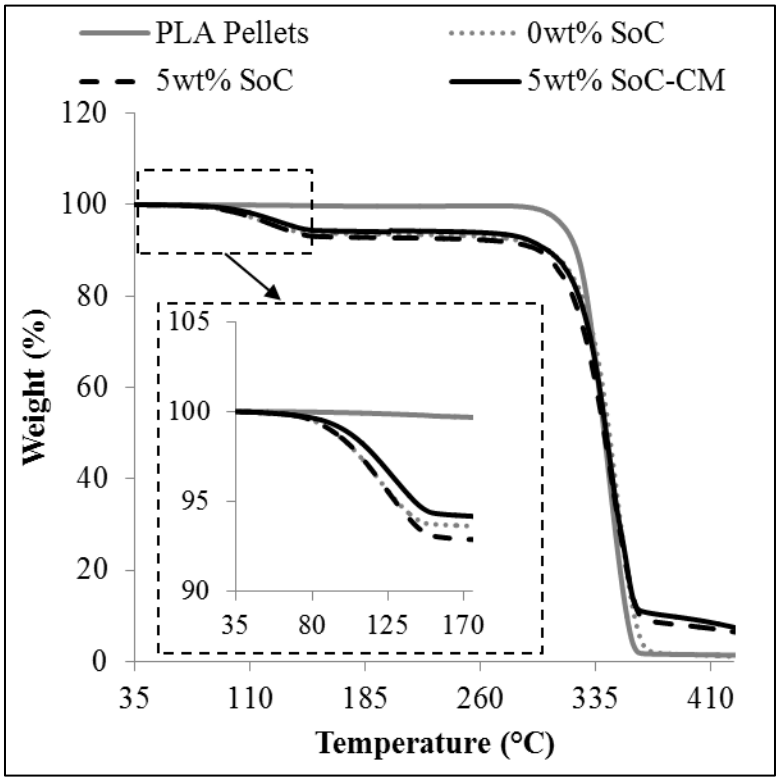

Figure 3.8 Representative TGA of as-received PLA pellets, 0 wt% SoC film, 5 wt% SoC film, and 5 wt% SoC-CM film

Additionally, initial heating thermograms, seen in Figures 3.9a, were used to compare crystallization characteristics of the films in order to identify whether or not the change in mechanical response is related to altering the crystallization behavior of the films upon compression. The cross sectional SEM seen in Figure 3.9c and d may not be representative of the entire sample; however, overall there was a significant decrease in micro-porosity upon compression, but the degree of crystallinity is comparable for both the 5 wt% SoC and the 5 wt% SoC-CM films. The degree of crystallinity of the 5 wt%

SoC films is 33.0 ± 1.0% and that of the 5 wt% SoC-CM films is 32.9 ± 0.4%. It is also important to note that there is a significant decrease in T_g upon compression, as seen in Figure 3.9a, compared to both the as-received pellets and the SoC film. A decrease in T_g with the addition of nanofillers has been well documented and is typically indicative of poor nanofiller dispersion and/or poor interactions between the nanofiller and the polymer matrix [68, 69]. However, the compounding method is identical for the 5 wt% SoC and 5 wt% SoC-CM films and there is no evidence of a significant change in distribution or dispersion, so this is not the dominating mechanism for the decrease in T_g upon compression. Furthermore, there is no statistically significant change in remnant chloroform between the 5 wt% SoC and 5 wt% SoC-CM films; therefore the decrease in T_g is not attributed to the chloroform content in the 5 wt% SoC-CM film. However, it has also been reported that changes in molecular entanglement and free volume due to the addition of nanofillers can alter the T_g [70]. Because the significant change in T_g occurs upon compression at elevated temperature, it is hypothesized that changes in molecular entanglement and/or free volume is contributing to the decrease in T_g.

Finally, diffraction patterns were obtained for both the 5 wt% SoC and 5 wt% SoC-CM films to identify whether there was a change in crystal phase upon compression and compare the average lamella thickness. As seen in Figure 3.9b, both films displayed only α phase crystals and there was only a small change in lamella thickness, calculated using equation (3.2), upon compression. The average lamella thickness of the 16.7° peak did increase slightly from 20.1 ± 1.0 nm to 24.0 ± 0.4 nm upon compression; however there was no statistically significant change in lamella thickness for the 19.1° peak. The change in spherulite size is very minimal and therefore is not believed to be a dominating

mechanism for the change in mechanical response. It is concluded that the dominating mechanism for the increase in modulus upon compression is the decrease in micro-porosity of the films.

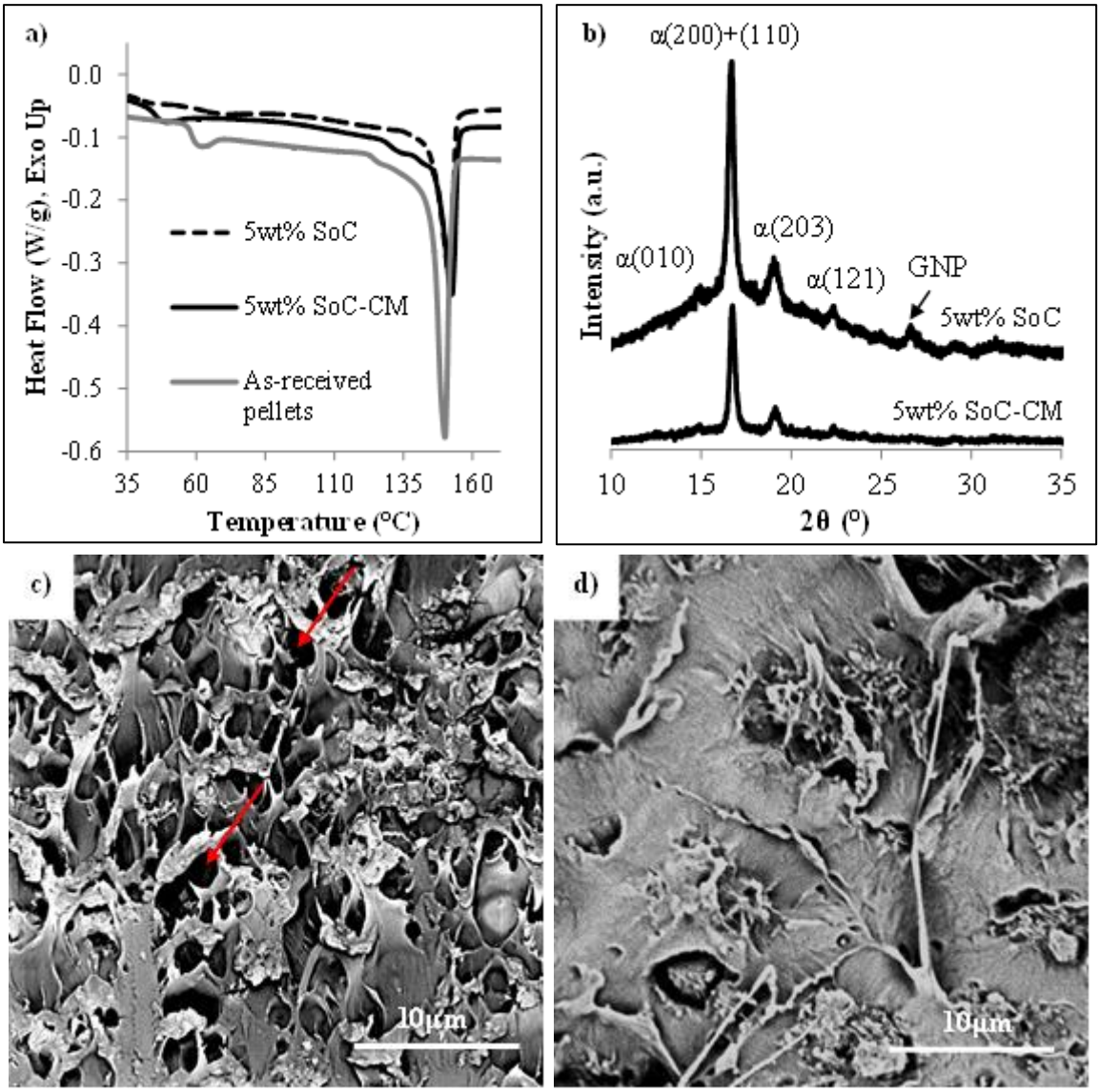

Figure 3.9 Comparison of crystallization characteristics of the 5 wt% SoC and 5 wt% SoC-CM films: a) initial heating thermograms compared to as-received pellets, b) diffraction patterns of films, and cryo-fracture surface SEM of c) 5 wt% SoC and d) 5 wt% SoC-CM. Arrows indicate microvoids.

3.4 Effect of GNP Distribution/Dispersion and Polymer Crystallinity on the Electrical Response

The frequency-dependent electrical response of the films was examined using impedance spectroscopy in order to ascertain more information on the film microstructure as well as the dielectric response. In composites, the degree of dispersion and matrix-filler interactions are critical factors influencing percolation behavior, not just conductive filler concentration [71]. Impedance spectroscopy measures the current, voltage, and phase angle over an extensive range of frequencies [44]. The complex impedance is governed by equation (3.3):

$$Z^*(\omega) = V(\omega)/i(\omega) \tag{3.3}$$

where the applied voltage, V, and the measured current, i, are:

$$V(\omega) = V_m \sin(\omega t) \tag{3.4}$$

$$i(\omega) = i_m \sin(\omega t + \vartheta) \tag{3.5}$$

The angular frequency, $\omega = 2\pi f$, is a function of frequency, f, ϑ is the phase angle, and V_m and i_m are the magnitudes of the voltage and the current, respectively.

In-plane (x-y plane) impedance spectroscopy measurements were performed and a schematic defining the measurement direction is shown in Figure 3.10. The impedance magnitude ($|Z^*|$) reported as a function of frequency at representative GNP concentrations for the FC, SC, and SoC films is presented in Figure 3.11. The drop in the low frequency impedance and loss of frequency dependence denotes conductive behavior and electrical percolation [72, 73]. In order to examine the effect of processing conditions i.e., cooling rate that strongly affects the polymer crystallinity, on the electrical response,

the FC and SC films, seen in Figure 3.11a and b, are compared. The FC films display highly insulating behavior up to 12 wt% of GNP, seen in Figure 3.11a, with a low frequency $|Z^*|$ in the order of 10^{12} Ω. However, at 15 wt% of GNP, the low frequency $|Z^*|$ drops to ~10^8 Ω, indicating percolation has occurred between 12 wt% and 15 wt% of GNP in the FC films. The percolation threshold for the SC films is much lower, between 1 wt% and 5 wt% of GNP, as seen in Figure 3.11b. The SC films display a significant drop in low frequency $|Z^*|$ at 5 wt% of GNP and exhibit a low frequency $|Z^*|$ of ~10^6 Ω at 15 wt% of GNP. The percolation threshold of the SoC films is between 5 wt% and 8 wt% of GNP and the value of the low frequency $|Z^*|$ is ~10^7 Ω at 15 wt% of GNP, as seen in Figure 3.11c. As more conductive filler is added into the composite, the low frequency $|Z^*|$ will tend to decrease, indicating an increase in conductance; however, due to the inherent heterogeneous structure of the composites this trend is not definitively seen. For example, this trend can be seen far from percolation at 15 wt% for the SC films, seen in Figure 3.11b, however close to the percolation threshold there is some fluctuation in low frequency $|Z^*|$ and the samples' behavior does not necessarily follow this trend.

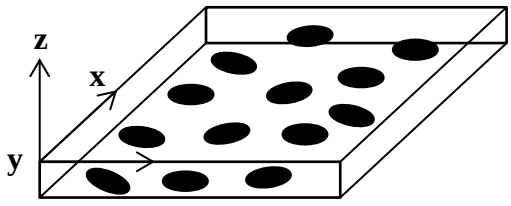

Figure 3.10 Schematic of GNP/PLA composite film

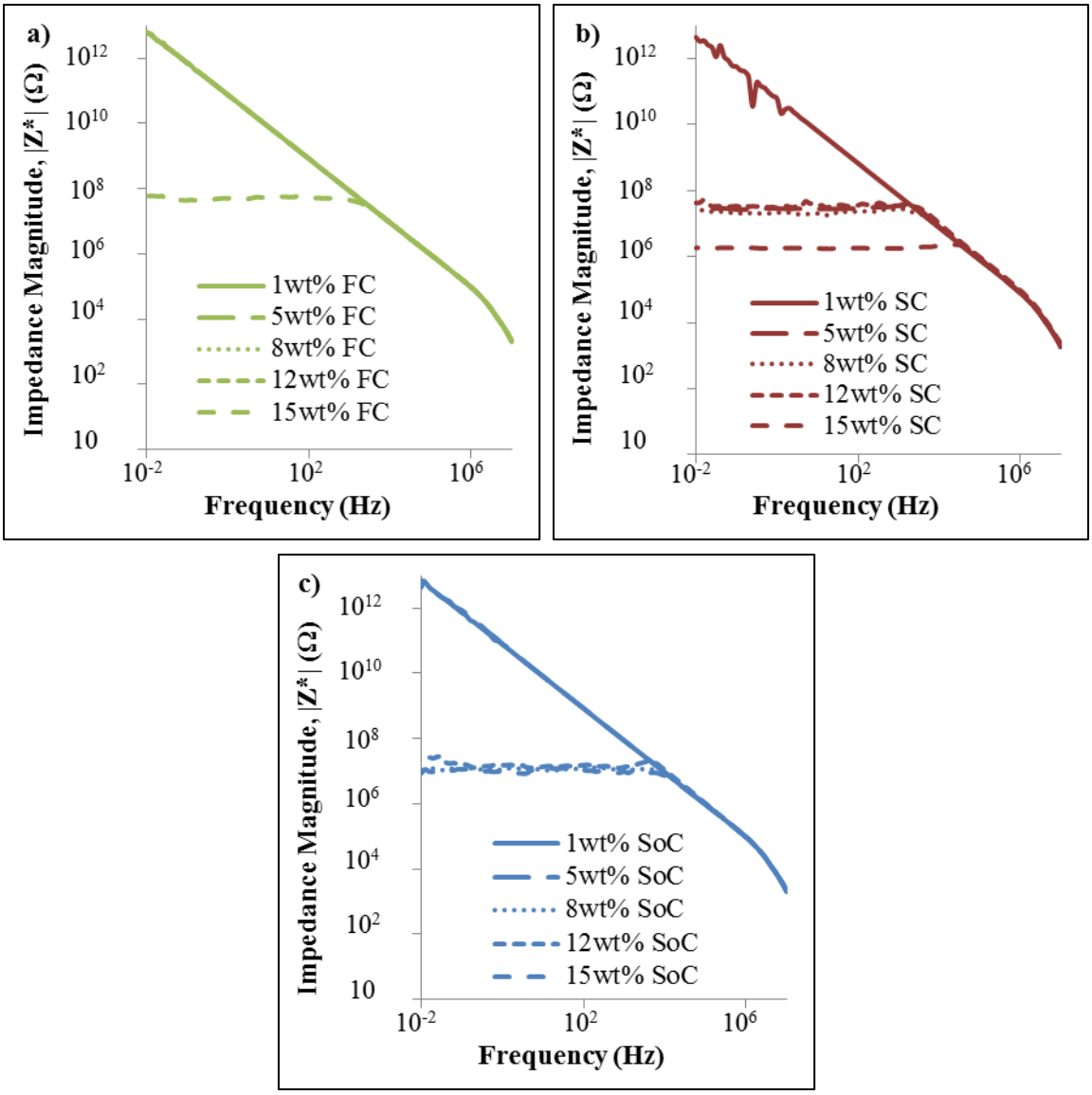

Figure 3.11 Representative runs of impedance magnitude, |Z*|, as a function of frequency for representative GNP concentrations for a) FC, b) SC, and c) SoC films

The percolation behavior of the films as a function of the GNP content can be seen in Figure 3.12. (Trend lines included in Figure 3.12 are visual guidelines and not indicative of any mathematical trend.) It is clear by the dramatic decrease in impedance that electrical percolation is achieved between 1 wt% and 5 wt% for the SC films, 5 wt%

and 8 wt% for the SoC films, and 12 wt% and 15 wt% for the FC films. In order to investigate the effect of processing conditions, specifically the polymer matrix crystallinity, the FC and SC films are closely examined. Isothermal and non-isothermal crystallization was performed using POM to simulate slow and fast cooling, respectively, confirming the drastic difference in crystallinity of the SC and FC films. (It is noted that 1 wt% films were used for the crystallization studies, to facilitate visualization, and as the average lamella thickness does not change with GNP content, the results can be correlated to the 15 wt% films.) In the case of non-isothermal crystallization, shown in Figure 3.13a, the composite was highly amorphous at room temperature whereas, isothermal crystallization resulted in spherulites forming around the GNP, shown in Figure 3.13b.

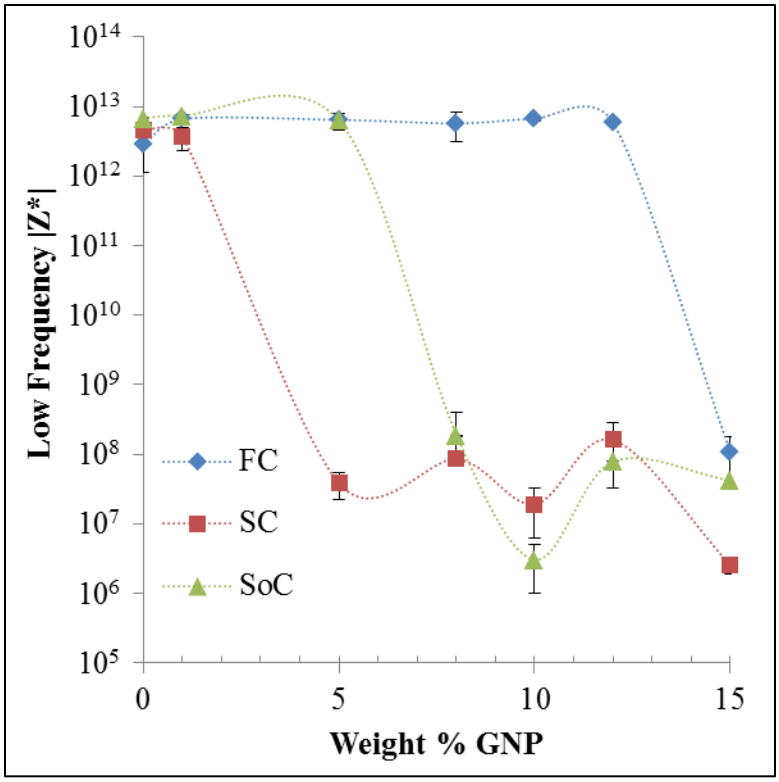

Figure 3.12 Low frequency impedance magnitude, |Z*|, as a function of GNP content for the FC, SC, and SoC films (trend lines included are visual guidelines and not indicative of any mathematical trend)

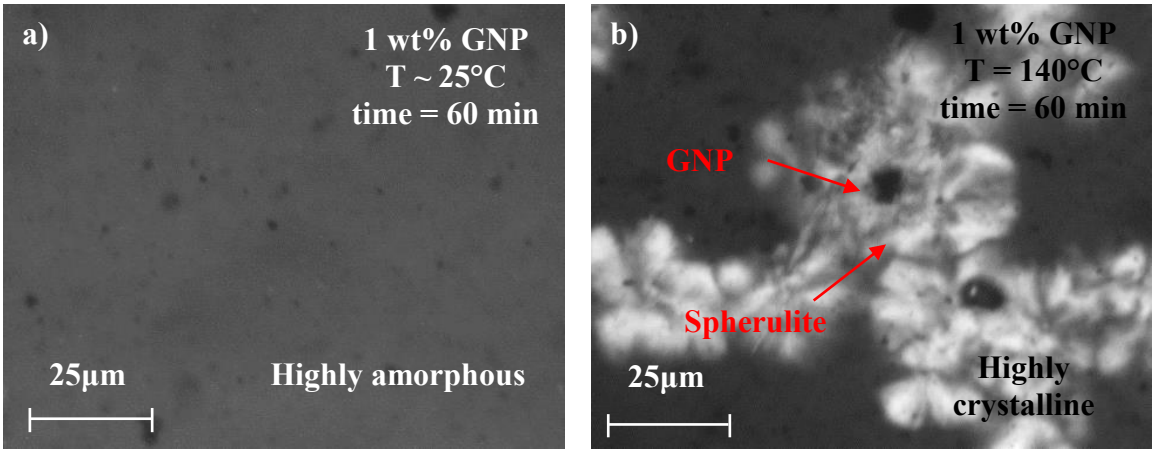

Figure 3.13 Representative POM image of a) non-isothermal (representative of FC) and b) isothermal (representative of SC) crystallization of 1 wt% GNP films

The morphological and crystallization studies show that the GNP dispersion and average crystal size remain constant in both the 15 wt% FC and 15 wt% SC films, indicating that the change in percolation threshold is due to the difference in crystallinity. Two possible primary mechanisms that contribute to this phenomenon are: 1) Difference in inherent conductivity of the constituents in the composite [51], namely the difference in electron transfer through crystalline versus amorphous phases [74] and 2) change in interparticle spacing of the conductive filler due to spherulite growth [53]. As previously reported [74], the efficiency of electron transfer in an insulating polymer, such as PLA, is dependent on the orientation of the polymer chains, particularly with respect to the direction of applied electric field. Ordered packing of crystalline regions will facilitate the transfer of electrons more favorably than disordered amorphous regions. Higher electrical conductivity and lower percolation threshold of the SC films is expected because the crystalline order at the GNP/polymer interface will lower contact resistance and result in less electron scattering. In addition to this mechanism, the excluded volume effect previously reported [53], may also contribute to the lower percolation threshold of the SC films. Specifically, the growth of spherulites will lead to more continuous conductive pathways through a more heterogeneous nanofiller distribution. For the SC films, the spherulites grow slowly around the GNP, as seen in Figure 3.13b, and GNP trapped outside of the spherulites are displaced leading to a more heterogeneous GNP network with higher chances of forming a continuous pathway through the PLA matrix. By altering the cooling rate during processing, the percolation behavior can be significantly altered due to the change in the crystallization characteristics of the polymer matrix.

The compounding method has significantly less of an effect on the electrical percolation than the processing conditions. The potential primary mechanisms for the difference in percolation threshold between the SC and SoC films are: 1) the better dispersion of the GNP throughout the matrix in the SoC films, 2) decrease in interparticle distance of the GNP due to spherulite growth in the SC films, 3) remnant chloroform in the SoC films altering the electrical response, and 4) possible voids in the SoC films due to evaporation of the solvent and lack of compaction, achieved through compression molding during processing. As seen in Figure 3.1, the SoC films have a better dispersion and distribution of GNP compared to the FC or SC films. This can be attributed to the decreased polymer viscosity during processing in the SoC films. The increase in percolation threshold of the SoC films, compared to that of the SC films, may be attributed to the excluded volume effect, i.e. a higher degree of amorphous regions in the matrix may lead to a more homogeneous filler distribution making a continuous conductive pathway more difficult to form [53]. The SC films have thicker crystalline regions and slightly higher degree of crystallinity compared to the SoC films, indicating the increased degree of crystallinity is due to the thicker crystalline regions. As the spherulites grow, the conductive filler is displaced causing a more heterogeneous dispersion leading to a formation of more conductive pathways at lower GNP content.

The percolation threshold for the SoC films can be lowered further upon compression, as previously described, representative SoC films were compression molded above T_g and below melting and referred to as SoC-CM films. As seen in Figure 3.14, upon compression molding the 5 wt% SoC-CM film displays conductive behavior indicating that the percolation threshold is less than 5 wt%. The change in electrical

response after compression molding is attributed to the decrease in microvoids upon compaction. As described in section 3.3, there was some remnant chloroform present in both the 5 wt% SoC and 5 wt% SoC-CM films, but the amount of chloroform did not significant change. Furthermore, the degree of crystallinity and crystal phase was not altered upon compression. However, the spherulite size did increase slightly from 20.1 ± 1.0 nm to 24.0 ± 0.4 nm upon compression molding for the primary 16.7° diffraction peak, but the increase was minimal and it is concluded that this is not a dominating mechanism.

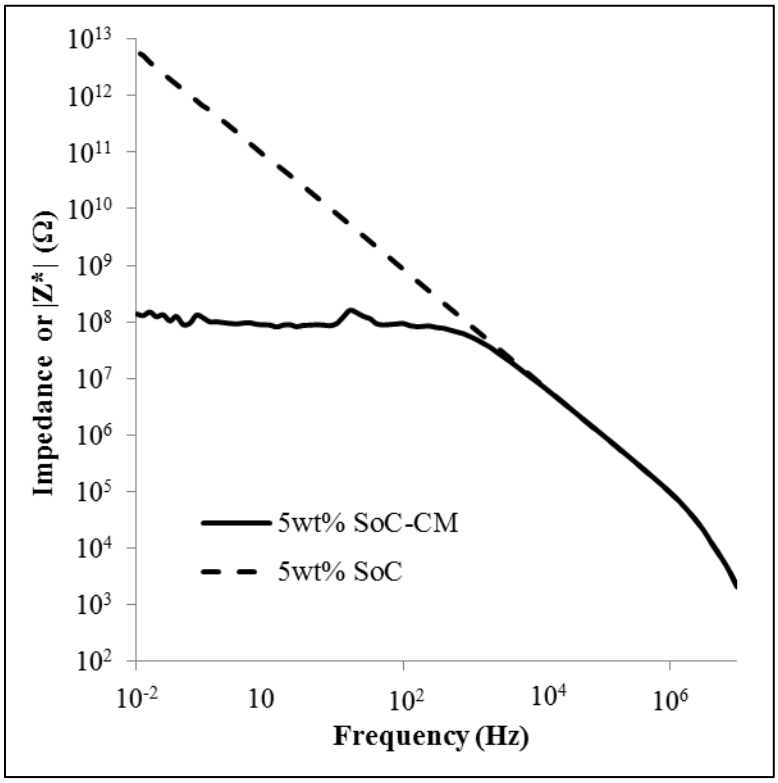

Figure 3.14 Representative impedance magnitude, |Z*|, as a function of frequency for 5 wt% SoC and 5 wt% SoC-CM films

3.5 Conclusions

The processing conditions and compounding methods employed to fabricate GNP/PLA composite films had a significant effect on both the mechanical and electrical response of these films. The processing conditions, i.e., slow versus fast cooling during compression molding, significantly altered the crystallization behavior of the polymer and strongly affected the dielectric behavior the GNP/PLA films. Furthermore, the highly amorphous FC films displayed a lower *E* compared to the highly crystalline SC films. On the other hand, the compounding method, i.e., melt compounding versus polymer dissolution, although it altered the dispersion and distribution of the GNP within the PLA matrix, it did not significantly affect the crystallization behavior of the polymer. The differences in percolation threshold and resistance between the FC and SC GNP/PLA films is attributed to the difference in PLA crystallinity with the FC films being amorphous with a more homogeneous GNP distribution and a percolation threshold between 12-15 wt% of GNP whereas the SC films exhibit a percolation threshold between 1-5 wt% of GNP and a more heterogeneous GNP distribution with smaller interparticle distances due to displacement of GNP during spherulite growth. Specifically, the main mechanisms for the observed results are the decreased scattering of electrons through the ordered crystalline lamella in SC films compared to the amorphous polymer phase in the FC films coupled with the excluded volume effect present in SC films.

The compounding method had a less significant effect on the electrical percolation. However, the difference in *E* between the SC and SoC films was significant. The SoC films exhibited similar crystallization characteristics to the SC films and had more homogeneous GNP distribution and dispersion due to the low viscosity of the

polymer solution during processing which led to a percolation threshold between 5 wt% and 8 wt% of GNP. The primary mechanism responsible for the lower percolation threshold and higher *E* of the SC films compared to that of SoC films is the difference in microstructure both in terms of micro-porosity and dispersion/distribution of GNP coupled with the exclude volume effect.

CHAPTER 4

EFFECT OF NANOFILLER GEOMETRY AND COMPOUNDING METHOD ON POLYLACTIC ACID NANOCOMPOSITE FILMS

This chapter focuses on understanding the effect of compounding method and nanofiller type on the nanofiller distribution and dispersion, crystallization behavior, thermo-mechanical behavior, and electrical response of PLA nanocomposite films. As outlined in Chapter 3, distribution and dispersion of nanofillers are governed by the compounding method [31, 46, 47]. In addition, the nanofiller type, both aspect ratio and chemistry, also influence the distribution, dispersion, and interfacial interactions between the nanofiller and polymer matrix. In Chapter 3, melt mixing, followed by melt fiber spinning and compression molding (MC-CM); and solution mixing, followed by solution casting (SoC) were used. In order to better isolate the effect of compounding on composite properties, this chapter employed: 1) MC-CM, and 2) solution mixing, followed by electrospinning and compression molding (E-CM). Both MC-CM and E-CM films are fabricated via compression molding of composite fibers with the only differences being the compounding of nanofiller and fabrication of fibers. For the MC-CM case, both GNP and CNT are used to determine the effect of nanofiller geometry on the film properties. When comparing the compounding method, CNT was chosen as the nanofiller. The cooling rate during compression molding is held constant in all cases at a slow cooling rate of ~0.4°C/min in order to maximize polymer matrix crystallinity as discussed in Chapter 3. It is also noted that due to the relatively high viscosity of the

CNT/polymer solution, the CNT content for the E-CM films was limited to 1 wt%. By comparing MC-CM and E-CM films rather than MC-CM and SoC films, the effect of compounding on film properties can be further identified.

Fabrication and characterization of CNT/PLA electrospun fibers has previously been explored [75-77]. Electrospun fiber diameter, morphology, and orientation have been shown to influence the electrical response of composite fibers and meshes [77, 78]. For example, Shao et al. [78] reported a percolation threshold of between 2-3 wt% of CNT for CNT/PLA electrospun meshes, with randomly oriented composite fiber meshes having a slightly lower surface resistivity compared to aligned composite fiber meshes. The novelty of this chapter is that it focuses on fabricating composite films from both electrospun and melt spun fibers in order to compare the percolation behavior of the resultant films, while simultaneously studying the effect of nanofiller geometry on electrical response. The GNP/PLA MC-CM, CNT/PLA MC-CM, and CNT/PLA E-CM composite films fracture surface morphology, crystallization behavior, thermo-mechanical properties, and electrical response were investigated as a function of nanofiller content.

4.1 Surface Composition of the Nanoreinforcements

The surface composition of GNP and CNT was compared using XPS in order to ascertain whether there was a significant difference in surface chemistry. Both the elemental composition of C and O in GNP and CNT, as well as the approximate concentration of specific chemical species for each nanofiller are shown in Table 4.1, while Figure 4.1 shows the high-resolution C 1s XPS scans of GNP and CNT. The high-

resolution C 1s scan for GNP was deconvoluted into six components with peak values of: 284.6 eV (C1) which corresponds to the sp^2-hybridized graphitic structure (C=C), 286.1 eV (C2) which corresponds to the sp^3-hybridized carbon atoms (C-C), and 287.5 eV (C3), 288.9 eV (C4), 290.4 eV (C5), and 291.7 eV (C6), which correspond to C-O, C=O, O-C=O, and π-π* transition loss peak, respectively [79]. Similarly, the high-resolution C 1s scan for CNT was deconvoluted into six components corresponding with same chemical species. For CNT, the peak values are: 284.6 eV (C1), 286.0 eV (C2), 287.1 eV (C3), 288.5 eV (C4), 290.0 eV (C5), and 291.4 eV (C6) [80]. During the intercalation and exfoliation steps used to fabricate GNP, a certain amount of oxidation can occur [81]. This accounts for the slightly higher oxygen content of the GNP. The presence of more C-O and C=O groups can lead to a better interface when the matrix polymer is polar [81]. Furthermore, the transformation of sp^2 carbons to sp^3 carbons also occurs in GNP due to oxidation and can lead to lower electrical conductivity [81], which is important to note when examining the films' electrical behavior.

Table 4.1 Relative atomic concentrations of components obtained from fittings of the high-resolution C 1s peak scan using XPS for GNP and CNT

	Composition (%)		**Concentration of chemical species (%)**					
	C	**O**	**-C=C**	**-C-C**	**-C-O**	**-C=O**	**C-OO**	**π-π***
GNP	95.1	4.9	65.1	12.0	6.6	5.1	3.1	8.1
CNT	99.0	1.0	75.0	6.4	4.5	3.1	1.7	9.3

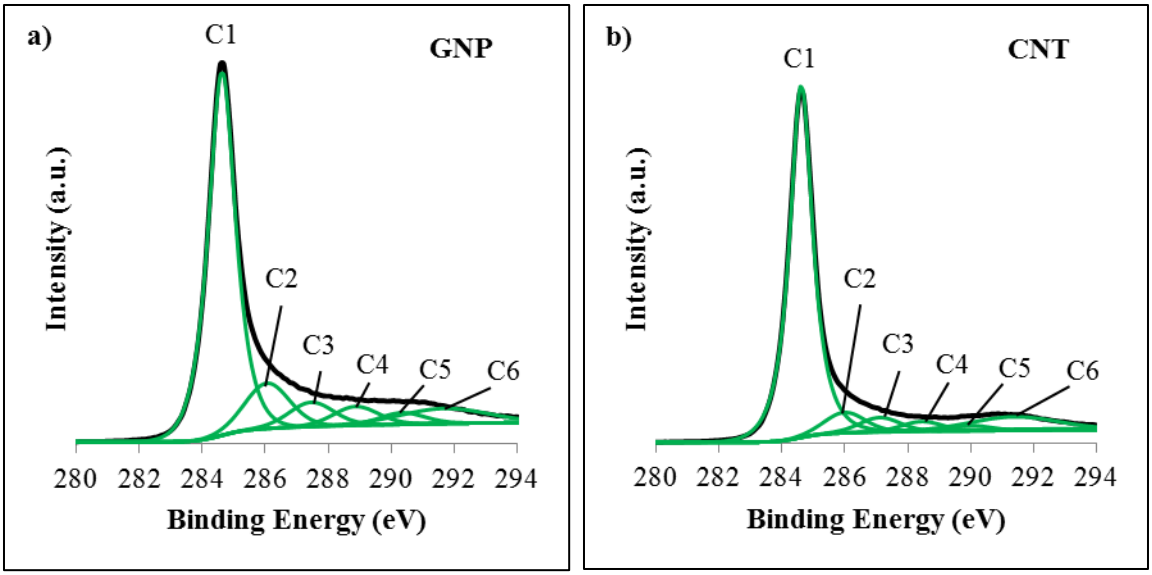

Figure 4.1 High resolution C 1s XPS scan of a) GNP and b) CNT

4.2 Morphology and Dispersion

Representative SEM images of the cryo-fracture surface of the 3 wt% GNP MC-CM film, 3 wt% CNT MC-CM film, and 1 wt% CNT E-CM film are shown in Figure 4.2a through f. The fine microstructure of the films can be seen in the low magnification images shown in Figure 4.2a, c, and e. Upon further magnification, seen in Figure 4.2d and f, the difference in distribution and dispersion of the nanofiller in the CNT MC-CM films compared to the CNT E-CM films is evident. As indicated by the arrows in Figure 4.2d, the CNT in the MC-CM film appears to be fairly homogeneously distributed throughout the matrix and there appear to be minimal agglomerates. However, the CNT in the E-CM film, seen in Figure 4.2f, have a much more heterogeneous distribution and dispersion with apparent agglomerates.

In order to further investigate the difference in CNT dispersion, the melt spun and electrospun CNT fibers were examined and representative SEM images of the fibers are seen in Figure 4.3a and b. The melt spun CNT/PLA composite fibers have a diameter on the order of 60-70 μm while the electrospun composite fibers have a diameter on the order of 0.5 μm. Furthermore, as seen in Figure 4.3b, the diameter of the electrospun fibers is not consistent. There are several agglomerates on the order of ~10-30 μm. The agglomerates seen in the electrospun fibers coupled with the heterogeneous dispersion of CNT in the films indicates CNT may be concentrated primarily in the agglomerates of the fibers leading to this heterogeneous dispersion. To further investigate the effect of nanofiller type and compounding method on the composite films, the crystallization behavior was investigated.

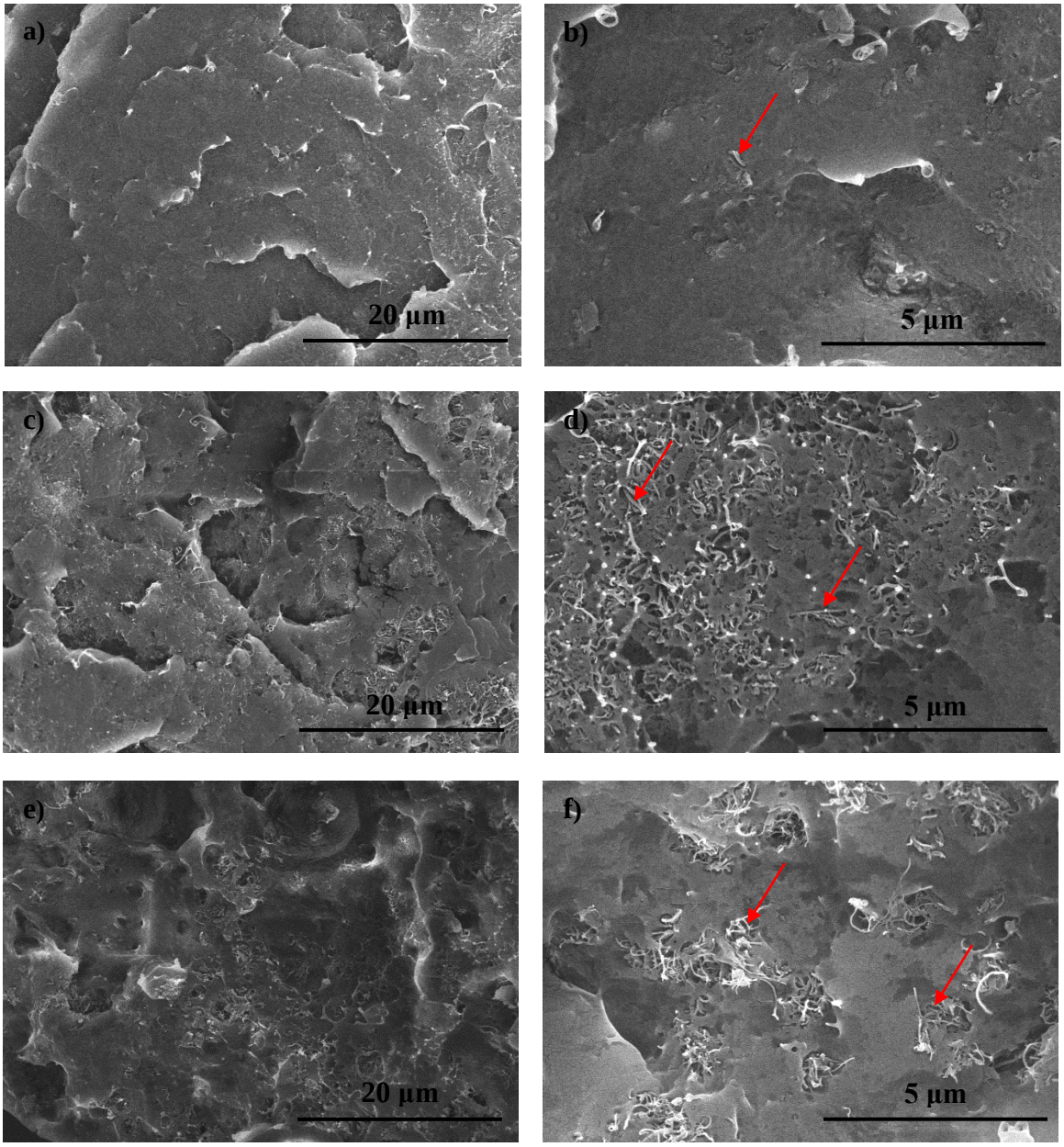

Figure 4.2 Representative cross sectional SEM images of composite film cryo-fracture surfaces: a) 3 wt% GNP MC-CM at low magnification, b) 3 wt% GNP MC-CM at high magnification, c) 3 wt% CNT MC-CM at low magnification, d) 3 wt% CNT MC-CM at high magnification, e) 1 wt% CNT E-CM at low magnification, and f) 1 wt% CNT E-CM at high magnification. Arrows indicate nanofiller.

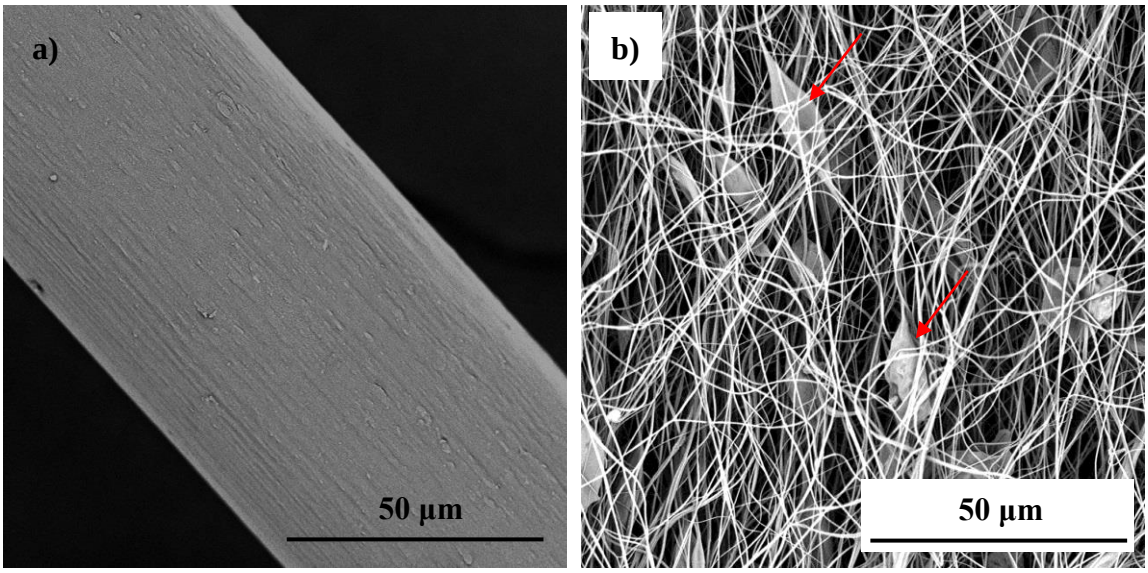

Figure 4.3 Representative SEM images of 1 wt% CNT fibers fabricated via a) melt spinning and b) electrospinning. Arrows indicate agglomerates.

4.3 Crystallization Characterization of Composite Films

The crystallization behavior of the films was first examined using initial heating thermograms, seen in Figure 4.4. The glass transition temperature (T_g) and degree of crystallinity, calculated using equation (3.1), are displayed in Table 4.2. There is no statistically significant change in T_g or degree of crystallinity as a function of either nanofiller content, type, or compounding method. The T_g of the films is ~60°C and the films are highly crystalline with a degree of crystallinity of ~36%. As observed in Chapter 3, the degree of crystallinity is affected more by the cooling rate during compression molding rather than the nanofiller content or compounding method. Because all three sets of films were fabricated using the same cooling rate during compression molding, the degree of crystallinity is not significantly altered. Furthermore, the

nanofiller type does not seem to significantly affect either the T_g or the degree of crystallinity, as seen in Figure 4.4 and Table 4.2. It is concluded that the nanofiller type does not play a significant role in altering the degree of crystallinity of the films and this characteristic is dominated by the processing conditions rather than nanofiller type, compounding method, or nanofiller content. The films also displayed double melting behavior, which as described in Chapter 3, is indicative of either polymorphism or melt recrystallization. To confirm the mechanism behind the double melting endotherms, diffraction patterns of the films were examined to determine crystal structure of the films.

Table 4.2 Effect of compounding method and nanofiller geometry on the degree of crystallinity (χ) and glass transition temperature (T_g) for GNP MC-CM, CNT MC-CM, and CNT E-CM PLA nanocomposite films

	χ (%)			T_g (°C)		
	GNP MC-CM	**CNT MC-CM**	**CNT E-CM**	**GNP MC-CM**	**CNT MC-CM**	**CNT E-CM**
0 wt%	36.9±1.3	35.7±0.8	31.2±2.7	60.8±0.1	61.2±0.2	59.5±0.5
1 wt%	35.7±0.8	37.9±0.8	36.7±0.5	58.0±0.4	60.5±0.3	60.1±0.2
2 wt%	36.6±0.9	37.8±0.7	-	61.2±3	60.0±0.3	-
3 wt%	35.3±3.2	35.5±1.0	-	61.3±0.1	60.6±0.2	-

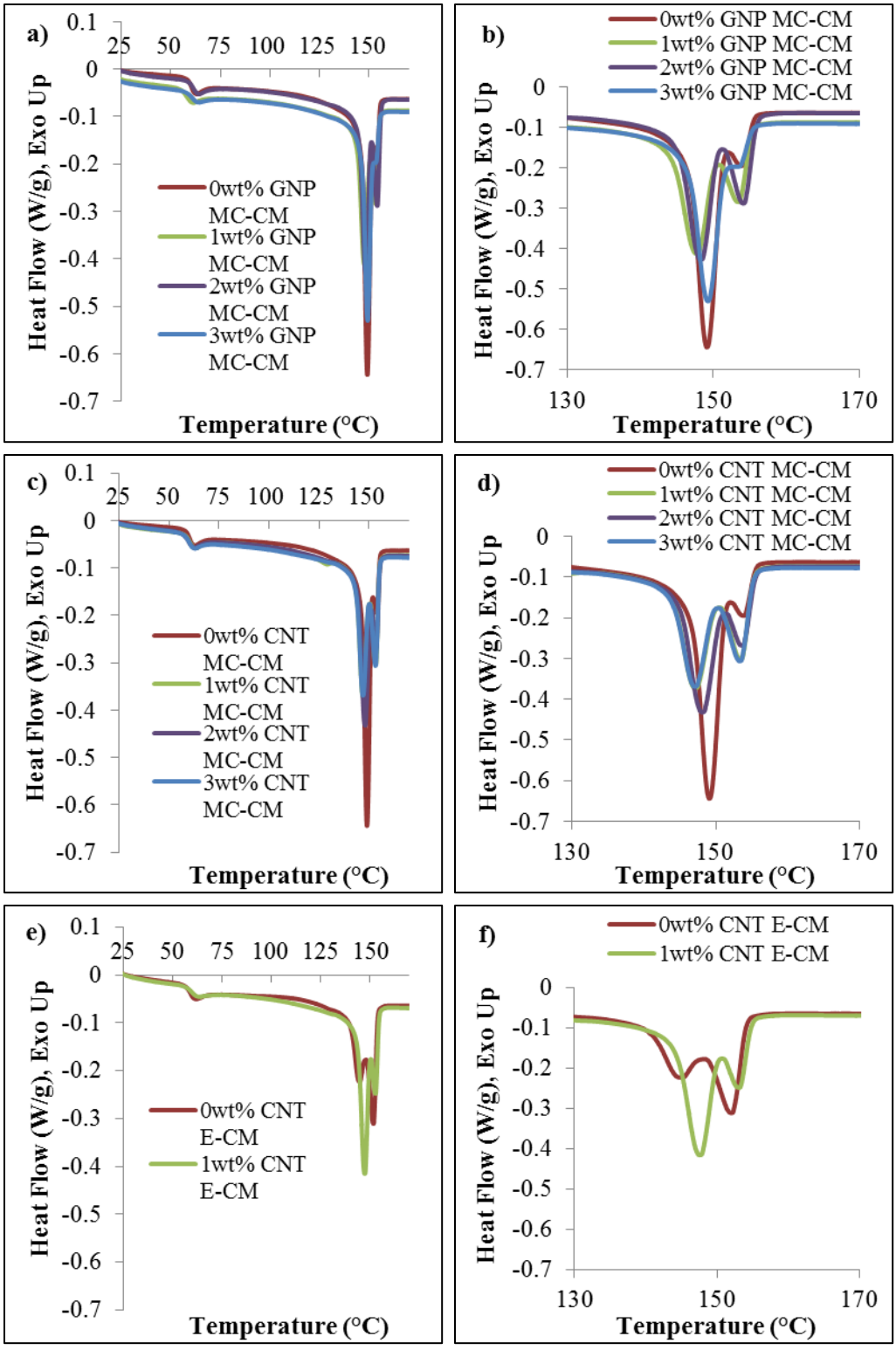

Figure 4.4 Non-isothermal initial heating thermograms of a) GNP MC-CM, b) GNP MC-CM melting endotherm, c) CNT MC-CM, d) CNT MC-CM melting endotherm, e) CNT E-CM, and f) CNT E-CM melting endotherm

As outlined in Chapter 3, PLA has three primary polymorphs, α, β, and γ, and a secondary polymorph, α'. As seen in Figure 4.5, the diffraction patterns for the GNP MC-CM, CNT MC-CM, and CNT E-CM films all show only the primary α crystal phase, indicating that the double melting endotherms observed in Figure 4.4 are a result of melt recrystallization and not polymorphism. As seen in Figure 4.5, the highly crystalline PLA is dominating the behavior and the primary diffraction peaks associated with both GNP and CNT at approximately 26.6° are not apparent. The sharp diffraction peaks associated with the PLA's primary α crystal phase indicate a highly crystalline structure which is in good agreement with the degree of crystallinity calculated using equation (3.1) and presented in Table 4.2. The GNP MC-CM, CNT MC-CM, and CNT E-CM films all display characteristic peaks of crystalline PLA at 2θ = 15.0°, 16.7°, 19.1°, and 22.4°, which correspond to the characteristic planes of α(010) [64], α(200 + 110) [62], α(203) [64], and α(121) [64]. While the degree of crystallinity and crystal structure is almost identical for the three sets of films, these are just two aspects of the crystallization behavior. The average lamella thickness may vary despite a comparable degree of crystallinity and crystal structure.

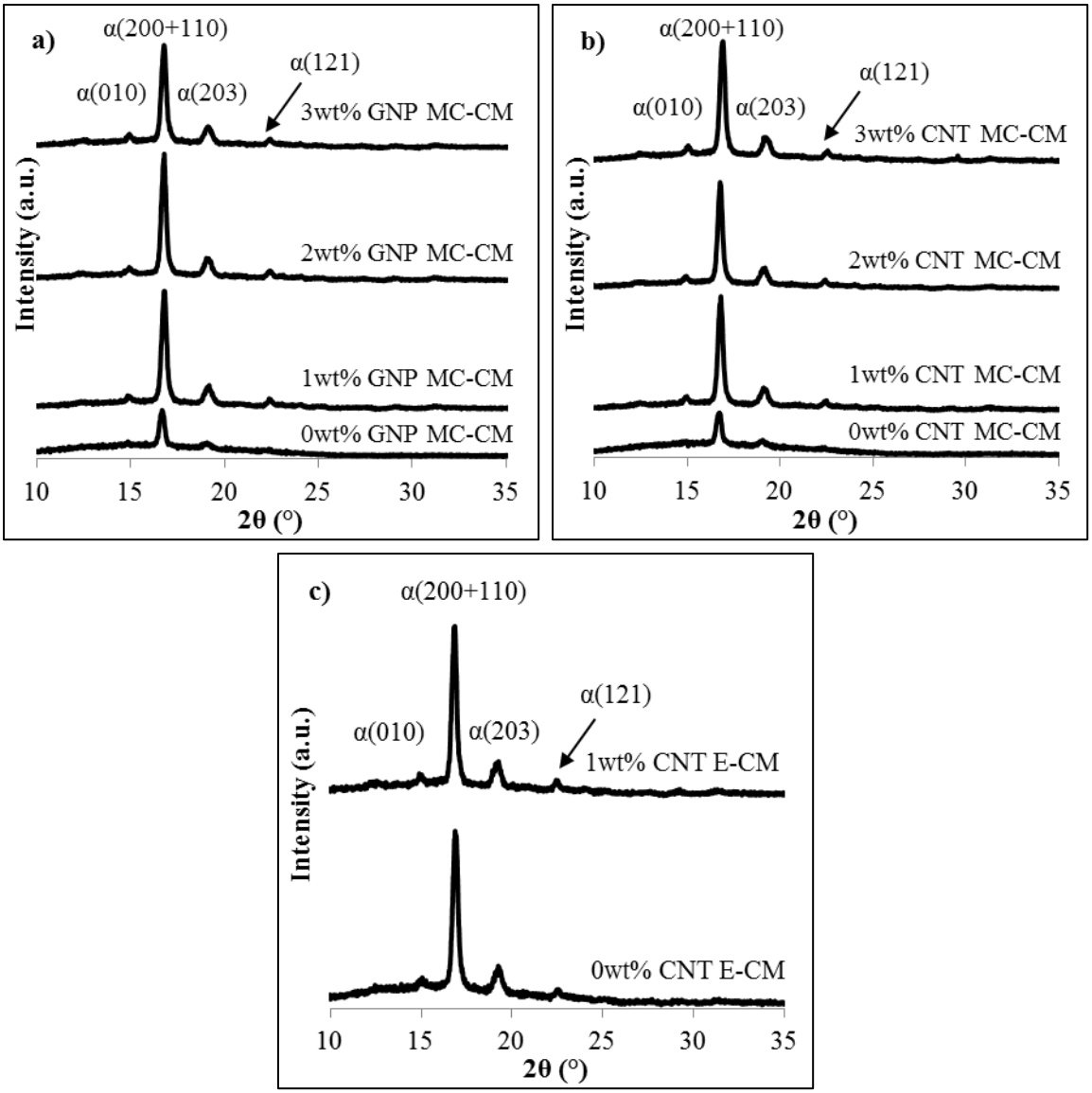

Figure 4.5 Diffraction patterns obtained for the a) GNP MC-CM, b) CNT MC-CM, and b) CNT E-CM films as a function of nanofiller content

The average lamella thickness for the two primary PLA crystal diffraction peaks at 16.7° and 19.1° is calculated using equation (3.2), the Scherrer equation, outlined in Chapter 3. As seen in Figure 4.6, the average lamella thickness does not significantly change as a function of both filler type or compounding method. Furthermore, the lamella

thickness for all three films, GNP MC-CM, CNT MC-CM, and CNT E-CM, does not change significantly with increased nanofiller content. This indicates that both the degree of crystallinity as outlined in Figure 4.4 and Table 4.2 and the lamella thickness seen in Figure 4.6 remains constant with the addition of nanofiller. It is concluded that neither the compounding method nor the nanofiller type significantly affects the crystallization behavior of the composite films.

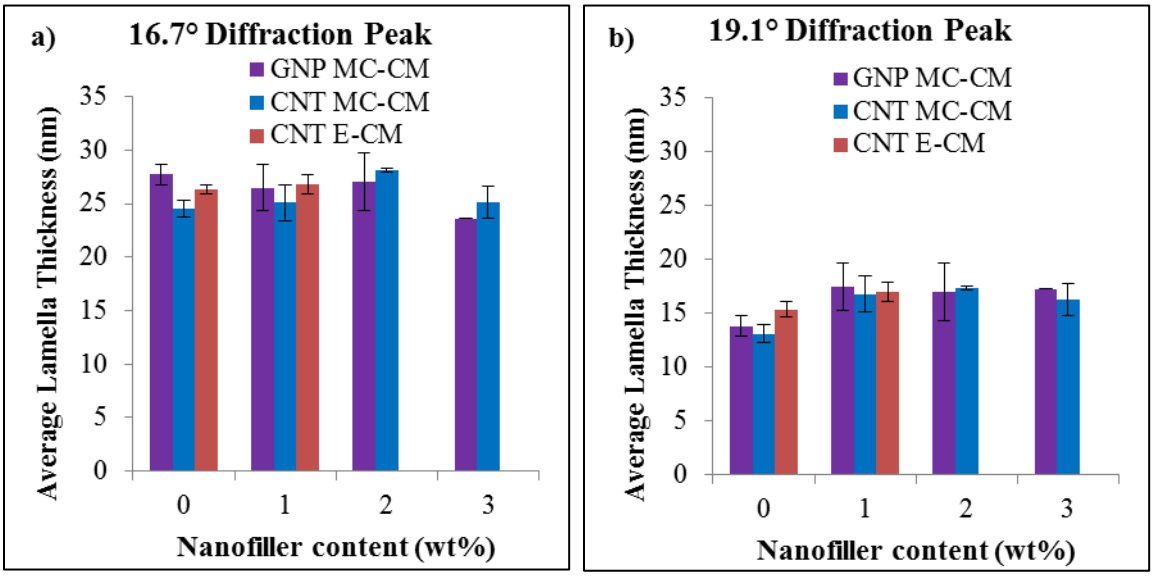

Figure 4.6 Average crystal lamella thickness of the two dominant diffraction peaks, a) 16.7° and b) 19.1°, for the GNP MC-CM, CNT MC-CM, and CNT E-CM films as a function of nanofiller content

4.4 Effect of Filler Type and Compounding Method on Thermo-mechanical Properties

The thermo-mechanical behavior of the films, both the storage modulus (E') and loss modulus (E''), is investigated as a function of nanofiller content. The results are seen in both Table 4.3 and Figure 4.7. The storage modulus slightly increases with the addition of nanofiller for all three sets of films. An increase in storage modulus is indicative of hindered polymer chain mobility, which can be attributed to: 1) an increase in polymer crystallinity which leads to lower chain mobility [67], 2) the addition of nanofiller which can disrupt the movement of polymer chains [66, 82, 83], or 3) a combinatory effect of 1) and 2).

The crystallization behavior of the films outlined in the previous section indicated no significant change in degree of crystallinity for any of the films; therefore, it can be assumed that the increase in storage modulus is due to the addition of nanofiller, which can hinder polymer chain mobility and increase storage modulus. However, there is only a slight increase in storage modulus with the addition of GNP and a more significant increase with the addition of CNT for both the MC-CM and E-CM films. As seen in Table 4.3, the storage modulus is increased to ~ 3 GPa with the addition of 1 wt% CNT for the CNT MC-CM and CNT E-CM films. While intrinsic properties, such as the modulus, of GNP and CNT are often very similar, factors such as differences in polymer-nanofiller interface and aspect ratio can lead to differences in performance. Despite a much more significant initial increase in storage modulus for the CNT films, the behavior seems to plateau and the storage modulus for the 3 wt% GNP MC-CM and 3 wt% CNT MC-CM films is comparable.

Furthermore, as seen in Figure 4.7b, there is a slight broadening of the loss modulus peak indicating a lengthening of the glass transition region. This broadening can also be attributed to some degree of hindered polymer chain mobility which is due to the addition of nanofiller, constricting polymer chain movement [82, 83]. However, it is important to note that the T_g does not increase, as would be anticipated despite the fact that the glass transition region is broadening with the addition of nanofiller. The broadening may also be attributed to the additional energy dissipation that is introduced to the material by adding GNP or CNT, such as interfacial friction between GNP or CNT and PLA [84].

Table 4.3 Storage modulus of the GNP MC-CM, CNT MC-CM, and CNT E-CM films as a function of nanofiller content

	E′ at 35°C (GPa)		
	GNP MC-CM	**CNT MC-CM**	**CNT E-CM**
0 wt%	2.0 ± 0.3	1.9 ± 0.2	2.2 ± 0.1
1 wt%	2.5 ± 0.3	3.0 ± 0.3	3.0 ± 0.2
2 wt%	2.5 ± 0.1	3.3 ± 0.1	-
3 wt%	3.3 ± 0.2	3.3 ± 0.3	-

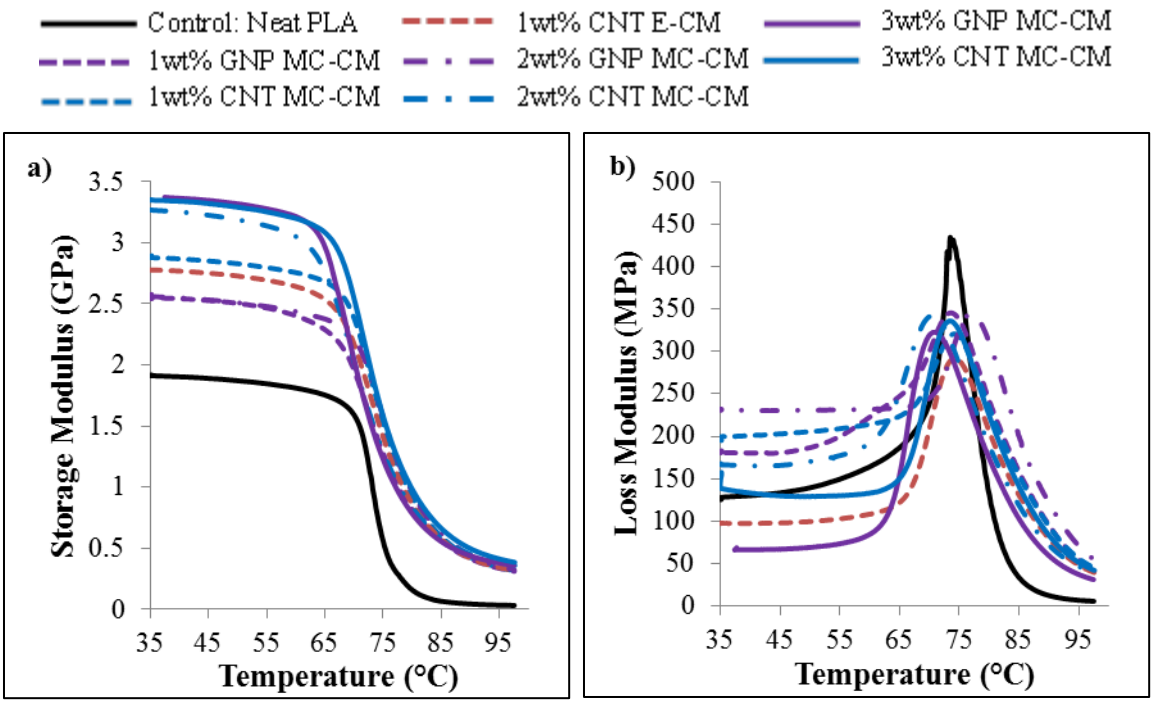

Figure 4.7 Representative a) storage modulus and b) loss modulus of the GNP MC-CM, CNT MC-CM, and CNT E-CM films as a function of nanofiller content

4.5 Effect of Filler Type and Compounding Method on the Electrical Response

The in-plane (x-y plane) electrical response of the films is examined using impedance spectroscopy. As outlined in Chapter 3 and equations (3.3) – (3.5), impedance spectroscopy measures change in current, voltage, and phase angle over a wide range of frequencies [44]. The impedance magnitude ($|Z^*|$) reported as a function of frequency for all three sets of films is shown in Figure 4.8. The loss of frequency dependence and drop in the low frequency impedance indicates conductive behavior and electrical percolation [72, 73].

As seen in Figure 4.8a, the GNP MC-CM films did not show conductive behavior even at 3 wt%. In Chapter 3, the percolation threshold of slow cooled (SC) GNP/PLA composite films fabricated via MC-CM was found to be between 1 wt% and 5 wt% GNP. It can now be concluded that percolation occurs between 3 wt% and 5 wt% GNP. Even though the low frequency $|Z^*|$ is relatively high (on the order of 10^{10} Ω) the CNT MC-CM films are conductive even at 1 wt% CNT, indicating the percolation threshold is less than 1 wt%. Upon further addition of CNT, the low frequency $|Z^*|$ decreases indicating an increases in conductance. However, it is important to note that due to the inherent heterogeneous structure of composites, this trend is not always seen particularly when close to the percolation threshold. The CNT E-CM films also have a percolation threshold of less than 1 wt% of CNT; however, at 1 wt% the low frequency $|Z^*|$ is lower than the low frequency $|Z^*|$ of the 1 wt% CNT MC-CM film. This indicates higher conductance at identical CNT content.

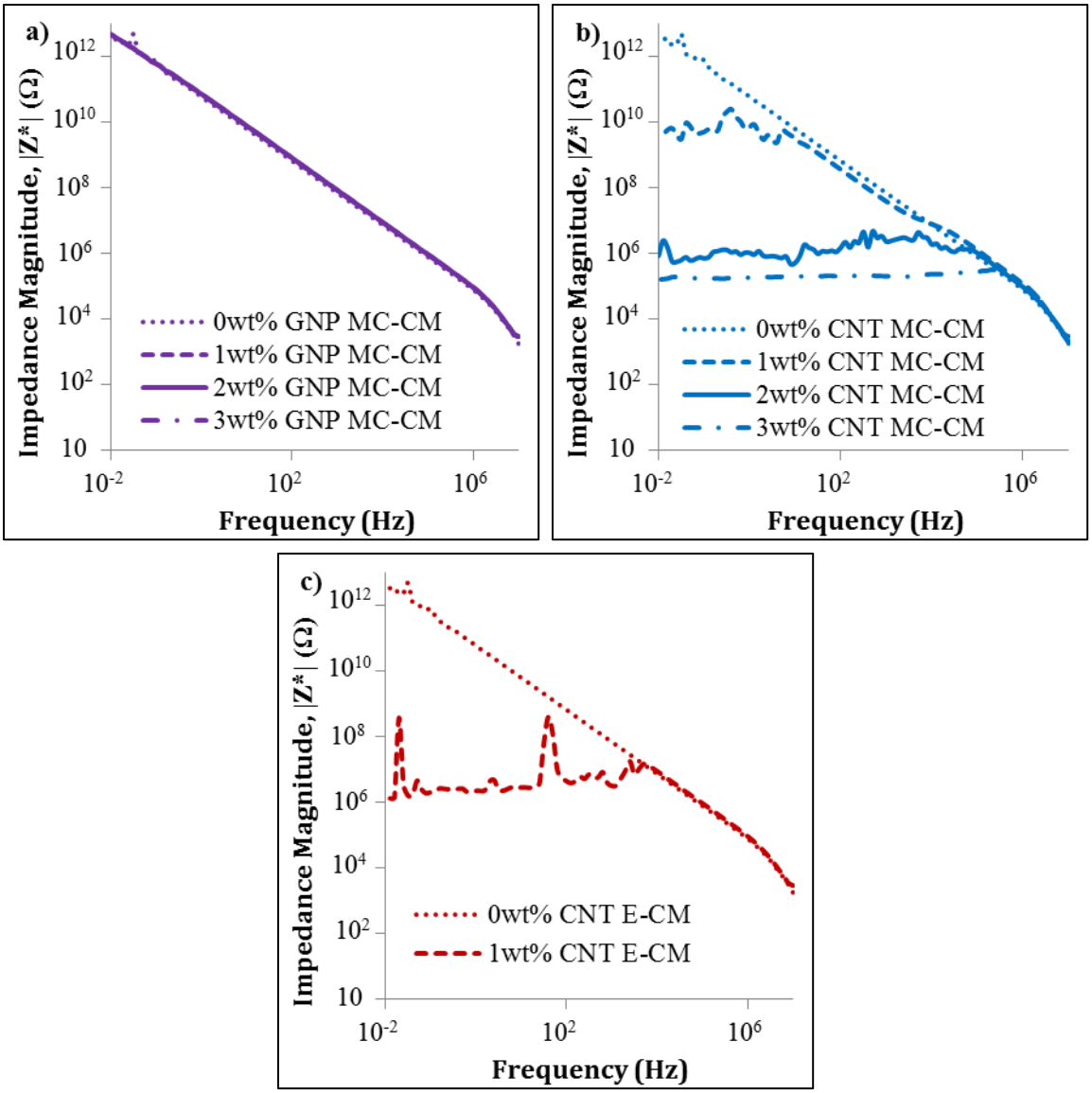

Figure 4.8 Representative runs of impedance magnitude, |*Z|, as a function of frequency for a) GNP MC-CM, b) CNT MC-CM, and c) CNT E-CM films**

The potential primary mechanisms for the difference in percolation threshold between the GNP MC-CM and CNT MC-CM films are: 1) the difference in surface composition and 2) the difference in geometry between GNP and CNT. As discussed in section 4.1, the surface composition of the GNP and CNT varies slightly. The GNP has a slightly higher oxygen content compared to the CNT, which has been reported to lower

the electrical conductivity of GNP [81]. While the intrinsic electrical conductivity of the GNP may be slightly lower than the reported in-plane conductivity value of ~10^7 S/m, displayed in Table 2.2, based on the analysis of the GNP/PLA composite films in Chapter 3, the GNP are still conductive. Furthermore, the intrinsic electrical conductivity of the CNT as reported by the manufacturer is >10^4 S/m [42], so it is concluded that this is not a dominating mechanism for the difference in percolation. Another contributing mechanism for the difference in percolation threshold is the significant difference in geometry between the GNP and CNT, particularly the aspect ratio. Aspect ratio, α, is defined as the ratio of length to diameter of a reinforcement. A filler with a high aspect ratio facilitates percolation through network formation at lower filler concentrations compared to a filler with a low aspect ratio [85]. The reported theoretical α for the GNP used is ~150, while for the CNT α is reported to be ~375. For comparison, a bulk composite with randomly distributed spherical inclusions of equal diameter (α = 1) has a critical percolation volume fraction of 0.2895 or 28.95 vol.% of filler [86, 87].

A schematic of the two films is displayed in Figure 4.9 and the importance in aspect ratio to achieve percolation it is illustrated. As seen in Figure 4.9a, there should be some amount of orientational ordering in the in-plane (x-y plane) direction due to application of compressive force in the z-direction during processing. At identical nanofiller content, the CNT will form a percolated network easier than the GNP due to the higher α, seen in Figure 4.9b. It is important to note however, that the theoretical aspect ratio of ~150 and ~375 for the GNP and CNT, respectively, may not be the effective α due to agglomerations and high shear forces during processing [88]. The

change in aspect ratio of the nanofillers and its effect on composite film properties are further explored in Chapter 5.

Finally, the in-plane electrical response is reported and because the GNP and CNT have very different geometries this could be a factor in the difference in percolation. The GNP are two dimensional platelet-like reinforcements with a through-plane conductivity reported at ~10^2 S/m [41], while the CNT are essentially one-dimensional tube-like reinforcements which are ideal for achieving low in-plane percolation thresholds when in-plane orientational ordering is achieved, shown in Figure 4.9. However, if a high through-plane conductivity is desired, the two-dimensional GNP may be a more desirable reinforcement.

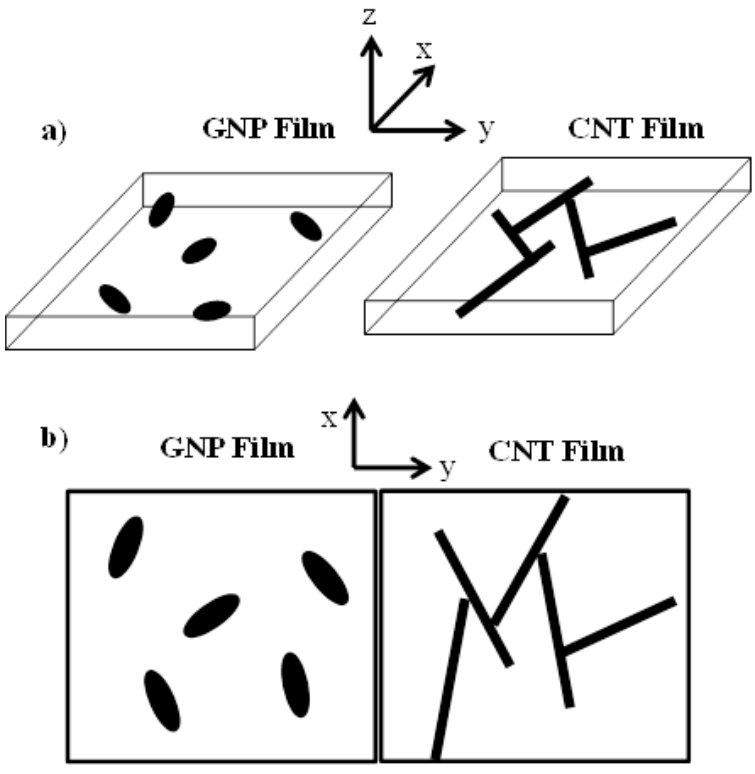

Figure 4.9 Schematic of a) the side view and b) the top view of the GNP and CNT films. Note the schematic is not to scale.

The compounding method has significantly less of an effect on the electrical response than the nanofiller type. Both the CNT MC-CM and CNT E-CM films displayed conductive behavior at 1 wt%, indicating both have a percolation threshold less than 1 wt% of CNT. However, the 1 wt% CNT E-CM film had a much lower low frequency $|Z^*|$ compared to the 1 wt% CNT MC-CM film indicating higher conductance. The potential primary mechanisms for the difference in percolation threshold between the CNT MC-CM and CNT E-CM films are: 1) the differences in dispersion of the CNT and 2) potential remnant solvent in the E-CM film. The nanofiller dispersion and distribution plays a critical role in the electrical response of the composite. When a nanofiller is homogeneously dispersed throughout the matrix, more filler content is generally needed to achieve an interconnected network and good percolation [85].

For a low percolation threshold, it is generally desirable to have a heterogeneously dispersed network of conductive nanofiller. As shown in Figure 4.2d and f, the dispersion of CNT varies for the MC-CM film and E-CM film. The CNT is more heterogeneously dispersed in the E-CM film compared to the MC-CM film. This heterogeneous dispersion may lead to a more interconnected network and contribute to the higher conductance of the E-CM film at 1 wt% of CNT.

Because of the sensitivity of electrical measurements, any remnant solvent in the E-CM films may alter the electrical response. TGA was performed on the E-CM films in order to determine whether there was remnant solvent and a representative TGA of the 1 wt% CNT E-CM film is shown in Figure 4.10. It is apparent that there is no remnant solvent in the E-CM films and therefore it was concluded that this is not a dominating factor for the difference in electrical response between the CNT MC-CM and E-CM

films. The primary mechanism for the difference in electrical response is concluded to be the difference in dispersion of the CNT.

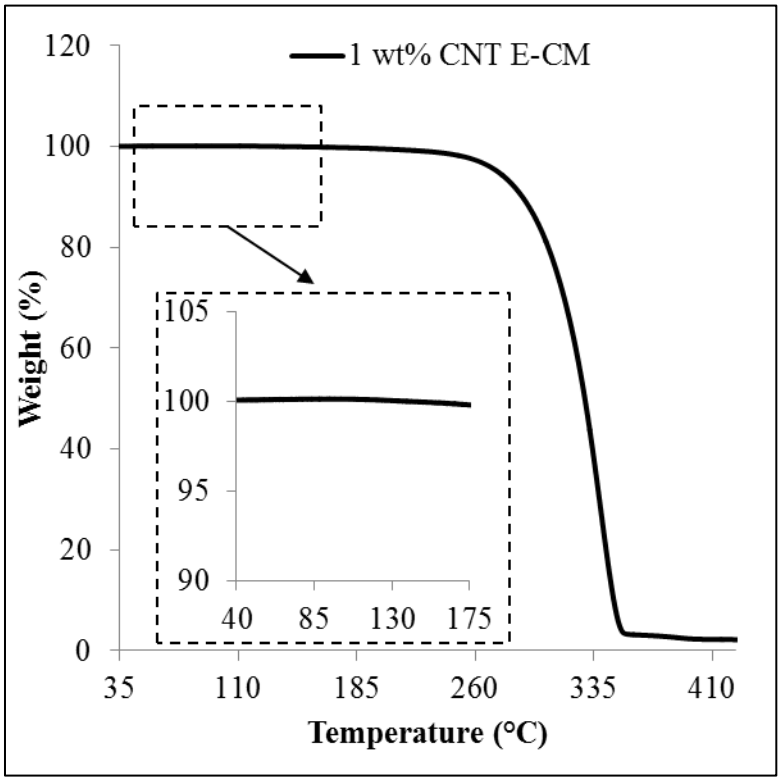

Figure 4.10 Representative TGA of the 1 wt% CNT E-CM film

4.6 Conclusions

While the nanofiller type and compounding methods employed to fabricate the composite films did not have a significant effect on the crystallization behavior of the films, the microstructure, as well as the thermo-mechanical and electrical response of the films was significantly altered. The melt spun fibers had a significantly larger diameter compared to the electrospun fibers. Furthermore, the electrospun fiber diameter was not

constant. The heterogeneous dispersion of CNT in the E-CM films may be attributed to the significant agglomerates seen in the electrospun fibers. Upon addition of nanofiller, both GNP and CNT, the storage modulus significantly increased indicating the constriction of polymer chain mobility due to the presence of nanofiller.

The difference in low frequency $|Z^*|$ between the GNP MC-CM and CNT MC-CM films is attributed to the difference in surface composition and geometry of the GNP and CNT and a percolation threshold greater than 3 wt% is reported for the GNP MC-CM film, while a percolation threshold lower than 1 wt% is reported for the CNT MC-CM film. The compounding method had a less significant effect on the electrical response. Both the CNT MC-CM and CNT E-CM films percolated at CNT content less than 1 wt%; however, the 1 wt% E-CM film displayed a lower low frequency $|Z^*|$ compared to the 1 wt% MC-CM film, indicating a higher conductance. The primary mechanism responsible for the lower low frequency $|Z^*|$ of the CNT E-CM film, is the more heterogeneous dispersion of CNT throughout the matrix, facilitating an interconnected nanofiller network.

CHAPTER 5

EVALUATING THE INFLUENCE OF NANOFILLER CHARACTERISTICS AND PROCESSING CONDITIONS ON THE ELASTIC MODULUS OF NANOCOMPOSITE FILMS

This chapter focuses on investigating the influence of specific parameters, such as nanofiller aspect ratio, processing conditions, and nanofiller type and content, on the elastic modulus of the composite films. Micromechanical modeling was used to help identify the effect of aspect ratio on the elastic modulus of the PLA composite films. The GNP MC-CM slow cooled films were used as the case study and experimental data was fit to four well-known micromechanical models for composites: 1) Halpin-Tsai (HT) unidirectional [89], 2) Halpin-Tsai (HT) randomly oriented [90], 3) Tandon-Weng (TW) unidirectional [91], and 4) Tandon-Weng (TW) randomly oriented [92]. The constants, assumptions, and limitations of the four micromechanical models are discussed. Furthermore, in order to examine the effect of multiple factors on the composite film elastic modulus, a design of experiments was performed. Specifically, a 2^3 factorial design was used and the following three factors were considered: 1) nanofiller type, GNP versus CNT, 2) nanofiller content, and 3) processing conditions, fast cooling (FC) versus slow cooling (SC).

5.1 Elastic Modulus: Micromechanical Models vs. Experimental Results

5.1.1 Theoretical Models and Assumptions

The experimental data for the elastic modulus is compared to four well-known theoretical micromechanical models to gain a better understanding of the effect of filler aspect ratio on the elastic modulus of the composite. Both the Halpin-Tsai (HT) model for the approximation of the longitudinal tensile modulus (E_{11}) in a unidirectional, fiber-reinforced composite, referred to as HT U, and the HT model for E_{11} in a randomly oriented, discontinuously fiber-reinforced composite, referred to as HT R, are considered. The equations describing the E_{11} for the unidirectional and randomly oriented cases are outlined below in equations (5.1) and (5.2), respectively [89, 90]:

$$E_{11} = E_0 \frac{1 + \eta \xi c}{1 - \eta c} \tag{5.1}$$

$$E_{11} = \left[\frac{3}{8} \left(\frac{1 + \frac{2}{3}(\alpha \eta_L c)}{1 - \eta_L c} \right) + \frac{5}{8} \left(\frac{1 + 2\eta_T c}{1 - \eta_T c} \right) \right] E_0 \tag{5.2}$$

where E_0 is the modulus of the matrix material, ξ is a function of the filler material's aspect ratio, α, and for platelet shaped fillers, $\xi = 2/3\alpha$, and c is the filler volume percent. For platelet shaped fillers, $\eta_L = \eta$ and η and η_T are outlined in equations (5.3) and (5.4) below:

$$\eta = \frac{\frac{E_1}{E_0} - 1}{\frac{E_1}{E_0} + \xi} \tag{5.3}$$

$$\eta_T = \frac{\frac{E_1}{E_0} - 1}{\frac{E_1}{E_0} + 2} \tag{5.4}$$

Furthermore, the Tandon-Weng (TW) models for the approximation of E_{11} for both the unidirectional (TW U) and randomly oriented, discontinuous (TW R) composite cases are also considered. The equations describing the E_{11} for the unidirectional and randomly oriented cases are outlined below in equations (5.5) and (5.6), respectively [91, 92]:

$$E_{11} = E_0 \frac{1}{1 + c\,(A_1 + 2\nu_0 A_2)/A} \tag{5.5}$$

$$E_{11} = E_0 \frac{1}{1 + cp_{11}} \tag{5.6}$$

where A_1, A_2, A, and p_{11} are functions of the nanofiller aspect ratio and are further described in Appendix A and ν_0 is the Poisson's ratio of the matrix.

Several assumptions were made for the four theoretical micromechanical models. Table 5.1 outlines the constants and assumptions used for all of the models. The experimental elastic modulus of PLA was used to account for the influence of specific processing conditions on the films. GNP often is reported to have an elastic modulus of up to 1 TPa, however, this value is based on monolayer graphene [93], which will have a higher modulus than the GNP used in this study. The elastic modulus of GNP was assumed to be 70 GPa [94, 95] based on previous research. The experimental data and the predictions of the four models for the elastic modulus of the GNP MC-CM composite film are shown in Figure 5.1. The theoretical value of 150 [41] was used as the aspect ratio. Included in Figure 5.1 are the predictions for the longitudinal and transverse modulus of a unidirectional continuous fiber reinforced composite, representing the upper and lower bounds of the behavior. The longitudinal and transverse moduli are outlined in equations (5.7) and (5.8), respectively.

$$E_{11} = cE_1 + (1 - c)E_0 \tag{5.7}$$

$$E_{22} = \frac{E_1 E_0}{E_1 - c(E_1 - E_0)} \tag{5.8}$$

where E_{11} and E_{22} are the longitudinal and transverse moduli, respectively, E_0 and E_1 are the modulus of the matrix and filler, respectively, and c is the filler volume fraction.

Table 5.1 Assumptions and constants used in the micromechanical models

Property	Value	Determination Method / Reference
GNP thickness, *t* (nm)	10	[41]
GNP diameter/length (μm)	1.5	[41]
Poisson's ratio, PLA	0.36	[6]
Poisson's ratio, GNP	0.25	[96]
Elastic modulus of PLA (GPa)	3.179	Tensile test
Elastic modulus of GNP (GPa)	70	AFM [94, 95]
Density of PLA (g/cm^3)	1.9	[46]
Density of GNP (g/cm^3)	1.25	[46]

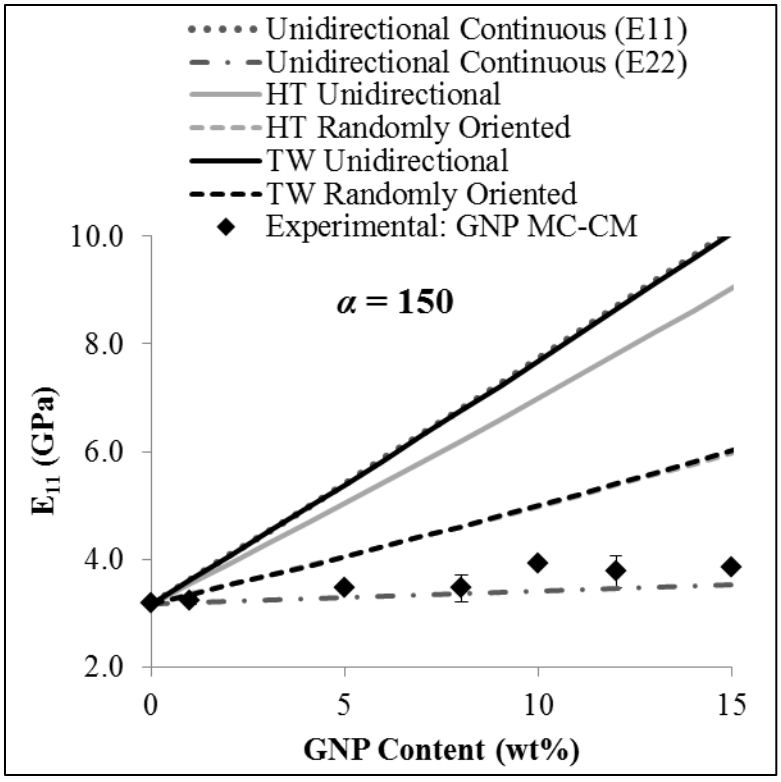

Figure 5.1 Elastic modulus for GNP MC-CM films with GNP aspect ratio of 150

The largest limitation of the micromechanical models is that they assume: 1) perfect contact between the nanofiller and polymer, 2) a specific orientation of the nanofiller throughout the matrix (i.e. unidirectional or randomly aligned), and 3) homogeneous distribution and dispersion or no agglomerations [90-92, 95].

There are several differences in the morphology/structure of what is assumed in the theoretical models and that of the composites made, a schematic representation is shown in Figure 5.2. First, the samples do not have a completely homogeneous distribution or dispersion of GNP. While there should be some degree of orientational ordering in the plane of the films (x-y plane), due to the applied pressure during compression molding there should be no positional ordering. The modulus of ~70 GPa

used for the GNP in the model is the longitudinal modulus and therefore there will be some discrepancy in the modulus if the GNP are not completely aligned in the plane of the film (x-y plane). Furthermore, the existence of agglomerations will alter the perceived aspect ratio of the model by increasing the apparent or effective thickness of the GNP (*t**), as seen in Figure 5.2. The micromechanical models used also assume a perfect contact at the nanofiller/polymer interface. In reality, the interface region should most likely be treated as an additional phase in the micromechanical models. Furthermore, any micro-voids or porosity that result in decrease of the elastic modulus are not taken into consideration in the models.

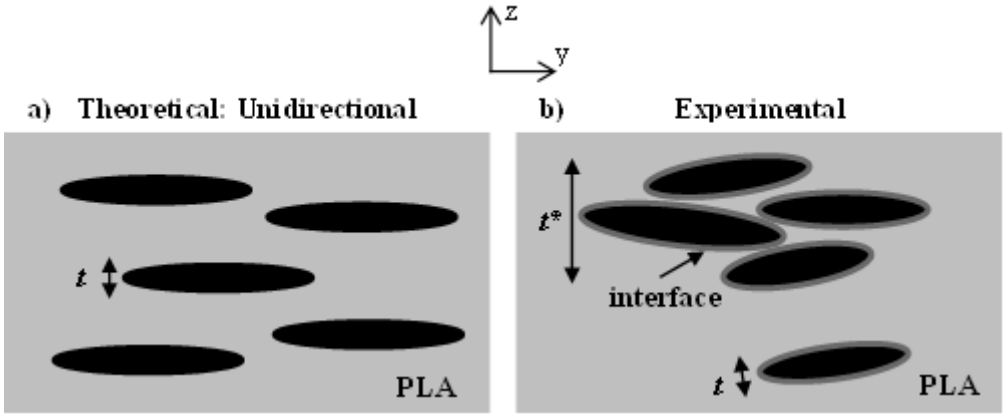

Figure 5.2 Schematic of the side view of the a) unidirectional theoretical and b) experimental GNP/PLA film

5.1.2 Effect of Aspect Ratio

In order to understand the effect of the aspect ratio on the modulus of the composites, which means the importance of the homogeneous dispersion assumption, the following parametric study was conducted. GNP agglomerates alter t^* thereby altering α which is an input parameter in the models. The diameter of the GNP was assumed constant at 1.5 μm. Perfect contact between GNP was also assumed. Assuming a very small agglomerate, i.e. consisting of only three graphite platelets, shown schematically in Figure 5.3, the corresponding values for the effective thickness and aspect ratio are ~30 nm and ~50, respectively. As seen in Table 5.2, the modulus values predicted by all four models are significantly reduced for the case of the small agglomerates. However, the models still over predict the modulus. Each model was then optimized to fit the experimental data and the predictions are shown in Table 5.2.

Figure 5.3 Schematic of GNP agglomerate with assumed perfect contact between GNP

Table 5.2 Effect of aspect ratio on elastic modulus

wt%	Exp. Data (GPa)	HT R	HT U	TW R	TW U	HT R	HT U	TW R	TW U
		t=30 nm, α=50*				*α=1.00*	*α=2.08*	*α=1.46*	*α=1.50*
0	3.179 ±0.054	3.179	3.179	3.179	3.179	3.179	3.179	3.179	3.179
1	3.231 ±0.065	3.316	3.453	3.340	3.591	3.226	3.224	3.226	3.238
5	3.463 ±0.045	3.886	4.584	4.010	5.270	3.422	3.414	3.422	3.485
8	3.459 ±0.248	4.334	5.469	4.540	6.565	3.580	3.567	3.576	3.682
10	3.910 ±0.013	4.644	6.077	4.909	7.445	3.691	3.674	3.684	3.818
12	3.767 ±0.300	4.963	6.701	5.289	8.340	3.806	3.785	3.794	3.960
15	3.854 ±0.033	5.459	7.668	5.884	9.710	3.988	3.961	3.968	4.181

**Note that all units are in GPa*

Upper and lower bounds for α were determined by fitting the experimental data to the unidirectional HT and TW models and randomly oriented HT and TW models, respectively. The lower bound for α is between 1.00 and 1.46, while the upper bound is between 1.50 and 2.08. The lower bound corresponds with an agglomerate size of between 1.0 – 1.5 μm and the upper bound corresponds with an agglomerate size between 720 nm and 1 μm. Considering that the assumption of homogeneous distribution and perfect contact at the interface hold true, the optimized fit of the models indicates there are significant agglomerations present in the composite system which are altering the effective GNP size. However, along with α, E_1 is influenced by GNP agglomeration size. The effective modulus (E^*) of the GNP will decrease as the agglomeration size increases due to slipping of the GNP with respect to each other and the presence of voids among

them. This will also affect the t^* of the system and the models can be updated to reflect the new assumptions.

5.1.3 Effect of Nanofiller Agglomeration and Effective Modulus

As α increases due to GNP agglomeration, the effective elastic modulus (E^*) of the GNP will change. The GNP aggregate can be modeled as a composite system consisting of GNP and voids. A schematic of a small GNP agglomerate is shown in Figure 5.4 where a minimal agglomeration size of approximately three graphite platelets was assumed and the spacing between platelets was assumed to be ~5 nm. Therefore, t^* was ~40 nm and assuming no reduction in diameter of GNP, the aspect ratio was ~37.5. The rule of mixtures, equation (5.7), was then used to approximate the effective elastic modulus (E^*) of the GNP agglomerate. In this case, E_0 is assumed to be zero to represent the voids between graphite platelets. Therefore, the E^* was approximately 52.3 GPa for the small agglomerate case. The micromechanical models were updated to reflect the new parameters, seen in Table 5.3. However, the models still over predict the modulus, therefore each of the models was optimized to fit the experimental data and the predictions are shown in Table 5.3.

Figure 5.4 Schematic of GNP agglomerate with assumed GNP spacing of 5 nm

Table 5.3 Effect of aspect ratio and effective modulus on elastic modulus

wt%	Exp. Data (GPa)	HT R	HT U	TW R	TW U	HT R	HT U	TW R	TW U
		t=40 nm, E*=52.3 GPa, α=37.5*				*α=1.17*	*α=2.29*	*α=1.15*	*α=1.50*
0	3.179 ±0.054	3.179	3.179	3.179	3.179	3.179	3.179	3.179	3.179
1	3.231 ±0.065	3.289	3.383	3.302	3.478	3.224	3.224	3.241	3.235
5	3.463 ±0.045	3.742	4.223	3.812	4.698	3.412	3.413	3.475	3.470
8	3.459 ±0.248	4.100	4.880	4.215	5.639	3.562	3.564	3.637	3.655
10	3.910 ±0.013	4.347	5.332	4.495	6.279	3.668	3.669	3.738	3.784
12	3.767 ±0.300	4.602	5.795	4.785	6.930	3.777	3.779	3.832	3.917
15	3.854 ±0.033	4.998	6.513	5.237	7.926	3.950	3.952	3.960	4.126

**Note that all units are in GPa*

The lower and upper bounds for α were determined by fitting the experimental data to the randomly oriented HT and TW models and unidirectional HT and TW models, respectively. When considering the change in effective modulus with agglomeration size, the lower bound for α is between 1.15 and 1.17 with an effective modulus of ~46.6 GPa and the upper bound for α is between 1.50 and 2.29 with an effective modulus of ~46.7 GPa. The lower bound corresponds to an agglomerate size of approximately 1.3 μm and the upper bound corresponds to an agglomerate size between 655 nm and 1 μm.

Despite changing the effective modulus of the reinforcement, the predicted upper and lower bounds of α are comparable to that of the case where the modulus of the GNP was held constant at 70 GPa. For the HT models, as α decreases, the influence of the GNP modulus has less impact on E_{11}. This can be seen mathematically in equations (5.3)

and (5.4). For the TW models, altering the modulus of the GNP only affects the Lamé constants, λ_1, μ_1, and κ_1. However, α heavily influences Eshelby's tensor which has a strong effect on E_{11}. Eshelby's tensor as well as the other components of the TW models are further described in Appendix A.

While, studying the effect of α and E^* through a parametric study can help describe the behavior of the composite, it is important to keep in mind the assumptions used to describe the system. For example, the parametric study only took the GNP dispersion / agglomerate size into consideration. Neither the models nor the parametric study took any heterogeneity in the GNP distribution into consideration. In order to better understand the factors that influence the GNP/PLA composite film modulus, design of experiments was used.

5.2 Process-Structure-Property Relationship through Design of Experiments

One of the primary aims of this work is to understand the relationship between nanofiller geometry, nanofiller content, and processing conditions. Using design of experiments, specifically a factorial design regression analysis technique, experiments can be performed more efficiently and multiple variables can be compared simultaneously reducing the number of necessary experiments and saving time. Factorial design can also isolate the effect of each parameter/factor and help with the interpretation of results, particularly when there are interaction or synergistic effects. Through the use of factorial design the effect of each factor on a given composite property can be determined through a single calculated value [97].

The simplest two-level factorial design structure of 2^k is used, with $k = 3$. The 2 represents the two different levels at which k factors will be evaluated. In this case, there are eight factor-level combinations. First the effect of each factor is considered through analysis of variance (ANOVA) and then predictions for the composite performance is considered for each factor and a regression model is proposed. The effect of each factor on the elastic modulus of the composite films was considered.

5.2.1 Analysis of Variance, ANOVA

The ANOVA for the 2^3 factorial design is presented in Table 5.4. Factors *A*, *B*, and *C* represent the main effects, while *AB*, *BC*, and *AC* are the two-factor interactions, and *ABC* is the three-factor interaction. Using the computed values in Table 5.4, the significance of an effect or factor can be determined. The F_o value was compared to the F^* value, which was obtained using a F-statistics table for a confidence level of 5% and the given degrees of freedom. When $F_o/F^* > 1$, the effect is significant, and when $F_o/F^* < 1$ the effect is statistically insignificant [97].

Table 5.4 Analysis of Variance (ANOVA) for a 2^3 factorial design

Effect (Source of Variance)	Degrees of Freedom (df)	Sum of Squares (SS)	Mean Square (SS/df)	F_o
Factor A	$a-1$	SS_A	MS_A	MS_A/MS_E
Factor B	$b-1$	SS_B	MS_B	MS_B/MS_E
Factor C	$c-1$	SS_C	MS_C	MS_C/MS_E
AxB	$(a-1)(b-1)$	SS_{AB}	MS_{AB}	MS_{AB}/MS_E
AxC	$(a-1)(c-1)$	SS_{AC}	MS_{AC}	MS_{AC}/MS_E
BxC	$(b-1)(c-1)$	SS_{BC}	MS_{BC}	MS_{BC}/MS_E
AxBxC	$(a-1)(b-1)(c-1)$	SS_{ABC}	MS_{ABC}	MS_{ABC}/MS_E
Error	$abc(n-1)$	SS_E	MS_E	
Total	$(abcn-1)$	SS_{Total}		

a, b, and c are the number of levels for *A*, *B*, and *C*, respectively. In the case of a 2^3 factorial design, $a = b = c = 2$. Furthermore, n is the number of observations per factor level combination. In this design, $n = 5$ was used in accordance with the recommended number of observations for each test. The sum of squares equations (SS) for the main effects are calculated as outlined in equations (5.9) – (5.11) [97]:

$$SS_A = \frac{1}{bnc}\sum_{i=1}^{a} y_{i\ldots}^2 - \frac{y_{\ldots\ldots}^2}{abnc} \tag{5.9}$$

$$SS_B = \frac{1}{anc}\sum_{j=1}^{b} y_{j\ldots}^2 - \frac{y_{\ldots\ldots}^2}{abnc} \tag{5.10}$$

$$SS_C = \frac{1}{abn}\sum_{k=1}^{c} y_{k\ldots}^2 - \frac{y_{\ldots\ldots}^2}{abnc} \tag{5.11}$$

where $y_{i\ldots}$, $y_{j\ldots}$, and $y_{k\ldots}$ are the total observations made under the i^{th}, j^{th}, and k^{th} levels of factors *A*, *B*, and *C*, respectively. The sum of squares equations for two-factor interactions are outlined in equations (5.12) – (5.14) [97]:

$$SS_{AB} = \frac{1}{nc}\sum_{i=1}^{a}\sum_{j=1}^{b} y_{ij..}^2 - \frac{y_{\ldots\ldots}^2}{abnc} - SS_A - SS_B \tag{5.12}$$

$$SS_{AC} = \frac{1}{nb}\sum_{i=1}^{a}\sum_{k=1}^{c} y_{i.k.}^2 - \frac{y_{\ldots\ldots}^2}{abnc} - SS_A - SS_C \tag{5.13}$$

$$SS_{BC} = \frac{1}{na}\sum_{j=1}^{b}\sum_{k=1}^{c} y_{.jk.}^2 - \frac{y_{\ldots\ldots}^2}{abnc} - SS_B - SS_C \tag{5.14}$$

The sum of squares equation for three-factor interactions is outlined in equation (5.15) [97]:

$$SS_{ABC} = \frac{1}{n}\sum_{i=1}^{a}\sum_{j=1}^{b}\sum_{k=1}^{c} y_{ijk}^2 - \frac{y_{....}^2}{abnc} - SS_A - SS_B - SS_C - SS_{AB} - SS_{AC} - SS_{BC} \quad (5.15)$$

Finally, the total sum of squares is outlined in equation (5.16) [97]:

$$SS_{Total} = \sum_{i=1}^{a}\sum_{j=1}^{b}\sum_{k=1}^{c}\sum_{l=1}^{n} y_{ijkl}^2 - \frac{y_{....}^2}{abnc} \quad (5.16)$$

5.2.2 Regression Model

For a 2^3 factorial design, the regression model outlined in equation (5.17) can be used to describe the experimental results [97]:

$$Y = \beta_0 + \beta_A x_A + \beta_B x_B + \beta_C x_C + \beta_{AB} x_A x_B + \beta_{AC} x_A x_C + \beta_{BC} x_B x_C + \beta_{ABC} x_A x_B x_C \quad (5.17)$$

where β_0 is the overall mean, the β's are the regression coefficients, and the x's are the coded variables and are calculated for each variable as described in equation (5.18):

$$x_A = \frac{A - (A_{low} + A_{high})/2}{(A_{high} - A_{low})/2} \quad (5.18)$$

x_B and x_C are also described by equation (5.18), but with *B* and *C* substituted for *A*, respectively.

The main and secondary effects (*A, B, C, AB, AC, BC,* and *ABC*) are needed in order to calculate the regression model coefficients (β*'s*). The treatment combinations are denoted with lower case letters, as seen in Table 5.5, and a high level of any factor is represented with the lowercase letter of that factor, while the low levels are indicated by the absence of a corresponding letter. For example, the treatment combination labeled a indicates that factor *A* is at its high level (+) and *B* and *C* are at their low level (-). When

all three factors are at their low level, the treatment combination is denoted ℓ, by convention.

Table 5.5 Treatment combination notation and signs for 2^3 factorial design

Experimental Run	Treatment Combination	Factorial Design Effects						
		A	**B**	**C**	**AB**	**AC**	**BC**	**ABC**
1	ℓ	-	-	-	+	+	+	-
2	a	+	-	-	-	-	+	+
3	b	-	+	-	-	+	-	+
4	c	-	-	+	+	-	-	+
5	ab	+	+	-	+	-	-	-
6	ac	+	-	+	-	+	-	-
7	bc	-	+	+	-	-	+	-
8	abc	+	+	+	+	+	+	+

The effects outlined in Table 5.5 are described below, with the main effect *A* described in equation (5.19):

$$A = \bar{y}_{A^+} - \bar{y}_{A^-} \tag{5.19}$$

Where $\bar{y}_{A^+}$ is the average value of the four runs where *A* is at the high level (+) and $\bar{y}_{A^-}$ is the average value of the four runs where *A* is at the low level (-). Therefore, using Table 5.5, the main effect *A* is described by equation (5.20):

$$A = \frac{1}{4n}\{(a + ab + ac + abc) - (\ell + b + c + bc)\} \tag{5.20}$$

Similarly, the main effects of *B, C, AB, AC, BC*, and *ABC* can be written as shown in equations (5.21) – (5.26):

$$B = \frac{1}{4n}\{(b + ab + bc + abc) - (\ell + a + c + ac)\} \tag{5.21}$$

$$C = \frac{1}{4n}\{(c + ac + bc + abc) - (\ell + a + b + ab)\} \tag{5.22}$$

$$AB = \frac{1}{4n}\{(\ell + c + ab + abc) - (a + b + ac + bc)\} \quad (5.23)$$

$$AC = \frac{1}{4n}\{(\ell + b + ac + abc) - (a + c + ab + bc)\} \quad (5.24)$$

$$BC = \frac{1}{4n}\{(\ell + a + bc + abc) - (b + c + ab + ac)\} \quad (5.25)$$

$$ABC = \frac{1}{4n}\{(a + b + c + abc) - (\ell + ab + ac + bc)\} \quad (5.26)$$

The regression coefficients included in equation (5.17) are described below in equations (5.27) – (5.33):

$$\beta_A = A/2 \quad (5.27)$$

$$\beta_B = B/2 \quad (5.28)$$

$$\beta_C = C/2 \quad (5.29)$$

$$\beta_{AB} = AB/2 \quad (5.30)$$

$$\beta_{AC} = AC/2 \quad (5.31)$$

$$\beta_{BC} = BC/2 \quad (5.32)$$

$$\beta_{ABC} = ABC/2 \quad (5.33)$$

Error or coefficient of determination (R^2) describes the proportion of the total variance that is explained by the model. The closer R^2 is to one, the better the "fit" of the model. R^2 is described by equation (5.34) [97]:

$$R^2 = 1 - \frac{SS_E}{SS_{Total}} \quad (5.34)$$

5.2.3 Factor Selection and Factorial Design Results

Factorial design in used to determine the factor(s) that most significantly affect the elastic modulus of the PLA composite films. The parameters chosen were: 1)

nanofiller type, CNT or GNP, 2) nanofiller content, 1 or 3 wt%, and 3) cooling rate during compression molding, FC or SC. The factors chosen are outlined in Table 5.6. The elastic modulus is the dependent variable in the factorial design and is determined experimentally.

Table 5.6 Factors used in factorial design

Factors	**Levels**	
	Low	**High**
Nanofiller Type	GNP	CNT
Nanofiller Content (wt%)	1	3
Processing Conditions	FC	SC

The ANOVA was performed for the elastic modulus using Table 5.4 and equations (5.9) – (5.16). The results of the ANOVA is shown in Table 5.7 in the last column labeled F_o. The significance level of an effect is determined using the F-statistics method. F_o is compared to the F^* value obtained from the F-statistics table in Appendix B. In order to obtain F^*, a significance level of 5% was used and the degrees of freedom were 1 for the numerator and 32 for the denominator, therefore, $F^* = 4.17$. If the F_o value is greater than the F^* value, then the factor is statistically significant. The F_o/F^* values are displayed in Table 5.8.

Table 5.7 The Analysis of Variance Table for the elastic modulus

Effect/Factor	df	Sum of Squares	Mean Square	F_o
Nanofiller Type (A)	1	0.005018	0.005018	0.4036
Nanofiller Content (B)	1	0.005954	0.005954	0.4789
Processing (C)	1	2.475	2.47506	**199.1**
Nanofiller Type x Nanofiller Content (AB)	1	0.1032	0.103226	**8.302**
Nanofiller Type x Processing (AC)	1	0.0002401	0.0002401	0.01931
Nanofiller Content x Processing (BC)	1	0.06740	0.06740	**5.421**
Nanofiller Type x Nanofiller Content x Processing (ABC)	1	0.01109	0.01109	0.8919
Error	32	0.3979	0.01243	1
Total	39	3.066		

Table 5.8 F_o/F^* values based on ANOVA for the elastic modulus 2^3 factorial design

Effect/Factor	Elastic Modulus
Nanofiller Type (A)	0.09678
Nanofiller Content (B)	0.1148
Processing (C)	**47.74**
Nanofiller Type x Nanofiller Content (AB)	**1.991**
Nanofiller Type x Processing (AC)	0.004631
Nanofiller Content x Processing (BC)	**1.300**
Nanofiller Type x Nanofiller Content x Processing (ABC)	0.2139

As seen in Table 5.8, processing conditions have a significant effect on the elastic modulus. The regression model described in equation (5.17) can be written using equations (5.27) – (5.33) to calculate the regression coefficients. Only the significant effects, underlined in Table 5.8, are taken into consideration. The regression model for the elastic modulus is described by equation (5.35):

$$Y = 2.976 + 0.2488x_C + 0.0508x_Ax_B + 0.4105x_Bx_C \quad (5.35)$$

The error of the proposed regression model was calculated using equation (5.34). The R^2 value was ~0.87. Therefore, the regression analysis model shown in equation (5.35) can describe the experimental data with an uncertainty of ~13%.

The effect of processing conditions on the elastic modulus can be visualized using an interaction plot shown in Figure 5.5. The slope of the four lines represent the change in elastic modulus with respect to the cooling rate. The larger the magnitude of the slope, the more significant the effect is on the elastic modulus. All of the slopes are comparable and have a magnitude greater than zero, indicating that there is a strong correlation between cooling rate during compression molding and elastic modulus. Similarly, the effect of nanofiller type is shown in Figure 5.6. The slope of the lines are all approximately zero, indicating there is no significant correlation between the nanofiller type and elastic modulus as displayed previously in Table 5.8.

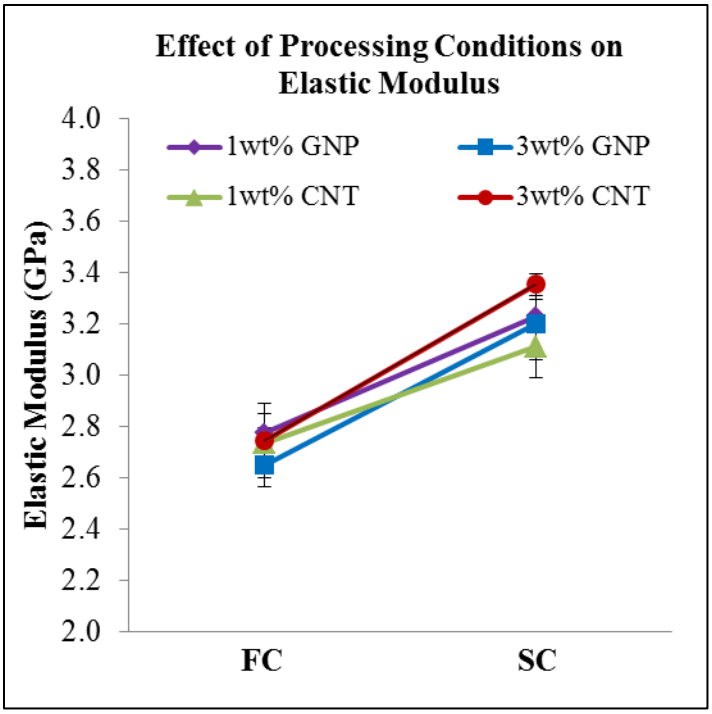

Figure 5.5 Effect of processing conditions on the elastic modulus

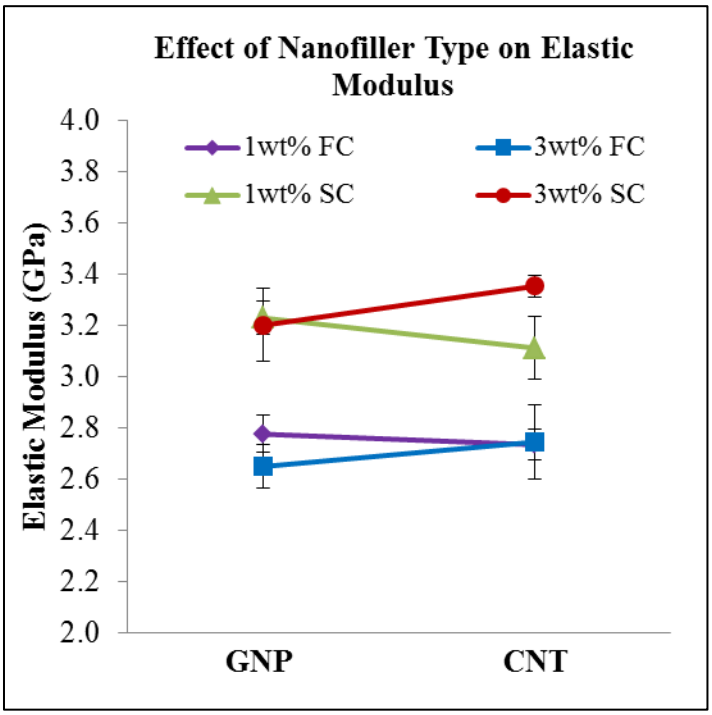

Figure 5.6 Effect of nanofiller type on the elastic modulus

5.3 Conclusions

The influence of parameters such as aspect ratio, processing conditions, and nanofiller type and content on the elastic modulus of the composite films was examined. Upper and lower bounds of the GNP aspect ratio were examined through a parametric study. The aspect ratio of the reinforcing phase will decrease with increased GNP agglomeration size assuming no change in GNP diameter. Furthermore, due to non-perfect contact between GNP in the aggregates and the presence of voids, the effective elastic modulus of the GNP will change with agglomeration size. The models predicted the presence of significant GNP agglomerates. However, the accuracy of the micromechanical modeling is limited by a few critical assumptions. The models assume: 1) perfect contact between the nanofiller and polymer, 2) a specific orientation of the nanofiller throughout the matrix (i.e. unidirectional or randomly aligned), and 3) homogeneous distribution and dispersion or no agglomerations. Design of experiments was used to determine the effect of nanofiller type, content, and processing conditions on the composite films. It was determined that the processing conditions, cooling rate during compression molding, had the most significant effect on the elastic modulus of the films and subsequently a regression model was proposed.

CHAPTER 6

INVESTIGATION OF FULLY BIODEGRADABLE AND BIORENEWABLE POLYLACTIC ACID NANOCOMPOSITE FILMS

The use of carbon based nanofillers, specifically GNP and CNT, has been thoroughly explored. This chapter focuses on investigating fully biodegradable and biorenewable PLA composite films through the use of CNC as the nanofiller. The incorporation of CNC in PLA has previously been explored through melt compounding coupled with the use of solvents, compatibilizers, and chemical modification of the CNC [98-107]. The use of silylated CNC (s-CNC) [99, 102] and plasticizers, such as glycerol triacetate (GTA) [101] and polyethylene glycol (PEG) [100], have been shown to enhance dispersion and minimize agglomerations in PLA composites and alter other composite properties. For example, they result in an increase of elongation at break, but a decrease in both the elastic modulus and tensile strength of PLA as reported [100, 103]. Additionally, the use of toxic solvents and time consuming functionalization steps are not ideal for creating scalable products. An alternative approach to incorporating CNC into PLA is melt compounding combined with liquid feeding [101, 104]. CNC tend to agglomerate when dry due to their high surface area to volume ratio [104]. Therefore, direct liquid feeding of an aqueous CNC suspension is used to help minimize CNC aggregation [104]. When using this type of approach, it is important to consider the miscibility of the aqueous medium and the polymer. For example, in previous research a CNC/polyvinyl alcohol (PVOH) suspension was fed into an extruder with PLA; however,

the immiscibility of PLA and PVOH led to phase separation and CNC was preferentially located in the PVOH phase [105].

This chapter focuses on creating a baseline for CNC/PLA composite film performance for scalable applications. The unique processing aspect of this chapter is that it focuses on fabricating CNC/PLA films via a two-step process: 1) melt compounding using direct liquid feeding, followed by melt fiber spinning and 2) compression molding, as described in Chapter 2. By fiber spinning prior to compression molding, the CNC agglomeration size may be partly controlled and minimized. Fabrication of melt spun CNC/PLA fibers has previously been investigated and the composite fibers displayed enhanced thermal stability due to the hindered polymer chain mobility upon addition of CNC [106]; however, these fibers were not compression molded to make films. This additional step may alter the thermal-mechanical properties. The effect of CNC on PLA fracture surface morphology, crystallization behavior, thermo-mechanical properties, and mechanical performance was investigated.

6.1 Film Microstructure

Representative SEM images of the cryo-fracture surface of the 0 wt% and 3 wt% CNC/PLA films are shown in Figure 6.1. The flatter fracture surface of the composite film as compared to the neat PLA film is indicative of a more brittle fracture event, suggesting that the CNC additions are making the PLA more brittle. This embrittlement is similar to that reported by John et al. [106], in which melt spun fibers having 3 wt% CNC had a lower tensile strength and elongation at break as compared to neat PLA fibers. There are many potential mechanisms for the property change, one that is

considered here is that the CNC additions altered the crystallization behavior of the PLA [108]. CNC has been shown to act as a nucleating agent, promoting crystallization [102], in which changes in the extent of PLA crystallization would alter the fracture properties of the composite. To assess the role of CNC on the PLA crystallization, the crystallization behavior was examined and presented below.

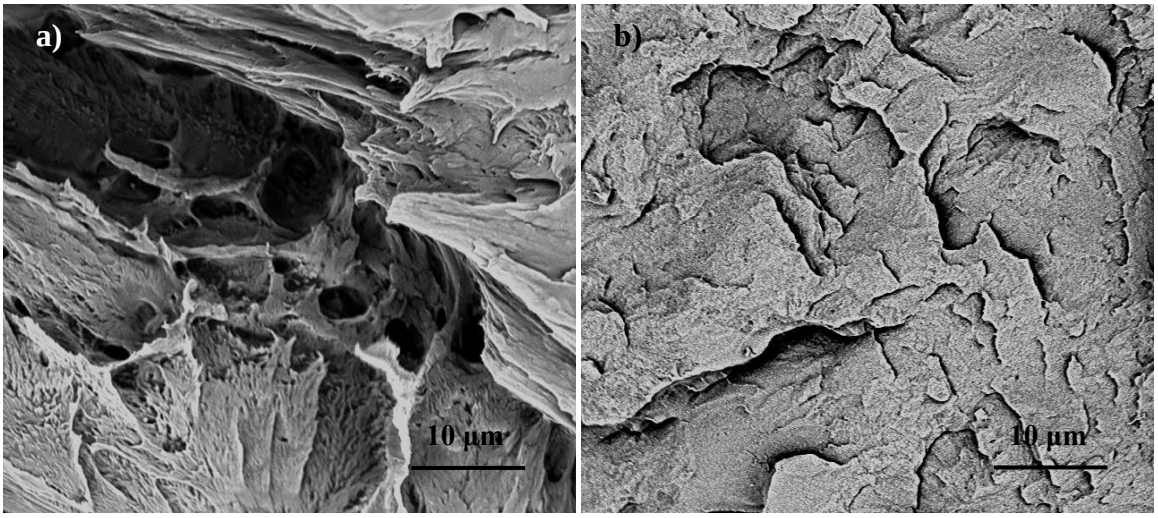

Figure 6.1 Representative SEM images of cryo-fracture surfaces for a) 0 wt% CNC/PLA and b) 3 wt% CNC/PLA composites

6.2 Crystallization Characterization of Composite Films

Crystallization behavior of the CNC/PLA melt spun fibers and films were examined in order to investigate the effect of CNC on PLA crystallization characteristics. Initial heating thermograms, seen in Figure 6.2, were used to calculated the degree of crystallinity (χ) and examine the cold crystallization enthalpy (ΔH_c), and cold crystallization temperature (T_{cc}) as a function of CNC content for both the fibers and

films. Equation (3.1) was used to calculate χ which is displayed along with ΔH_c and T_{cc} in Table 6.1.

Table 6.1 Degree of crystallinity (χ), cold crystallization enthalpy (ΔH_c), and cold crystallization temperature (T_{cc}) for CNC/PLA fibers and films

	χ (%)		$\lvert\Delta H_c\rvert$ (J/g)		T_{cc} (°C)	
	Fibers	**Films**	**Fibers**	**Films**	**Fibers**	**Films**
0wt% CNC	5.7±2.4	11.5±0.8	22.7±2.6	16.2±2.1	113.2±0.5	113.0±0.5
1wt% CNC	2.2±2.1	24.1±0.2	28.0±2.9	7.3±1.3	113.7±0.2	110.2±0.1
2wt% CNC	1.6±1.2	25.3±0.2	28.2±2.8	5.8±0.7	114.5±1.4	109.9±0.2
3wt% CNC	1.3±1.3	29.7±0.5	29.8±0.7	1.9±0.2	113.2±1.3	109.3±0.1

*Note that ΔH_c is reported as an absolute value; however by convention $\Delta H_c < 0$

The fibers are highly amorphous with large $|\Delta H_c|$ because the PLA chains do not have ample time to organize into crystalline lamella due to the rapid cooling of the fibers during melt spinning. However, the films' degree of crystallinity is higher than that of the fibers and also increases with increasing CNC content due to the slow cooling rate during compression molding allowing time for crystallization coupled with CNC acting as a nucleating agent. For example, the 0 wt% CNC film has a relatively low crystallinity at approximately 11.5%, while the 3 wt% CNC film has a relatively high crystallinity at approximately 29.7%. Furthermore, both the $|\Delta H_c|$ and T_{cc} decrease with increased CNC content, seen in Figure 6.2c and d and displayed in Table 6.1. This increase in χ and decrease in both $|\Delta H_c|$ and the cold crystallization peak as a function of CNC content indicates that the CNC are acting as nucleating agents, promoting crystallization in the PLA films [102]. As seen in Figure 6.2e and f, the melting endotherms for both the fibers and films are comparable and do not change with increased CNC content. Both the fibers

and films displayed double melting behavior, which as outlined in Chapter 3 is indicative of either polymorphism or melt recrystallization. To further investigate the crystal structure of the composite fibers and films, diffraction patterns were examined.

The diffraction patterns of the CNC composite fibers and films are seen in Figure 6.3. Both the fibers and films were comprised of primary α phase crystals and do not display evidence of a secondary crystal phase, therefore the double melting behavior seen in Figure 6.2 is due to melt recrystallization and not polymorphism. The diffraction patterns of the fibers, seen in Figure 6.3a, display a broad maximum at $2\theta = 16.7°$ corresponding to the characteristic plane of α(200 + 110) [62] and this is in good agreement with the low crystallinity calculated using equation (3.1) and displayed in Table 6.1. The CNC films display characteristic peaks of crystalline PLA at $2\theta = 16.7°$ and 19.1° which correspond to the α phase crystalline peaks with characteristic planes of (200 + 110) [62] and (203) [64], respectively.

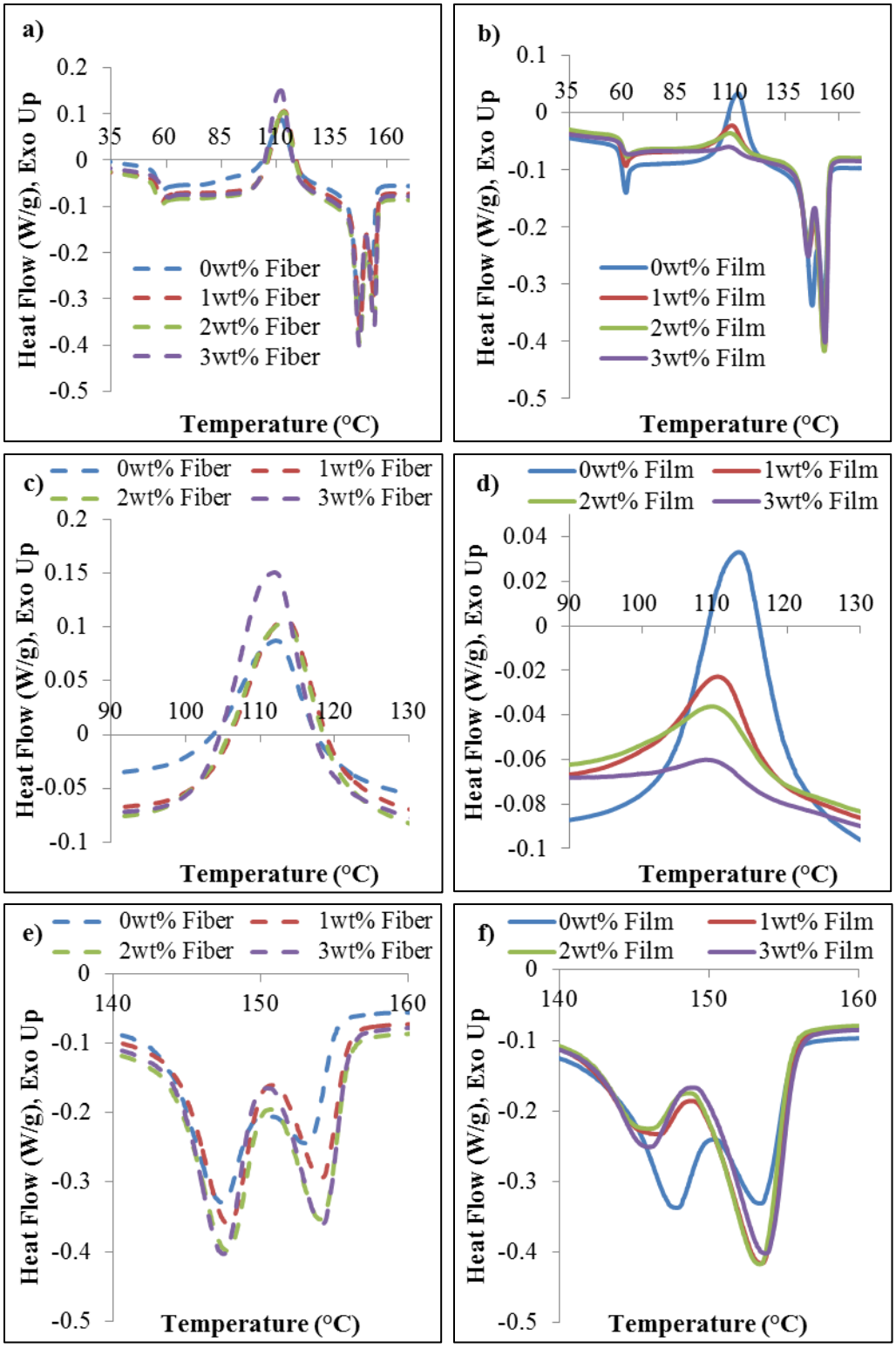

Figure 6.2 Non-isothermal initial heating thermograms of CNC/PLA a) fibers, b) films, c) fiber cold crystallization peaks, d) film cold crystallization peaks, e) fiber melting endotherms, and f) film melting endotherms

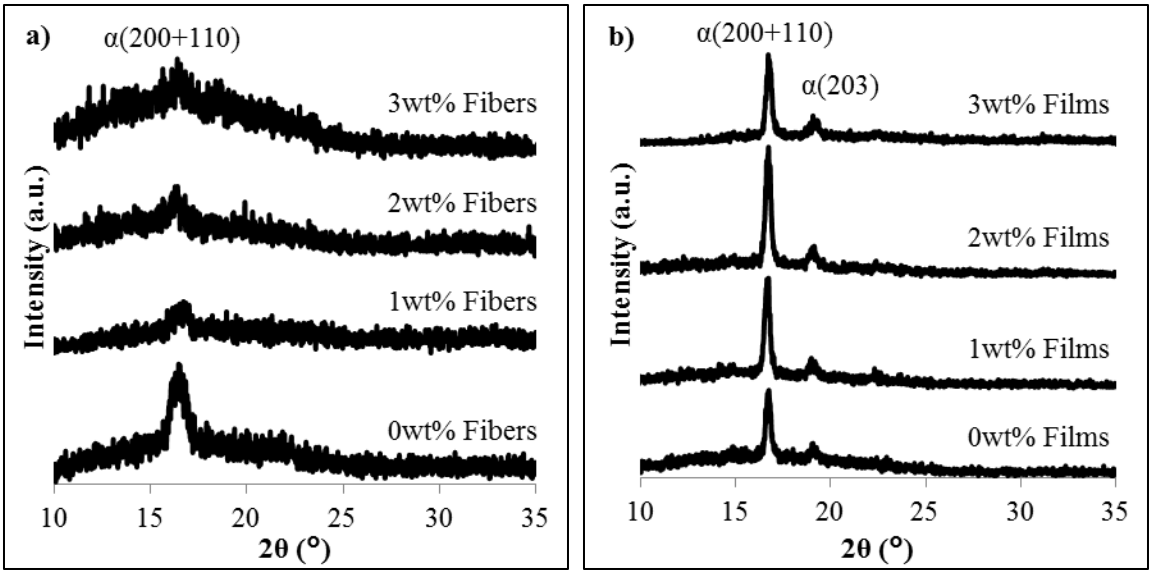

Figure 6.3 Diffraction patterns obtained for the CNC/PLA a) fibers and b) films as a function of CNC content

The diffraction behavior of both the composite fibers and films is dominated by the PLA phase, which is the primary phase of the composite. In order to ascertain the crystal structure of the reinforcing phase, the as-received CNC/water suspension was dried in a vacuum oven and the diffraction pattern of the resultant CNC mat is shown in Figure 6.4. The CNC display primary peaks at 2θ = 15.1°, 17.5°, and 22.7° with a weak diffraction peak at 34.4° which correspond to the cellulose I crystal planes (1-10), (110), (200), and (040), respectively [99, 109, 110]. Diffraction peaks are also seen at 2θ = 12.5° and 20.1° which is consistent with the primary peaks associated with cellulose II which are at 2θ = 12.5°, 20.1°, 22.7°, and 34.4° [110]. The obtained crystal structure of the CNC mat is consistent with previously reported highly crystalline CNC of both cellulose I and II [99, 109]. The existence of cellulose II in the CNC is typical of CNC from Forest Products Laboratory and is likely an artifact of using dissolving pulp as a

source material [111], but may also be attributed to the acid hydrolysis extraction method and exposure to alkali and acid treatments [110].

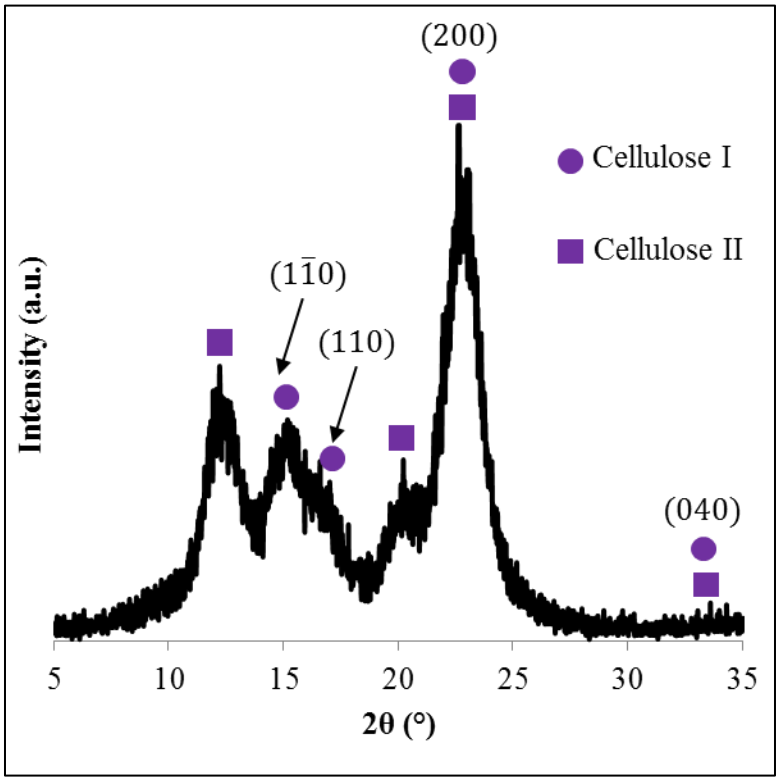

Figure 6.4 Diffraction pattern of a CNC mat with cellulose I and cellulose II primary diffraction peaks indicated

To further investigate the crystal structure of the composite films as a function of CNC content, the average lamella thickness at the PLA primary diffraction peaks, 16.7° and 19.1°, was calculated using equation (3.2). As seen in Figure 6.5, the average lamella thickness does not significantly change for either primary diffraction peak as a function of CNC content. However, the degree of crystallinity significantly increases as a function of CNC content, as reported in Table 6.1, indicating that while the crystallinity of the

films is increasing the average spherulite size is constant. Therefore, as the CNC content increases, there are more spherulites of comparable size present.

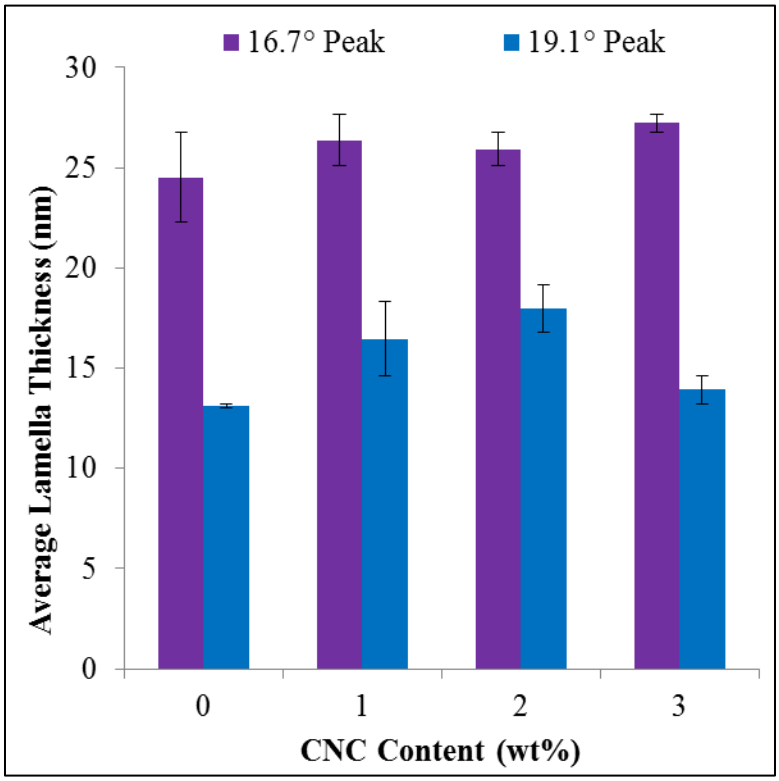

Figure 6.5 Average crystal lamella thickness of the two dominant diffraction peaks, 16.7° and 19.1°, for the CNC/PLA films as a function of CNC content

6.3 Thermo-mechanical and Mechanical Response of Composite Films

The thermo-mechanical behavior of the CNC/PLA films, both the storage modulus (E') and loss modulus (E''), was investigated as a function of CNC content. The results are seen in both Table 6.2 and Figure 6.6. The storage modulus increases significantly from 1.9 ± 0.3 GPa to 2.7 ± 0.0 GPa with the addition of only 1 wt% CNC.

As detailed in Chapter 4, this increase in storage modulus can be attributed to hindered polymer chain mobility due to: 1) an increase in polymer crystallinity [67], 2) the addition of CNC constricting polymer chain movements [82, 83], or 3) a combination of 1) and 2). In this case, the significant increase in storage modulus can be attributed to a combinatory effect because, as shown in Table 6.1, not only is CNC added to the system, but the degree of crystallinity is increasing. Furthermore, as displayed in Table 6.2, there is a slight increase in glass transition temperature (T_g) with the addition of 3 wt% CNC. The T_g values reported in Table 6.2 are from *tanδ* which is defined as *E″/E′*. Additionally, the loss modulus peak shows some indication of broadening upon the addition of CNC, particularly at a higher CNC content of 3 wt%. This can be attributed to both the increase in PLA matrix crystallinity coupled with the addition of CNC, which will further hinder polymer chain mobility resulting in a slight broadening of the glass transition region [107].

Table 6.2 Thermo-mechanical behavior of CNC/PLA films as a function of CNC content

	E′ at 35°C (GPa)	**T_g, from tanδ (°C)**
0 wt% CNC	1.9 ± 0.3	79.3±0.8
1 wt% CNC	2.7 ± 0.0	79.5±0.3
2 wt% CNC	2.7 ± 0.1	78.8±0.0
3 wt% CNC	2.9 ± 0.1	82.2±0.3

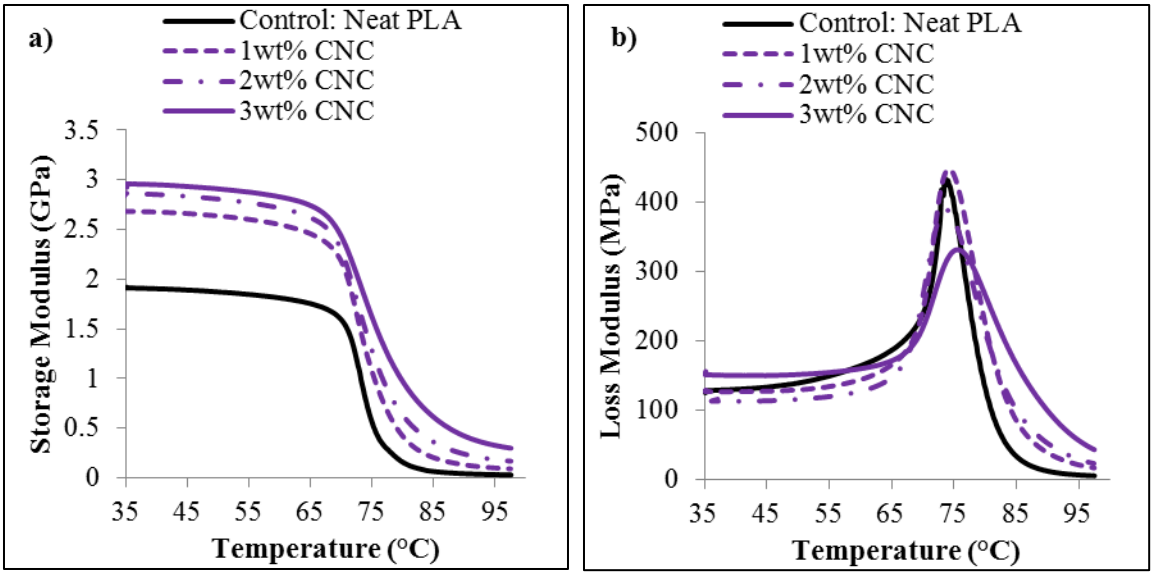

Figure 6.6 a) Storage modulus and b) loss modulus of the CNC/PLA films as a function of CNC content

The elastic modulus, *E*, of the composite films as a function of CNC content is shown in Figure 6.7. As seen in Figure 6.7, there is a minimal change in elastic modulus as a function of CNC content for the CNC/PLA films. This is similar to that reported by John et al. [106], in which melt spun fibers having 3 wt% CNC additions had a modest 0.2 GPa increase in elastic modulus as compared to the neat PLA fibers. The previously reported elastic modulus of CNC (in the axial direction is ~60-105 GPa [112] and 20-50 GPa [113] in the transverse direction) is higher than that of PLA (~3 GPa), therefore, an increase in elastic modulus upon addition of CNC would be expected. However, while CNC have a higher intrinsic elastic modulus, there are several factors that may influence the modulus of the composites including: 1) the CNC/polymer interfacial interactions, 2) CNC distribution and dispersion, 3) CNC alignment, and even 4) moisture content in the composite [20]. Poor interfacial adhesion may also lead to poor nanofiller distribution

and dispersion, which has previously been reported for CN/PLA composites fabricated via melt compounding [114]. Furthermore, because the CNC/PLA films were fabricated using direct liquid feeding of the as-received CNC/water suspension, TGA was performed on the films to investigate whether any moisture was present and representative results of the 3 wt% CNC/PLA films are seen in Figure 6.8. There is no significant moisture content present, therefore excess moisture is not a dominating factor to the plateau in elastic modulus with the addition of CNC content. Furthermore, due to the introduction of water during processing, the degradation of the 3 wt% CNC film was compared to the as-received PLA pellets. As seen in Figure 6.8a and b, the thermal stability of the 3 wt% CNC film is comparable to the as-received PLA pellets and does not appear to be compromised.

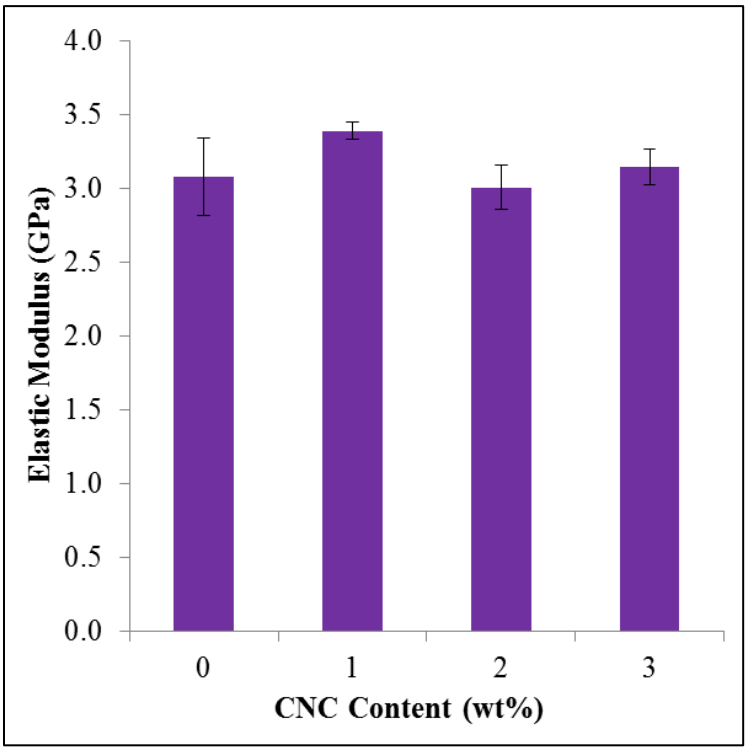

Figure 6.7 Elastic modulus of the CNC/PLA films as a function of CNC content

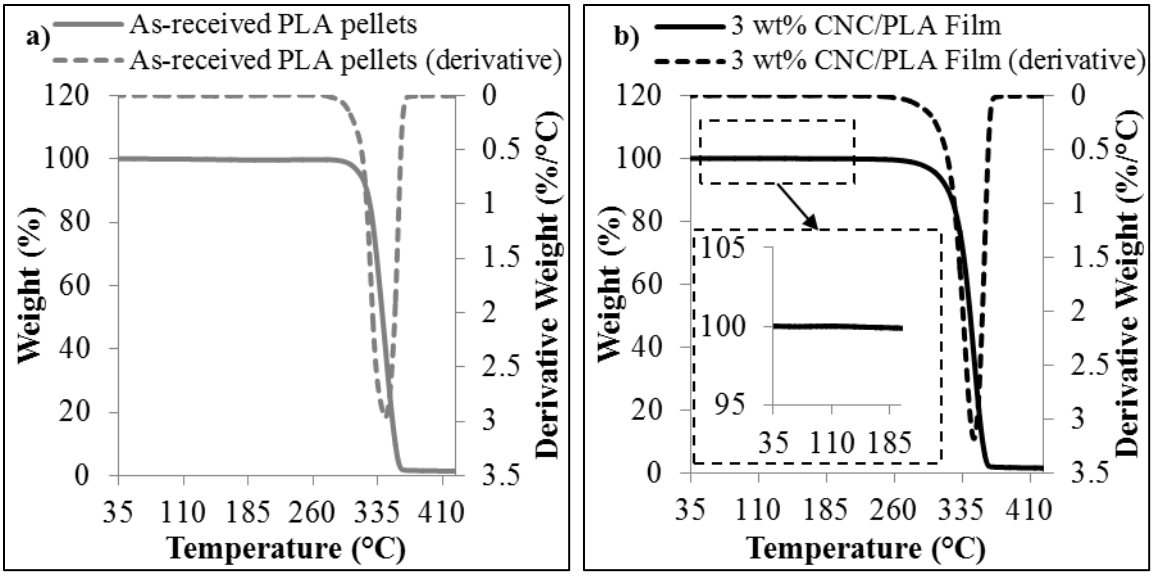

Figure 6.8 Representative TGA of the a) as-received PLA pellets and b) 3 wt% CNC/PLA film

6.4 Conclusions

Cryo-fracture surface SEM images indicated a more brittle fracture surface morphology upon addition of CNC when compared to neat PLA. This can be attributed to the increase in polymer matrix crystallinity with the addition of CNC, indicating CNC is acting as nucleating agents, promoting crystallization. While the CNC did not significantly alter the PLA crystal structure or spherulite lamella thickness, the CNC used was highly crystalline and composed of both cellulose I and II types due to the use of dissolving pulp as a source material and the acid hydrolysis extraction method. The storage modulus of the films did increase with the addition of CNC due to the increased polymer matrix crystallinity coupled with the hindered polymer chain mobility caused by the addition of nanofiller. There was not a significant change in elastic modulus with the

addition of CNC which can be attributed to the: 1) CNC/polymer interfacial interactions, 2) CNC distribution and dispersion, and/or 3) CNC alignment.

The incorporation of CNC in PLA via MC-CM to fabricate fully biodegradable and biorenewable films using a scalable production method was explored in this chapter. While the use of unmodified CNC did show promise to increase the crystallinity of PLA, the elastic modulus was not significantly altered.

CHAPTER 7

CONCLUSIONS AND RECOMMENDATIONS FOR FUTURE WORK

7.1 Conclusions

This study has explored process-structure-property relationships in biodegradable polymer nanocomposite films. It has been shown that the fabrication method, both in terms of processing conditions and compounding method, as well as nanofiller type and content play a significant role in altering the composite film properties.

The cooling rate during compression molding significantly altered the crystallinity of the PLA matrix in the MC-CM films. Furthermore, there was a significant difference in percolation threshold between the FC and SC GNP/PLA films. The FC films percolate between 12-15 wt% of GNP while the SC films percolate between 3-5 wt% of GNP. The difference in percolation is attributed to the difference in crystallization behavior of the insulating polymer phase. The FC films are highly amorphous with a more homogeneous GNP distribution whereas the SC films are highly crystalline and have a more heterogeneous GNP distribution with smaller interparticle distances due to displacement of GNP during spherulite growth. The primary mechanisms for the lower percolation in the SC films are the decreased scattering of electrons through the ordered crystalline lamella in SC films coupled with the excluded volume effect present in SC films. Furthermore, factorial design was used to examine the influence of nanofiller type (CNT versus GNP), nanofiller content, and processing

conditions (FC versus SC) on the elastic modulus of the composite films. It is concluded through design of experiments that cooling rate during compression molding is the primary factor influencing the elastic modulus of both the CNT and GNP MC-CM films.

The compounding method also has an influence on the composite film properties. However, compounding method has a less significant effect on the properties. GNP SoC films exhibited similar crystallization behavior to the GNP SC films. However, the SoC films had a more homogeneous GNP distribution and dispersion due to the low viscosity of the polymer solution during processing which led to a percolation threshold between 5-8 wt% of GNP compared to that of 3-5 wt% for the SC films. The lower percolation of the SC films is attributed to the difference in microstructure both in terms of micro-porosity and dispersion/distribution of GNP coupled with the exclude volume effect. The effect of compounding on film properties was also explored by comparing CNT MC-CM films with CNT E-CM films. By comparing the use of electrospun fibers and melt spun fibers on compression molded films, the influence of compounding can be further isolated by eliminating some of the differences in fabrication, such as lack of compaction of SoC films compared to compression molded films. Both the CNT MC-CM and CNT E-CM films percolated at CNT content less than 1 wt%. However, the 1 wt% E-CM film displayed a lower low frequency $|Z^*|$ compared to the 1 wt% MC-CM film, indicating a higher conductance. The lower low frequency $|Z^*|$ of the 1 wt% CNT E-CM film is attributed to a more heterogeneous dispersion of CNT throughout the matrix, facilitating an interconnected nanofiller network.

The effect of nanofiller type, content, processing conditions, and compounding method on composite film properties was investigated in order to help eliminate the

commonly used trial and error approach to materials design through the creation of property roadmaps. Focusing or narrowing the design space can help facilitate the creation of nanocomposites with tailored properties for targeted applications. An example of a property roadmap created through this study is shown in Figure 7.1. The inverse of the low frequency $|Z^*|$ is displayed as a function of nanofiller content. It is important to note that this property roadmap is exclusive for the specific materials, manufacturing methods, and processing conditions employed in this study. The roadmap can be used to guide future design by outlining the influence of processing and nanofiller content on a given property.

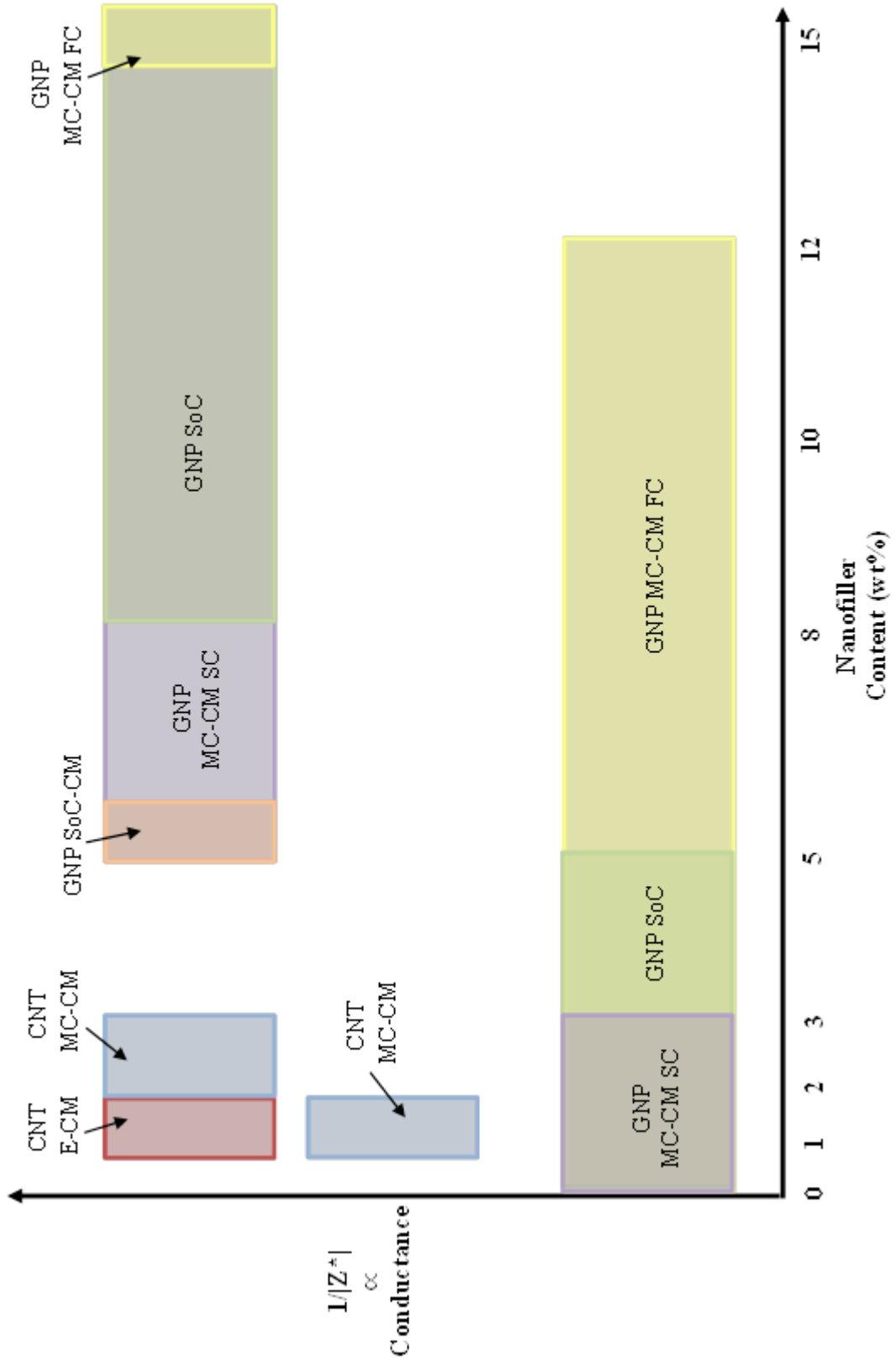

Figure 7.1 Property roadmap example for low frequency impedance magnitude.

7.2 Future Work

Several recommendations for future research can be made based on the results presented in this work. It is suggested, an extensive study on specific processing parameters is performed in order to optimize nanocomposite film properties. Design of experiments can be used to investigate conditions such as screw speed and temperature during melt compounding, as well as solvent type and ultrasonication time for solvent cast films. Processing parameters, such as these, may have an effect on both nanofiller distribution and dispersion, as well as polymer matrix characteristics. Using design of experiments would allow for the selection of optimal processing parameters for enhancing specific properties, such as high elastic modulus or low percolation threshold. Additionally, it is recommended to use enhanced computational modeling to better quantify the effect of aspect ratio and nanofiller agglomeration on the composite properties. Furthermore, it is recommended to perform a detailed analysis of nanofiller orientation through the use of X-ray diffraction. Texture analysis would allow for the quantification of the random in-plane nanofiller orientation within the composite films.

The electrical response of both GNP/PLA and CNT/PLA composite films was examined in this study. A percolation range was given for the composite films fabricated by all processing methods and conditions: less than 1 wt% for the CNT MC-CM and CNT E-CM films, 3-5 wt% for the GNP MC-CM SC films, 5-8 wt% for the GNP SoC films, and 12-15 wt% for the GNP MC-CM FC films. However, in the future it is recommended to expand this study to include an extensive range of nanofiller concentrations in order to pinpoint the percolation threshold for each of the films. This would allow for a more robust property roadmap for future materials design and

applications as it can allow for use of the minimum possible filler content keeping the cost low.

Additionally, exploring the use of functionalization and compatibilizers on CNC/PLA film properties is recommended. This study focused on investigating the potential of unmodified CNC/PLA films using a scalable processing technique. However, the use of modifiers and compatibilizers or plasticizers can help with distribution and dispersion of CNC in PLA. It is suggested to examine the potential trade-offs between using unmodified CNC in PLA and using modified CNC and compatibilizers. Additional processing steps may limit scalability and additives, such as plasticizers may not only compromise the biodegradability and biorenewablity, but also may compromise mechanical performance.

Finally, the design methodology used in this study could be expanded to other polymer nanocomposite materials systems. It would be of particular interest to explore hybrid composites. Utilizing a nucleating agent, such as CNC, combined with an electrically conductive nanofiller, such as CNT, in PLA may help enhance PLA's crystallinity and electrical conductivity. Using knowledge of process-structure-property relationships can help optimize materials manufacturing and eliminate trial and error in materials design.

APPENDIX A

COMPONENTS OF MICROMECHANICAL MODELING EQUATIONS

A.1 Components of Eshelby's Tensor

The components of Eshelby's tensor, S_{ijkl}, assuming a spheroidal inclusion are as follows:

$$S_{1111} = \frac{1}{2(1-\nu_0)}\left\{1 - 2\nu_0 + \frac{3\alpha^2 - 1}{\alpha^2 - 1} - \left[1 - 2\nu_0 + \frac{3\alpha^2}{\alpha^2 - 1}\right] g\right\} \tag{A.1}$$

$$S_{2222} = S_{3333} = \frac{3}{8(1-\nu_0)}\frac{\alpha^2}{\alpha^2 - 1} + \frac{1}{4(1-\nu_0)}\left[1 - 2\nu_0 - \frac{9}{4(\alpha^2 - 1)}\right] g \tag{A.2}$$

$$S_{2233} = S_{3322} = \frac{1}{4(1-\nu_0)}\left\{\frac{\alpha^2}{2(\alpha^2 - 1)} - \left[1 - 2\nu_0 + \frac{3}{4(\alpha^2 - 1)}\right] g\right\} \tag{A.3}$$

$$S_{2211} = S_{3311} = -\frac{1}{2(1-\nu_0)}\frac{\alpha^2}{\alpha^2 - 1} + \frac{1}{4(1-\nu_0)}\left\{\frac{3\alpha^2}{\alpha^2 - 1} - (1 - 2\nu_0)\right\} g \tag{A.4}$$

$$S_{1122} = S_{1133} - \frac{1}{2(1-\nu_0)}\left[1 - 2\nu_0 + \frac{1}{\alpha^2 - 1}\right] + \frac{1}{2(1-\nu_0)}\left[1 - 2\nu_0 + \frac{3}{2(\alpha^2 - 1)}\right] g \tag{A.5}$$

$$S_{2323} = S_{3232} = \frac{1}{4(1-\nu_0)}\left\{\frac{\alpha^2}{2(\alpha^2 - 1)} + \left[1 - 2\nu_0 - \frac{3}{4(\alpha^2 - 1)}\right] g\right\} \tag{A.6}$$

$$S_{1212} = S_{1313} = \frac{1}{4(1-\nu_0)}\left\{1 - 2\nu_0 - \frac{\alpha^2 + 1}{\alpha^2 - 1} - \frac{1}{2}\left[1 - 2\nu_0 - \frac{3}{4(\alpha^2 - 1)}\right] g\right\} \tag{A.7}$$

where ν_0 is the Poisson's ratio of the matrix material, α is the aspect ratio of the inclusion, and g is described below for an prolate inclusion:

$$g = \frac{\alpha}{(\alpha^2 - 1)^{3/2}}\left\{\alpha(1 - \alpha^2)^{1/2} - \cos^{-1}\alpha\right\} \tag{A.8}$$

When the inclusions are spherical ($\alpha = 1$), Eshelby's tensor simplifies to:

$$S_{1111} = S_{2222} = S_{3333} = \frac{7 - \nu_0}{15(1 - \nu_0)} \tag{A.9}$$

$$S_{1122} = S_{2233} = S_{3311} = \frac{5\nu_0 - 1}{15(1 - \nu_0)} \tag{A.10}$$

$$S_{1212} = S_{2323} = S_{3131} = \frac{4 - 5\nu_0}{15(1 - \nu_0)} \tag{A.11}$$

A.2 Components of Tandon-Weng Models

A.2.1 Unidirectional Aligned Tandon-Weng Model Components

The components A_1, A_2, and A are as follows:

$$A_1 = D_1(B_4 + B_5) - 2B_2 \tag{A.12}$$

$$A_2 = (1 + D_1)B_2 - (B_4 + B_5) \tag{A.13}$$

$$A = 2B_2B_3 - B_1(B_4 + B_5) \tag{A.14}$$

where the components B_1, B_2, B_3, B_4, and B_5 are as follows:

$$B_1 = cD_1 + D_2 + (1 - c)(D_1S_{1111} + 2S_{2211}) \tag{A.15}$$

$$B_2 = c + D_3 + (1 - c)(D_1S_{1122} + S_{2222} + S_{2233}) \tag{A.16}$$

$$B_3 = c + D_3 + (1 - c)(S_{1111} + (1 + D_1)S_{2211}) \tag{A.17}$$

$$B_4 = cD_1 + D_2 + (1 - c)(S_{1122} + D_1S_{2222} + S_{2233}) \tag{A.18}$$

$$B_5 = c + D_3 + (1 - c)(S_{1122} + S_{2222} + D_1S_{2233}) \tag{A.19}$$

where c is the volume percent of inclusions in the matrix, S_{ijkl} are the components of Eshelby's tensor described in section (A.1), and the components D_1, D_2, and D_3 are as follows:

$$D_1 = 1 + 2(\mu_1 - \mu_0)/(\lambda_1 - \lambda_0) \tag{A.20}$$

$$D_2 = (\lambda_0 - 2\mu_0)/(\lambda_1 - \lambda_0) \tag{A.21}$$

$$D_3 = \lambda_0/(\lambda_1 - \lambda_0) \tag{A.22}$$

where μ_0 and λ_0 are Lamé constants of the matrix material and μ_1 and λ_1 are Lamé constants of the inclusion. The Lamé constants are described below:

$$\mu_0 = \frac{E_0}{2(1+\nu_0)} \tag{A.23}$$

$$\lambda_0 = \frac{\nu_0 E_0}{(1+\nu_0)(1-2\nu_0)} \tag{A.24}$$

$$\mu_1 = \frac{E_1}{2(1+\nu_1)} \tag{A.25}$$

$$\lambda_1 = \frac{\nu_1 E_1}{(1+\nu_1)(1-2\nu_1)} \tag{A.26}$$

where E_0 and E_1 are the moduli of the matrix and inclusion materials, respectively, and ν_0 ν_1 are the Poisson's ratios of the matrix and inclusion materials, respectively.

A.2.2 Randomly Oriented Tandon-Weng Model Components

p_{11} is described by the following equation:

$$\begin{aligned} p_{11} = \frac{1+\nu_0}{1+c(b_1-b_2)} \times \left\{ \frac{2(a_1+a_2-a_3)+a_4+a_5 a}{16a} - \frac{1}{4[2S_{1212}+\mu_0/(\mu_1-\mu_0)]} \right\} \\ - \frac{(1-\nu_0)(1+cb_5)+2c\nu_0 b_3}{2c^2 b_3 b_4 - (1+cb_5)[1+c(b_1+b_2)]} \frac{2(a_1-a_2+a_3)+a_4+a_5 a}{8a} \\ + \frac{(1-\nu_0)cb_4 + \nu_0[1+c(b_1+b_2)]}{2c^2 b_3 b_4 - (1+cb_5)[1+c(b_1+b_2)]} \end{aligned} \tag{A.27}$$

The components a_1, a_2, a_3, a_4, a_5, and a are as follows:

$$a_1 = 6(\kappa_1-\kappa_0)(\mu_1-\mu_0)(S_{2222}+S_{2233}-1) - 2(\kappa_0\mu_1-\kappa_1\mu_0) + 6\kappa_1(\mu_1-\mu_0) \tag{A.28}$$

$$a_2 = 6(\kappa_1-\kappa_0)(\mu_1-\mu_0)S_{1133} + 2(\kappa_0\mu_1-\kappa_1\mu_0) \tag{A.29}$$

$$a_3 = -6(\kappa_1-\kappa_0)(\mu_1-\mu_0)S_{3311} - 2(\kappa_0\mu_1-\kappa_1\mu_0) \tag{A.30}$$

$$a_4 = 6(\kappa_1 - \kappa_0)(\mu_1 - \mu_0)(S_{1111} - 1) + 2(\kappa_0\mu_1 - \kappa_1\mu_0) + 6\mu_1(\kappa_1 - \kappa_0) \quad \text{(A.31)}$$

$$a_5 = 1/[S_{3322} - S_{3333} + 1 - \mu_1/(\mu_1 - \mu_0)] \quad \text{(A.32)}$$

$$\begin{aligned} a = {} & 6(\kappa_1 - \kappa_0)(\mu_1 - \mu_0)[2S_{1133}S_{3311} - (S_{1111} - 1)(S_{3322} + S_{3333} - 1)] \\ & +2(\kappa_0\mu_1 - \kappa_1\mu_0)[2(S_{1133} + S_{3311}) + (S_{1111} - S_{3322} - S_{3333})] \\ & -6\kappa_1(\mu_1 - \mu_0)(S_{1111} - 1) - 6\mu_1(\kappa_1 - \kappa_0)(S_{2222} + S_{2233} - 1) - 6\kappa_1\mu_1 \end{aligned} \quad \text{(A.33)}$$

where S_{ijkl} is Eshelby's tensor, μ_0 and κ_0 are Lamé constants of the matrix material and μ_1 and κ_1 are Lamé constants of the inclusion. μ_0 and μ_1 are defined in equations (A.23) and (A.25) and κ_0 and κ_1 are listed below:

$$\kappa_0 = \frac{E_0}{3(1 + 2\nu_0)} \quad \text{(A.34)}$$

$$\kappa_1 = \frac{E_1}{3(1 + 2\nu_1)} \quad \text{(A.35)}$$

where E_0 and E_1 are the moduli of the matrix and inclusion materials, respectively, and ν_0 and ν_1 are the Poisson's ratios of the matrix and inclusion, respectively.

The components b_1, b_2, b_3, b_4, and b_5 are as follows:

$$\begin{aligned} b_1 = {} & (1/16a)\{2a_3(6S_{1122} + S_{2222} + S_{2233} - 1) + a_4[3(S_{2222} + S_{2233} - 1) \\ & +2S_{1122}] + 3a_5a(S_{2222} - S_{2233} - 1) + 2a_1[3(S_{1111} - 1) + S_{2211}] \\ & -2a_2(S_{1111} + 3S_{2211} - 1) - 4a\,(2S_{1212} - 1)/[2S_{1212} + \mu_0/(\mu_1 - \mu_0)]\} \end{aligned} \quad \text{(A.36)}$$

$$\begin{aligned} b_2 = {} & (1/16a)\{2a_3[2S_{1122} + 3(S_{2222} + S_{2233} - 1)] + a_4(6S_{1122} + S_{2222} \\ & +S_{2233} - 1) + a_5a(S_{2222} - S_{2233} - 1) + 2a_1(S_{1111} + 3S_{2211} - 1) \\ & -2a_2[S_{2211} + 3(S_{1111} - 1)] + 4a\,(2S_{1212} - 1)/[2S_{1212} + \mu_0/(\mu_1 - \mu_0)] \end{aligned} \quad \text{(A.37)}$$

$$\begin{aligned} b_3 = {} & (1/4a)\{-2a_2(S_{1111} + S_{2211} - 1) + a_4(2S_{1122} + S_{2222} + S_{2233} - 1) \\ & -a_5a(S_{2222} - S_{2233} - 1)\} \end{aligned} \quad \text{(A.38)}$$

$$b_4 = (1/4a)\{2(a_1 - a_2)S_{2211} + (2a_3 + a_4)(S_{2222} + S_{2233} - 1) \quad \text{(A.39)}$$

$$-a_5 a(S_{2222} - S_{2233} - 1)\}$$

$$b_5 = (1/2a)\{-2a_2 S_{2211} + a_4(S_{2222} + S_{2233} - 1) + a_5 a(S_{2222} - S_{2233} - 1)\} \quad \text{(A.40)}$$

where S_{ijkl} is Eshelby's tensor, μ_0 and μ_1 are Lamé constants of the matrix material described in equations (A.23) and (A.25).

APPENDIX B

F-STATISTICS TABLE

TABLE **B.4** Critical Values for the *F* Statistic ($\alpha = .05$)

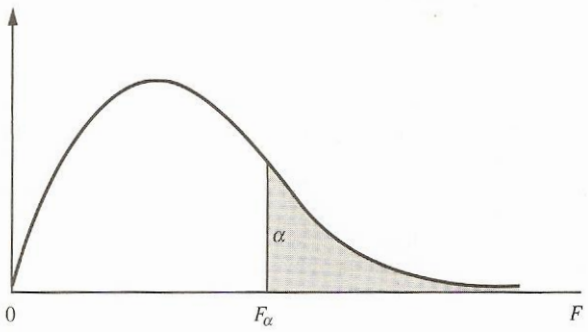

Denominator Degrees of Freedom ($v2$) \ Numerator Degrees of Freedom ($v1$)	1	2	3	4	5	6	7	8	9
1	161.40	199.50	215.70	224.60	230.20	234.00	236.80	238.90	240.50
2	18.51	19.00	19.16	19.25	19.30	19.33	19.35	19.37	19.38
3	10.13	9.55	9.28	9.12	9.01	8.94	8.89	8.85	8.81
4	7.71	6.94	6.59	6.39	6.26	6.16	6.09	6.04	6.00
5	6.61	5.79	5.41	5.19	5.05	4.95	4.88	4.82	4.77
6	5.99	5.14	4.76	4.53	4.39	4.28	4.21	4.15	4.10
7	5.59	4.74	4.35	4.12	3.97	3.87	3.79	3.73	3.68
8	5.32	4.46	4.07	3.84	3.69	3.58	3.50	3.44	3.39
9	5.12	4.26	3.86	3.63	3.48	3.37	3.29	3.23	3.18
10	4.96	4.10	3.71	3.48	3.33	3.22	3.14	3.07	3.02
11	4.84	3.98	3.59	3.36	3.20	3.09	3.01	2.95	2.90
12	4.75	3.89	3.49	3.26	3.11	3.00	2.91	2.85	2.80
13	4.67	3.81	3.41	3.18	3.03	2.92	2.83	2.77	2.71
14	4.60	3.74	3.34	3.11	2.96	2.85	2.76	2.70	2.65
15	4.54	3.68	3.29	3.06	2.90	2.79	2.71	2.64	2.59
16	4.49	3.63	3.24	3.01	2.85	2.74	2.66	2.59	2.54
17	4.45	3.59	3.20	2.96	2.81	2.70	2.61	2.55	2.49
18	4.41	3.55	3.16	2.93	2.77	2.66	2.58	2.51	2.46
19	4.38	3.52	3.13	2.90	2.74	2.63	2.54	2.48	2.42
20	4.35	3.49	3.10	2.87	2.71	2.60	2.51	2.45	2.39
21	4.32	3.47	3.07	2.84	2.68	2.57	2.49	2.42	2.37
22	4.30	3.44	3.05	2.82	2.66	2.55	2.46	2.40	2.34
23	4.28	3.42	3.03	2.80	2.64	2.53	2.44	2.37	2.32
24	4.26	3.40	3.01	2.78	2.62	2.51	2.42	2.36	2.30
25	4.24	3.39	2.99	2.76	2.60	2.49	2.40	2.34	2.28
26	4.23	3.37	2.98	2.74	2.59	2.47	2.39	2.32	2.27
27	4.21	3.35	2.96	2.73	2.57	2.46	2.37	2.31	2.25
28	4.20	3.34	2.95	2.71	2.56	2.45	2.36	2.29	2.24
29	4.18	3.33	2.93	2.70	2.55	2.43	2.35	2.28	2.22
30	4.17	3.32	2.92	2.69	2.53	2.42	2.33	2.27	2.21
40	4.08	3.23	2.84	2.61	2.45	2.34	2.25	2.18	2.12
60	4.00	3.15	2.76	2.53	2.37	2.25	2.17	2.10	2.04
120	3.92	3.07	2.68	2.45	2.29	2.17	2.09	2.02	1.96
∞	3.84	3.00	2.60	2.37	2.21	2.10	2.01	1.94	1.88

TABLE B.4 *(continued)*

Denominator Degrees of Freedom ($v2$) \ Numerator Degrees of Freedom ($v1$)	10	12	15	20	24	30	40	60	120	∞
1	241.90	243.90	245.90	248.00	249.10	250.10	251.10	252.20	253.30	254.30
2	19.40	19.41	19.43	19.45	19.45	19.46	19.47	19.48	19.49	19.50
3	8.79	8.74	8.70	8.66	8.64	8.62	8.59	8.57	8.55	8.53
4	5.96	5.91	5.86	5.80	5.77	5.75	5.72	5.69	5.66	5.63
5	4.74	4.68	4.62	4.56	4.53	4.50	4.46	4.43	4.40	4.36
6	4.06	4.00	3.94	3.87	3.84	3.81	3.77	3.74	3.70	3.67
7	3.64	3.57	3.51	3.44	3.41	3.38	3.34	3.30	3.27	3.23
8	3.35	3.28	3.22	3.15	3.12	3.08	3.04	3.01	2.97	2.93
9	3.14	3.07	3.01	2.94	2.90	2.86	2.83	2.79	2.75	2.71
10	2.98	2.91	2.85	2.77	2.74	2.70	2.66	2.62	2.58	2.54
11	2.85	2.79	2.72	2.65	2.61	2.57	2.53	2.49	2.45	2.40
12	2.75	2.69	2.62	2.54	2.51	2.47	2.43	2.38	2.34	2.30
13	2.67	2.60	2.53	2.46	2.42	2.38	2.34	2.30	2.25	2.21
14	2.60	2.53	2.46	2.39	2.35	2.31	2.27	2.22	2.18	2.13
15	2.54	2.48	2.40	2.33	2.29	2.25	2.20	2.16	2.11	2.07
16	2.49	2.42	2.35	2.28	2.24	2.19	2.15	2.11	2.06	2.01
17	2.45	2.38	2.31	2.23	2.19	2.15	2.10	2.06	2.01	1.96
18	2.41	2.34	2.27	2.19	2.15	2.11	2.06	2.02	1.97	1.92
19	2.38	2.31	2.23	2.16	2.11	2.07	2.03	1.98	1.93	1.88
20	2.35	2.28	2.20	2.12	2.08	2.04	1.99	1.95	1.90	1.84
21	2.32	2.25	2.18	2.10	2.05	2.01	1.96	1.92	1.87	1.81
22	2.30	2.23	2.15	2.07	2.03	1.98	1.94	1.89	1.84	1.78
23	2.27	2.20	2.13	2.05	2.01	1.96	1.91	1.86	1.81	1.76
24	2.25	2.18	2.11	2.03	1.98	1.94	1.89	1.84	1.79	1.73
25	2.24	2.16	2.09	2.01	1.96	1.92	1.87	1.82	1.77	1.71
26	2.22	2.15	2.07	1.99	1.95	1.90	1.85	1.80	1.75	1.69
27	2.20	2.13	2.06	1.97	1.93	1.88	1.84	1.79	1.73	1.67
28	2.19	2.12	2.04	1.96	1.91	1.87	1.82	1.77	1.71	1.65
29	2.18	2.10	2.03	1.94	1.90	1.85	1.81	1.75	1.70	1.64
30	2.16	2.09	2.01	1.93	1.89	1.84	1.79	1.74	1.68	1.62
40	2.08	2.00	1.92	1.84	1.79	1.74	1.69	1.64	1.58	1.51
60	1.99	1.92	1.84	1.75	1.70	1.65	1.59	1.53	1.47	1.39
120	1.91	1.83	1.75	1.66	1.61	1.55	1.50	1.43	1.35	1.25
∞	1.83	1.75	1.67	1.57	1.52	1.46	1.39	1.32	1.22	1.00

REFERENCES

[1] ASSOCIATION, S. T. P. I. T. (June 18). Available: http://www.plasticsindustry.org/aboutplastics/?navItemNumber=1008

[2] NORTH, E. J. and HALDEN, R. U., "Plastics and environmental health: The road ahead," Reviews on environmental health, vol. 28, pp. 1-8, 2013.

[3] HALDEN, R. U., "Plastics and health risks," Annual Review of Public Health, vol. 31, pp. 179-194, 2010.

[4] (2014, September 12). *Plastic waste causes $13 billion in annual damage to marine ecosystems, says un agency*. Available: http://www.un.org/apps/news/story.asp?NewsID=48113#.VBMHLmOa-VU

[5] RAY, S. S. and BOUSMINA, M., "Biodegradable polymers and their layered silicate nano composites: In greening the 21st century materials world," Prog. Mater. Sci., vol. 50, pp. 962-1079, 2005.

[6] JAMSHIDIAN, M., TEHRANY, E. A., IMRAN, M., JACQUOT, M., and DESOBRY, S., "Poly-lactic acid: Production, applications, nanocomposites, and release studies," Compr. Rev. Food. Sci. Food Saf., vol. 9, pp. 552-571, 2010.

[7] LUNT, J., "Large-scale production, properties and commercial applications of polylactic acid polymers," Polymer Degradation and Stability, vol. 59, pp. 145-152, 1998.

[8] VINK, E. T. H., RÁBAGO, K. R., GLASSNER, D. A., and GRUBER, P. R., "Applications of life cycle assessment to natureworks™ polylactide (pla) production," Polymer Degradation and Stability, vol. 80, pp. 403-419, 2003.

[9] DRUMRIGHT, R. E., GRUBER, P. R., and HENTON, D. E., "Polylactic acid technology," Adv. Mater., vol. 12, pp. 1841-1846, 2000.

[10] NAMPOOTHIRI, K. M., NAIR, N. R., and JOHN, R. P., "An overview of the recent developments in polylactide (pla) research," Bioresour. Technol., vol. 101, pp. 8493-8501, 2010.

[11] (May 18). *Matweb: Material property data*. Available: www.matweb.com

[12] *Natureworks*. Available: www.natureworksllc.com

[13] MARK, J. E., *Polymer data handbook*: Oxford University Press, 1999.

[14] VILLMOW, T., PÖTSCHKE, P., PEGEL, S., HÄUSSLER, L., and KRETZSCHMAR, B., "Influence of twin-screw extrusion conditions on the

dispersion of multi-walled carbon nanotubes in a poly(lactic acid) matrix," Polymer, vol. 49, pp. 3500-3509, 2008.

[15] CAPOZZI, C. J. and GERHARDT, R. A., "Novel percolation mechanism in pmma matrix composites containing segregated ito nanowire networks," Adv. Funct. Mater., vol. 17, pp. 2515-2521, 2007.

[16] JOHNSEN, B. B., KINLOCH, A. J., MOHAMMED, R. D., TAYLOR, A. C., and SPRENGER, S., "Toughening mechanisms of nanoparticle-modified epoxy polymers," Polymer, vol. 48, pp. 530-541, 2007.

[17] PARK, J. H. and JANA, S. C., "The relationship between nano- and micro-structures and mechanical properties in pmma–epoxy–nanoclay composites," Polymer, vol. 44, pp. 2091-2100, 2003.

[18] THOSTENSON, E. T., REN, Z. F., and CHOU, T. W., "Advances in the science and technology of carbon nanotubes and their composites: A review," Composites Science and Technology, vol. 61, pp. 1899-1912, 2001.

[19] KALAITZIDOU, K., FUKUSHIMA, H., and DRZAL, L. T., "Multifunctional polypropylene composites produced by incorporation of exfoliated graphite nanoplatelets," Carbon, vol. 45, pp. 1446-1452, 2007.

[20] MOON, R. J., MARTINI, A., NAIRN, J., SIMONSEN, J., and YOUNGBLOOD, J., "Cellulose nanomaterials review: Structure, properties and nanocomposites," Chem. Soc. Rev., vol. 40, pp. 3941-3994, 2011.

[21] WU, H. and DRZAL, L. T., "Graphene nanoplatelet paper as a light-weight composite with excellent electrical and thermal conductivity and good gas barrier properties," Carbon, vol. 50, pp. 1135-1145, 2012.

[22] LI, C., THOSTENSON, E. T., and CHOU, T.-W., "Dominant role of tunneling resistance in the electrical conductivity of carbon nanotube–based composites," Applied Physics Letters, vol. 91, p. 223114, 2007.

[23] HAN, Z. and FINA, A., "Thermal conductivity of carbon nanotubes and their polymer nanocomposites: A review," Progress in Polymer Science, vol. 36, pp. 914-944, 2011.

[24] HANSEN, F., BRUN, V., KELLER, E., WEGNER, T., MEADOR, M., and FRIEDERSDORF, L., "Cellulose nanomaterials - a path towards commercialization workshop report," 2014.

[25] MOON, R. J., BECK, S., RUDIE, A.W., "Cellulose nanocrystals - a material with unique properties and many potential applications," in *Production and applications of cellulose nanomaterials*, M. T. Postek, Moon, R.J, Rudie, A.W.,

Bilodeau, M.A. , Ed., ed Peachtree Corners, Georgia, U.S.A. : Tappi Press, 2013, pp. 9-12.

[26] MIAO, C. W. and HAMAD, W. Y., "Cellulose reinforced polymer composites and nanocomposites: A critical review," Cellulose, vol. 20, pp. 2221-2262, 2013.

[27] TASIS, D., *Carbon nanotube-polymer composites*: Royal Society of Chemistry, 2013.

[28] LIM, L. T., AURAS, R., and RUBINO, M., "Processing technologies for poly(lactic acid)," Progress in Polymer Science, vol. 33, pp. 820-852, 2008.

[29] BADAIRE, S., POULIN, P., MAUGEY, M., and ZAKRI, C., "In situ measurements of nanotube dimensions in suspensions by depolarized dynamic light scattering," Langmuir, vol. 20, pp. 10367-10370, 2004.

[30] BYUN, Y., WHITESIDE, S., THOMAS, R., DHARMAN, M., HUGHES, J., and KIM, Y. T., "The effect of solvent mixture on the properties of solvent cast polylactic acid (pla) film," J. Appl. Polym. Sci., vol. 124, pp. 3577-3582, 2012.

[31] TAIT, M., PEGORETTI, A., DORIGATO, A., and KALAITZIDOU, K., "The effect of filler type and content and the manufacturing process on the performance of multifunctional carbon/poly-lactide composites," Carbon, vol. 49, pp. 4280-4290, 2011.

[32] SUN, Y. P., FU, K. F., LIN, Y., and HUANG, W. J., "Functionalized carbon nanotubes: Properties and applications," Accounts Chem. Res., vol. 35, pp. 1096-1104, 2002.

[33] MICKELSON, E. T., HUFFMAN, C. B., RINZLER, A. G., SMALLEY, R. E., HAUGE, R. H., and MARGRAVE, J. L., "Fluorination of single-wall carbon nanotubes," Chem. Phys. Lett., vol. 296, pp. 188-194, 1998.

[34] FOWLKS, A. C. and NARAYAN, R., "The effect of maleated polylactic acid (pla) as an interfacial modifier in pla-talc composites," J. Appl. Polym. Sci., vol. 118, pp. 2810-2820, 2010.

[35] CARLSON, D., NIE, L., NARAYAN, R., and DUBOIS, P., "Maleation of polylactide (pla) by reactive extrusion," J. Appl. Polym. Sci., vol. 72, pp. 477-485, 1999.

[36] FRONE, A. N., BERLIOZ, S., CHAILAN, J. F., PANAITESCU, D. M., and DONESCU, D., "Cellulose fiber-reinforced polylactic acid," Polym. Compos., vol. 32, pp. 976-985, 2011.

[37] ALI, A. M. and AHMAD, S. H., "Effect of processing parameter and filler content on tensile properties of multi-walled carbon nanotubes reinforced polylactic acid nanocomposite," 2012 National Physics Conference (Perfik 2012), vol. 1528, pp. 254-259, 2013.

[38] KASHIWAGI, T., GRULKE, E., HILDING, J., HARRIS, R., AWAD, W., and DOUGLAS, J., "Thermal degradation and flammability properties of poly (propylene)/carbon nanotube composites," Macromolecular Rapid Communications, vol. 23, pp. 761-765, 2002.

[39] KIM, K. H. and JO, W. H., "Synthesis of polythiophene-graft-pmma and its role as compatibilizer for poly(styrene-co-acrylonitrile)/mwcnt nanocomposites," Macromolecules, vol. 40, pp. 3708-3713, 2007.

[40] KALAITZIDOU, K., FUKUSHIMA, H., ASKELAND, P., and DRZAL, L. T., "The nucleating effect of exfoliated graphite nanoplatelets and their influence on the crystal structure and electrical conductivity of polypropylene nanocomposites," J. Mater. Sci., vol. 43, pp. 2895-2907, 2008.

[41] *Xg sciences*. Available: www.xgsciences.com

[42] *Cheaptubes*. Available: www.cheaptubes.com

[43] GIROUARD, N., SCHUENEMAN, G. T., SHOFNER, M. L., and MEREDITH, J. C., "Exploiting colloidal interfaces to increase dispersion, performance, and pot-life in cellulose nanocrystal/waterborne epoxy composites," Polymer, vol. 68, pp. 111-121, 2015.

[44] GERHARDT, R. A., "Impedance spectroscopy and mobility spectra," in *Encyclopedia of condensed matter physics*, F. Bassani, G. L. Liedl, and P. Wyder, Eds., ed Oxford: Elsevier, 2005, pp. 350-363.

[45] PENG, C. Q., THIO, Y. S., and GERHARDT, R. A., "Conductive paper fabricated by layer-by-layer assembly of polyelectrolytes and ito nanoparticles," Nanotechnology, vol. 19, 2008.

[46] KIM, I. H. and JEONG, Y. G., "Polylactide/exfoliated graphite nanocomposites with enhanced thermal stability, mechanical modulus, and electrical conductivity," J. Polym. Sci. Pt. B-Polym. Phys., vol. 48, pp. 850-858, 2010.

[47] DUAN, J. K., SHAO, S. X., YA, L., WANG, L. F., JIANG, P. K., and LIU, B. P., "Polylactide/graphite nanosheets/mwcnts nanocomposites with enhanced mechanical, thermal and electrical properties," Iran. Polym. J., vol. 21, pp. 109-120, 2012.

[48] AHARONY, A. and STAUFFER, D., *Introduction to percolation theory*: Taylor & Francis, 2003.

[49] GOKTURK, H. S., FISKE, T. J., and KALYON, D. M., "Effects of particle-shape and size distributions on the electrical and magnetic-properties of nickel/polyethylene composites," J. Appl. Polym. Sci., vol. 50, pp. 1891-1901, 1993.

[50] JING, X., ZHAO, W., and LAN, L., "The effect of particle size on electric conducting percolation threshold in polymer/conducting particle composites," J. Mater. Sci. Lett., vol. 19, pp. 377-379, 2000.

[51] CLINGERMAN, M. L., WEBER, E. H., KING, J. A., and SCHULZ, K. H., "Development of an additive equation for predicting the electrical conductivity of carbon-filled composites," J. Appl. Polym. Sci., vol. 88, pp. 2280-2299, 2003.

[52] SULLIVAN, E., OH, Y., GERHARDT, R., WANG, B., and KALAITZIDOU, K., "Understanding the effect of polymer crystallinity on the electrical conductivity of exfoliated graphite nanoplatelet/polylactic acid composite films," J Polym Res, vol. 21, pp. 1-9, 2014.

[53] CHODAK, I. and KRUPA, I., ""Percolation effect" and mechanical behavior of carbon black filled polyethylene," J. Mater. Sci. Lett., vol. 18, pp. 1457-1459, 1999.

[54] KALAITZIDOU, K., FUKUSHIMA, H., and DRZAL, L. T., "A route for polymer nanocomposites with engineered electrical conductivity and percolation threshold," Materials, vol. 3, pp. 1089-1103, 2010.

[55] RAY, S. S., YAMADA, K., OKAMOTO, M., FUJIMOTO, Y., OGAMI, A., and UEDA, K., "New polylactide/layered silicate nanocomposites. 5. Designing of materials with desired properties," Polymer, vol. 44, pp. 6633-6646, 2003.

[56] RHIM, J. W., MOHANTY, A. K., SINGH, S. P., and NG, P. K. W., "Effect of the processing methods on the performance of polylactide films: Thermocompression versus solvent casting," J. Appl. Polym. Sci., vol. 101, pp. 3736-3742, 2006.

[57] MURARIU, M., DECHIEF, A. L., BONNAUD, L., PAINT, Y., GALLOS, A., FONTAINE, G., BOURBIGOT, S., and DUBOIS, P., "The production and properties of polylactide composites filled with expanded graphite," Polymer Degradation and Stability, vol. 95, pp. 889-900, 2010.

[58] KRIKORIAN, V. and POCHAN, D. J., "Unusual crystallization behavior of organoclay reinforced poly(l-lactic acid) nanocomposites," Macromolecules, vol. 37, pp. 6480-6491, 2004.

[59] YASUNIWA, M., TSUBAKIHARA, S., SUGIMOTO, Y., and NAKAFUKU, C., "Thermal analysis of the double-melting behavior of poly(l-lactic acid)," J. Polym. Sci. Pt. B-Polym. Phys., vol. 42, pp. 25-32, 2004.

[60] CHEN, X. L., KALISH, J., and HSU, S. L., "Structure evolution of alpha '-phase poly(lactic acid)," J. Polym. Sci. Pt. B-Polym. Phys., vol. 49, pp. 1446-1454, 2011.

[61] HEBERT, J. S., WOOD-ADAMS, P., HEUZEY, M. C., DUBOIS, C., and BRISSON, J., "Morphology of polylactic acid crystallized during annealing after uniaxial deformation," J. Polym. Sci. Pt. B-Polym. Phys., vol. 51, pp. 430-440, 2013.

[62] HOOGSTEEN, W., POSTEMA, A. R., PENNINGS, A. J., TENBRINKE, G., and ZUGENMAIER, P., "Crystal-structure, conformation, and morphology of solution-spun poly(l-lactide) fibers," Macromolecules, vol. 23, pp. 634-642, 1990.

[63] GOPAKUMAR, T. G. and PAGE, D., "Polypropylene/graphite nanocomposites by thermo-kinetic mixing," Polymer Engineering and Science, vol. 44, pp. 1162-1169, 2004.

[64] PLUTA, M. and GALESKI, A., "Crystalline and supermolecular structure of polylactide in relation to the crystallization method," J. Appl. Polym. Sci., vol. 86, pp. 1386-1395, 2002.

[65] LANGFORD, J. I. and WILSON, A. J. C., "Scherrer after 60 years - survey and some new results in determination of crystallite size," J. Appl. Crystallogr., vol. 11, pp. 102-113, 1978.

[66] DIEZ-PASCUAL, A. M., GUAN, J. W., SIMARD, B., and GOMEZ-FATOU, M. A., "Poly(phenylene sulphide) and poly(ether ether ketone) composites reinforced with single-walled carbon nanotube buckypaper: Ii - mechanical properties, electrical and thermal conductivity," Compos. Pt. A-Appl. Sci. Manuf., vol. 43, pp. 1007-1015, 2012.

[67] LANDEL, R. F. and NIELSEN, L. E., *Mechanical properties of polymers and composites, second edition*: Taylor & Francis, 1993.

[68] RAMANATHAN, T., STANKOVICH, S., DIKIN, D. A., LIU, H., SHEN, H., NGUYEN, S. T., and BRINSON, L. C., "Graphitic nanofillers in pmma nanocomposites - an investigation of particle size influence on nanocomposite and dispersion and their properties," J. Polym. Sci. Pt. B-Polym. Phys., vol. 45, pp. 2097-2112, 2007.

[69] CHO, D., LEE, S., YANG, G. M., FUKUSHIMA, H., and DRZAL, L. T., "Dynamic mechanical and thermal properties of phenylethynyl-terminated

polyimide composites reinforced with expanded graphite nanoplatelets," Macromol. Mater. Eng., vol. 290, pp. 179-187, 2005.

[70] MACKAY, M. E., DAO, T. T., TUTEJA, A., HO, D. L., VAN HORN, B., KIM, H. C., and HAWKER, C. J., "Nanoscale effects leading to non-einstein-like decrease in viscosity," Nat. Mater., vol. 2, pp. 762-766, 2003.

[71] EZQUERRA, T. A., CONNOR, M. T., ROY, S., KULESCZA, M., FERNANDES-NASCIMENTO, J., and BALTÁ-CALLEJA, F. J., "Alternating-current electrical properties of graphite, carbon-black and carbon-fiber polymeric composites," Composites Science and Technology, vol. 61, pp. 903-909, 2001.

[72] OU, R. Q., GUPTA, S., PARKER, C. A., and GERHARDT, R. A., "Fabrication and electrical conductivity of poly(methyl methacrylate) (pmma)/carbon black (cb) composites: Comparison between an ordered carbon black nanowire-like segregated structure and a randomly dispersed carbon black nanostructure," J. Phys. Chem. B, vol. 110, pp. 22365-22373, 2006.

[73] SANDLER, J. K. W., KIRK, J. E., KINLOCH, I. A., SHAFFER, M. S. P., and WINDLE, A. H., "Ultra-low electrical percolation threshold in carbon-nanotube-epoxy composites," Polymer, vol. 44, pp. 5893-5899, 2003.

[74] LEWIS, T. J., "Charge transport, charge injection and breakdown in polymeric insulators," J. Phys. D-Appl. Phys., vol. 23, pp. 1469-1478, 1990.

[75] MCCULLEN, S. D., STEVENS, D. R., ROBERTS, W. A., CLARKE, L. I., BERNACKI, S. H., GORGA, R. E., and LOBOA, E. G., "Characterization of electrospun nanocomposite scaffolds and biocompatibility with adipose-derived human mesenchymal stem cells," Int. J. Nanomed., vol. 2, pp. 253-263, 2007.

[76] KONG, Y. X., YUAN, J., WANG, Z. M., and QIU, J., "Study on the preparation and properties of aligned carbon nanotubes/polylactide composite fibers," Polym. Compos., vol. 33, pp. 1613-1619, 2012.

[77] YANG, T., WU, D. F., LU, L. L., ZHOU, W. D., and ZHANG, M., "Electrospinning of polylactide and its composites with carbon nanotubes," Polym. Compos., vol. 32, pp. 1280-1288, 2011.

[78] SHAO, S., ZHOU, S., LI, L., LI, J., LUO, C., WANG, J., LI, X., and WENG, J., "Osteoblast function on electrically conductive electrospun pla/mwcnts nanofibers," Biomaterials, vol. 32, pp. 2821-2833, 2011.

[79] YADAV, S. K. and CHO, J. W., "Functionalized graphene nanoplatelets for enhanced mechanical and thermal properties of polyurethane nanocomposites," Appl. Surf. Sci., vol. 266, pp. 360-367, 2013.

[80] ROY, S., DAS, T., MING, Y., CHEN, X. L., YUE, C. Y., and HU, X., "Specific functionalization and polymer grafting on multiwalled carbon nanotubes to fabricate advanced nylon 12 composites," J. Mater. Chem. A, vol. 2, pp. 3961-3970, 2014.

[81] LI, B. and ZHONG, W.-H., "Review on polymer/graphite nanoplatelet nanocomposites," J. Mater. Sci., vol. 46, pp. 5595-5614, 2011.

[82] JIN, Z., PRAMODA, K. P., XU, G., and GOH, S. H., "Dynamic mechanical behavior of melt-processed multi-walled carbon nanotube/poly(methyl methacrylate) composites," Chem. Phys. Lett., vol. 337, pp. 43-47, 2001.

[83] DIEZ-PASCUAL, A. M., GUAN, J. W., SIMARD, B., and GOMEZ-FATOU, M. A., "Poly(phenylene sulphide) and poly(ether ether ketone) composites reinforced with single-walled carbon nanotube buckypaper: I - structure, thermal stability and crystallization behaviour," Compos. Pt. A-Appl. Sci. Manuf., vol. 43, pp. 997-1006, 2012.

[84] GARDEA, F., GLAZ, B., RIDDICK, J., LAGOUDAS, D. C., and NARAGHI, M., "Energy dissipation due to interfacial slip in nanocomposites reinforced with aligned carbon nanotubes," Acs Applied Materials & Interfaces, vol. 7, pp. 9725-9735, 2015.

[85] BAUHOFER, W. and KOVACS, J. Z., "A review and analysis of electrical percolation in carbon nanotube polymer composites," Composites Science and Technology, vol. 69, pp. 1486-1498, 2009.

[86] CONSIGLIO, R., BAKER, D. R., PAUL, G., and STANLEY, H. E., "Continuum percolation thresholds for mixtures of spheres of different sizes," Physica A, vol. 319, pp. 49-55, 2003.

[87] RINTOUL, M. D. and TORQUATO, S., "Precise determination of the critical threshold and exponents in a three-dimensional continuum percolation model," Journal of Physics A: Mathematical and General, vol. 30, p. L585, 1997.

[88] ANDREWS, R., JACQUES, D., MINOT, M., and RANTELL, T., "Fabrication of carbon multiwall nanotube/polymer composites by shear mixing," Macromol. Mater. Eng., vol. 287, pp. 395-403, 2002.

[89] HALPIN, J. C., "Effects of environmental factors on composite materials," DTIC Document1969.

[90] HALPIN, J. C. and KARDOS, J. L., "Halpin-tsai equations - review," Polymer Engineering and Science, vol. 16, pp. 344-352, 1976.

[91] TANDON, G. P. and WENG, G. J., "The effect of aspect ratio of inclusions on the elastic properties of unidirectionally aligned composites," Polym. Compos., vol. 5, pp. 327-333, 1984.

[92] TANDON, G. P. and WENG, G. J., "Average stress in the matrix and effective moduli of randomly oriented composites," Composites Science and Technology, vol. 27, pp. 111-132, 1986.

[93] LEE, C., WEI, X. D., KYSAR, J. W., and HONE, J., "Measurement of the elastic properties and intrinsic strength of monolayer graphene," Science, vol. 321, pp. 385-388, 2008.

[94] YU, M. F., LOURIE, O., DYER, M. J., MOLONI, K., KELLY, T. F., and RUOFF, R. S., "Strength and breaking mechanism of multiwalled carbon nanotubes under tensile load," Science, vol. 287, pp. 637-640, 2000.

[95] KAREVAN, M. and KALAITZIDOU, K., "Formation of a complex constrained region at the graphite nanoplatelets-polyamide 12 interface," Polymer, vol. 54, pp. 3691-3698, 2013.

[96] YASMIN, A. and DANIEL, I. M., "Mechanical and thermal properties of graphite platelet/epoxy composites," Polymer, vol. 45, pp. 8211-8219, 2004.

[97] DIELMAN, T. E., *Applied regression analysis for business and economics*: Duxbury/Thomson Learning, 2001.

[98] ABDULKHANI, A., HOSSEINZADEH, J., ASHORI, A., DADASHI, S., and TAKZARE, Z., "Preparation and characterization of modified cellulose nanofibers reinforced polylactic acid nanocomposite," Polym. Test, vol. 35, pp. 73-79, 2014.

[99] FORTUNATI, E., PELTZER, M., ARMENTANO, I., TORRE, L., JIMENEZ, A., and KENNY, J. M., "Effects of modified cellulose nanocrystals on the barrier and migration properties of pla nano-biocomposites," Carbohydr. Polym., vol. 90, pp. 948-956, 2012.

[100] OKSMAN, K., MATHEW, A. P., BONDESON, D., and KVIEN, I., "Manufacturing process of cellulose whiskers/polylactic acid nanocomposites," Composites Science and Technology, vol. 66, pp. 2776-2784, 2006.

[101] HERRERA, N., MATHEW, A. P., and OKSMAN, K., "Plasticized polylactic acid/cellulose nanocomposites prepared using melt-extrusion and liquid feeding: Mechanical, thermal and optical properties," Composites Science and Technology, vol. 106, pp. 149-155, 2015.

[102] PEI, A. H., ZHOU, Q., and BERGLUND, L. A., "Functionalized cellulose nanocrystals as biobased nucleation agents in poly(l-lactide) (plla) - crystallization and mechanical property effects," Composites Science and Technology, vol. 70, pp. 815-821, 2010.

[103] JACOBSEN, S. and FRITZ, H. G., "Plasticizing polylactide - the effect of different plasticizers on the mechanical properties," Polymer Engineering and Science, vol. 39, pp. 1303-1310, 1999.

[104] JONOOBI, M., HARUN, J., MATHEW, A. P., and OKSMAN, K., "Mechanical properties of cellulose nanofiber (cnf) reinforced polylactic acid (pla) prepared by twin screw extrusion," Composites Science and Technology, vol. 70, pp. 1742-1747, 2010.

[105] BONDESON, D. and OKSMAN, K., "Polylactic acid/cellulose whisker nanocomposites modified by polyvinyl alcohol," Compos. Pt. A-Appl. Sci. Manuf., vol. 38, pp. 2486-2492, 2007.

[106] JOHN, M. J., ANANDJIWALA, R., OKSMAN, K., and MATHEW, A. P., "Melt-spun polylactic acid fibers: Effect of cellulose nanowhiskers on processing and properties," J. Appl. Polym. Sci., vol. 127, pp. 274-281, 2013.

[107] KAMAL, M. R. and KHOSHKAVA, V., "Effect of cellulose nanocrystals (cnc) on rheological and mechanical properties and crystallization behavior of pla/cnc nanocomposites," Carbohydr. Polym., vol. 123, pp. 105-114, 2015.

[108] TODO, M., PARK, S.-D., TAKAYAMA, T., and ARAKAWA, K., "Fracture micromechanisms of bioabsorbable plla/pcl polymer blends," Engineering Fracture Mechanics, vol. 74, pp. 1872-1883, 2007.

[109] MAITI, S., JAYARAMUDU, J., DAS, K., REDDY, S. M., SADIKU, R., RAY, S. S., and LIU, D. G., "Preparation and characterization of nano-cellulose with new shape from different precursor," Carbohydr. Polym., vol. 98, pp. 562-567, 2013.

[110] XU, X., LIU, F., JIANG, L., ZHU, J. Y., HAAGENSON, D., and WIESENBORN, D. P., "Cellulose nanocrystals vs. Cellulose nanofibrils: A comparative study on their microstructures and effects as polymer reinforcing agents," Acs Applied Materials & Interfaces, vol. 5, pp. 2999-3009, 2013.

[111] REINER, R. S. and RUDIE, A. W., ".1 process scale-up of cellulose nanocrystal production to 25 kg per batch at the forest products laboratory," 2013.

[112] RUSLI, R. and EICHHORN, S. J., "Determination of the stiffness of cellulose nanowhiskers and the fiber-matrix interface in a nanocomposite using raman spectroscopy," Applied Physics Letters, vol. 93, 2008.

[113] LAHIJI, R. R., XU, X., REIFENBERGER, R., RAMAN, A., RUDIE, A., and MOON, R. J., "Atomic force microscopy characterization of cellulose nanocrystals," Langmuir, vol. 26, pp. 4480-4488, 2010.

[114] MATHEW, A. P., OKSMAN, K., and SAIN, M., "Mechanical properties of biodegradable composites from poly lactic acid (pla) and microcrystalline cellulose (mcc)," J. Appl. Polym. Sci., vol. 97, pp. 2014-2025, 2005.